COUPLED ELECTROMAGNETIC AND THERMAL ANALYSIS AND DESIGN OPTIMIZATION OF SYNCHRONOUS ELECTRIC MACHINES

by
Yi Wang

A Thesis Submitted in

Partial Fulfillment of the

Requirements for the Degree of

Master of Science

in Engineering

at

The University of Wisconsin-Milwaukee

August 2014

ABSTRACT

COUPLED ELECTROMAGNETIC AND THERMAL
ANALYSIS AND DESIGN OPTIMIZATION OF
SYNCHRONOUS ELECTRIC MACHINES

by

Yi Wang

University of Wisconsin-Milwaukee, 2014
Under the Supervision of Dr. Adel Nasiri and Dr. Dan M. Ionel

A new technique for coupling the electromagnetic, thermal, and air-flow analysis is proposed for electronically controlled synchronous machines. A computationally efficient finite element analysis (CE-FEA) technique is employed for the electromagnetic field analysis. An equivalent circuit network is used for thermal and air-flow analysis. An iterative algorithm, which exploits the fact that the type of machines studied have very low rotor losses and also a relatively reduced dependency of core losses with temperature and load, has been developed. The overall computational time is significantly reduced in comparison with the conventional coupling method, such that the new technique is highly suitable for large scale optimization studies. An automated design optimization method based on differential evolution algorithms has also been developed and implemented on a multi-core computer system. Example case studies are provided for permanent magnet and for synchronous reluctance machines. Computational and experimental results from prototype motors are included.

Dedicated to my parents

for their infinite love, support, and encouragement

TABLE OF CONTENTS

LIST OF FIGURES

LIST OF TABLES

ACKNOWLEDGEMENTS

First of all, I would like to express my deepest gratitude to my advisors, Dr. Dan M. Ionel and Dr. Adel Nasiri, for their close guidance, invaluable suggestions, and selfless support during this research. I also wish to thank them for giving me the opportunity to begin and complete my Master studies at University of Wisconsin - Milwaukee, for kind and continuous encouragement, and for teaching me how think like a scientist and innovate like an engineer.

The sponsorship provided by Regal Beloit Corp. (RBC) for my graduate student research is gratefully acknowledged. Special thanks are due to Mr. Steven Stretz, engineering manager with RBC, for continuous support and expert advice from an industrial perspective. I thank also Mr. Alan Yeadon, especially for his contributions to the prototyping and experimentation performed at RBC.

ANSYS Corp. and Motor Design Ltd. (MDL) are gratefully acknowledged for providing simulation software. Special thanks are due to Mr. Mark Solveson and Dr. Marius Rosu of ANSYS, and to Dr. David Staton, Mr. Douglas Hawkins and Dr. Mircea Popescu of MDL for their many insights on how to best utilize the programming capabilities of the software.

Dr. Peng Zhang, who graduated in 2013 after laying a solid foundation and making

significant contributions to an earlier implementation of the electromagnetic CE-FEA, provided invaluable mentorship. I thank my colleague Ph.D. candidate Ahmad Hamidi for his early work on differential evolution optimization and for introducing me to the topic. I would like to extend my sincere appreciation for friendship and many good memories to my colleagues and friends from the UWM Power Electronics and Electric Drives Laboratory: Salam Bani-Ahmed, Zeljko Janovic, Emad Manla, Bora Novakovic, Mohammad Rashidi, Ashishkumar Solanki, and Luke Weber.

Last but definitely not the least, I would like to thank my parents, brother and sister-in-law for their patience and endless devotion. Without their constant support and encouragement throughout my studies, this work would never have come into existence.

CHAPTER 1

Introduction

1.1 Research background

Compared with induction machines, brushless permanent magnet (BLPM)and synchronous reluctance (SyncRel) machines, may have advantageous characteristics in terms of high efficiency, high overload and fault-tolerant capabilities, high torque and power density, as well as very wide constant power (field-weakening) operating range, and represent a preferred choice for many high efficiency, variable speed, and for electric traction applications [1]. As a result, the optimal design of electronically controlled synchronous machines currently represents a high-priority.

In order to accurately analyze the performance and optimize the design of electric machines, the electromagnetic, thermal, and air-flow problems have to be all considered according to a coupling mechanism in which the electromagnetic power losses are generating heat, leading to a non-uniform distribution of temperature inside the machine, which in turn yields further variations of the power losses. In particular, recent developments demonstrate that the thermal design can be rewarded by significant improvements in the overall machine performance [2]. The first part of the thesis is devoted to such topics.

Optimization techniques are required in order to address the major design challenges, which are typically considered to be cost versus performance for a large variety of design typologies of the BLPM type and the low power factor and relatively high torque ripple for SyncRel machines. Such problems, which have multiple and conflicting objectives, are studied in the second part of the thesis.

1.2 Electronically controlled PM and synchronous reluctance motors and drives

Vector (sinusoidal) control is the most common method for achieving synchronous machine variable speed operation. The structure of the synchronous machine controller (vector control controller) is shown in Figure 1.1, in which the magnitudes and angles of the space vectors, such as magnetic flux, current and voltage, are controlled in d-q coordinates [3]. The direct Park transformation:

$$T_s = \sqrt{\frac{2}{3}} \begin{bmatrix} \cos(\omega t) & \cos(\omega t - 2\pi/3) & \cos(\omega t - 4\pi/3) \\ -\sin(\omega t) & -\sin(\omega t - 2\pi/3) & -\sin(\omega t - 4\pi/3) \\ 1/2 & 1/2 & 1/2 \end{bmatrix}, \qquad (1.1)$$

where ω represents the $d-q$ frame rotational speed, provides the relationship between the abc and the $d-q$ reference frames.

The main advantage of using the dq synchronous reference frame is that three-phase AC variables can be represented by two-phase variables, and thus the modeling of the control loop and the design of the control variables becomes more convenient.

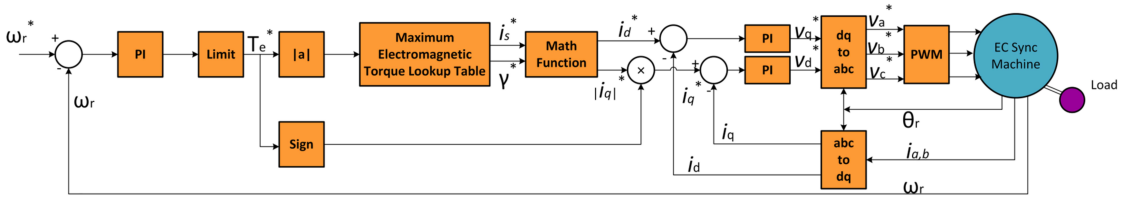

Figure 1.1: Generic control for electronically commutated synchrous machines.

At steady-state operation with constant speed and torque, the $d-q$ currents are constant.

In a generic implementation, two control loops, one inner for torque and one outer for speed, are employed and shown in Figure 1.1. Two conventional proportional integral (PI) controllers are utilized to control the speed and torque, and a look up table is employed to determine the optimal torque angle and current in order to obtain maximum electromagnetic torque. The stator voltage space vector is transformed back from the $d-q$ reference frame into the abc reference frame, which is fixed with respect to the stator, through the inverse Park transformation,

$$T_s^{'} = \sqrt{\frac{2}{3}} \begin{bmatrix} \cos(\omega t) & -\sin(\omega t) \\ \cos(\omega t + 4\pi/3) & -\sin(\omega t + 4\pi/3) \\ \cos(\omega t + 2\pi/3) & -\sin(\omega t + 2\pi/3) \end{bmatrix} . \tag{1.2}$$

The controller generates a 3-phase PWM voltage command and regulates the motor phase current to a quasi sine-wave as illustrated with experimental results in Figure 1.2. An important observation, which justifies a major assumption made in the electromagnetic field analysis, is that at steady state operation with modern controllers the currents can be assumed to be perfectly sinusoidal.

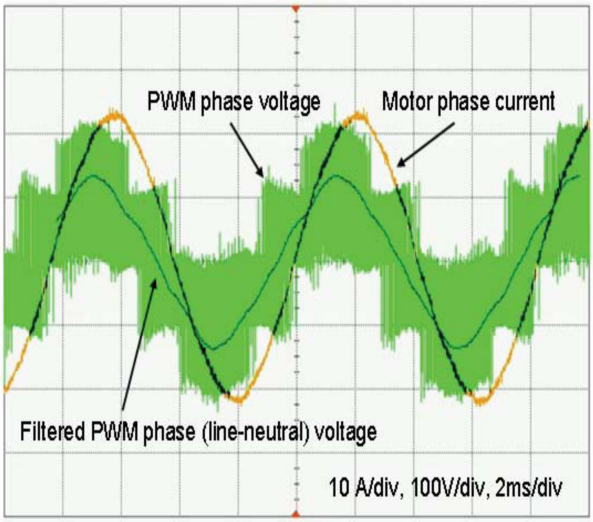

Figure 1.2: Voltage and current waveforms at steady-state operation for a sensorless vector controlled IPM motor drive [1].

1.3 Thesis layout

Chapter 1 introduces the research background for electronically controlled synchronous machines and outlines the main goals of this research. Literature reviews on BLPM and SyncRel machines, as well as on optimization methods are covered in this chapter.

Chapter 2 focuses on the theoretical fundamentals, including the electromagnetic finite element analysis (FEA), its computational efficient version, and thermal analysis. A novel iterative technique for coupled electromagnetic and thermal analysis is introduced and validated by comparison with experimental results in this chapter.

Chapter 3 covers the methodology and implementation of the automated multi-objective optimization utilizing the DE algorithm combined with CE-FEA method. DThe recommended approach of parameterized FEA models used for large scale optimization is presented in this chapter.

Chapter 4 discusses the optimization of an IPM machine prototype and of a SynRel machine prototype. Numerical results from different case studies are included together with experimental data, where available.

Chapter 5 concludes with a summary of work and original contributions. Suggestions for future work that can be extended based on the current research are also incorporated.

1.4 Literature review

1.4.1 Permanent magnet machines

By employing permanents magnets (PM) for excitation, a synchronous machine (PMSM) has the advantages of higher efficiency, power density and higher magnetic flux density in the air gap [4–9]. The performance at given inverter ratings of two types of PMSM, interior permanent magnet (IPM) and surface mounted permanent magnet (SPM) machines, as shown in Figure 1.3, were compared in [10]. According to Vagati, despite the fact of that SPM machine is easier to be manufactured, the good overload capability of IPM machine over the entire speed range makes the IPM

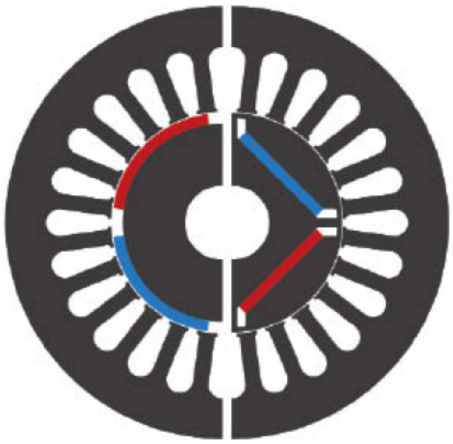

Figure 1.3: Schematic cross-section of a four-pole IPM machine (left) and of an interior PM motor (right). Magnets of different polarities are colored in red and blue, respectively. [11].

machine suitable for the application in which the rotor anisotropy is maximized.

In [12], three of the most popular topologies of IPM machine, flat-type, V-type and spoke-type, were investigated and two novel morphing parametric models for flat-to-V-type (FV) and for spoke-to-V-type (SV) IPM machine configuration were introduced. As shown in Figure 1.4, the robust parametric model can geometrically morph between the flat-type and V-type IPM layouts. Another morphing study is between the spoke-type and V-type IPM, as shown in Figure 1.5. This morphing study was based on a robust parametric model, which is an essential requirement of the large scale optimization and will be later described in more details.

Compared with the flat-type IPM machine, the V-type machine could be, in principle, more suitable for high speed, flux-weakening constant-power operation, hybrid and electric vehicle applications due the higher saliency ratio and lower PM losses.

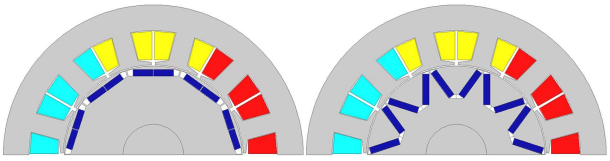

(a) Flat-type (b) V-type

Figure 1.4: Morphing cross-sections of the FV-PM layout parametric model [12].

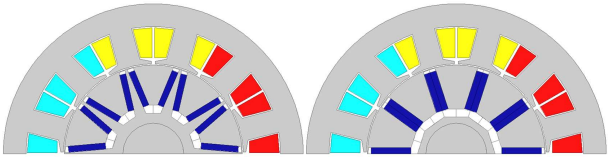

(a) V-type (b) Spoke-type

Figure 1.5: Morphing cross-sections of the SV-PM layout parametric model [12].

Spoke-type IPM machines have the advantage of magnetic flux concentration, so that in high-polarity motors, the flux density in the motor air-gap and the specific power output are increased. This leads the way to further performance improvement and size reduction [11, 13].

1.4.2 Synchronous reluctance machines

Three types of rotor geometry, 3C, 3U and I2U, are described in [14] and [15], as shown in Figure 1.6. The investigation indicates that the I2U geometry can have the same performance as the 3C topology and that the I2U design is superior to the 3C type from the point of view of mechanical aspects, such as reducing the stress in the structural ribs and the moment of inertia.

In reference [16], the influence of the number combinations of stator slots and

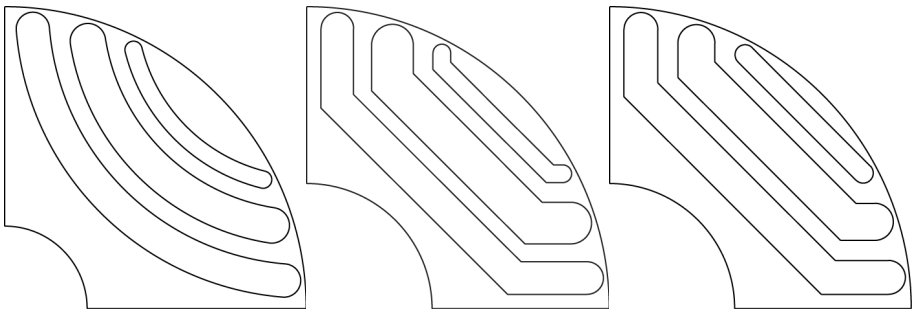

(a) Round barriers (3C) (b) 3U angled barriers (c) I2U angled barriers

Figure 1.6: Different shapes of the flux barriers in SyncRel rotors [14]

.

rotor poles together with the number of flux-barrier layers on the performance of the SynRel machine with emphasis on output torque and torque ripple was investigated. In order to accurately estimate the impact of slot/pole number combinations on performance of SynRel machine, the same ratio of rotor insulation width to the rotor iron width has been used for all the slot and pole number combinations machines. The investigation indicates that average torque decreases with the increase of the pole numbers but remain almost constant when employing different stator slot numbers but with the same pole number. In addition, the torque ripple decreases significantly with the increase of the stator slot number and the SynRel machines with three- and four-layer flux-barrier in the rotor have the lowest torque ripple and slightly smaller average torque than the machine with double-layer flux-barrier which has the biggest average torque and highest torque ripple.

The physical nature as well as measurements from efficiency point of view for the SynRel machine and its correspondent induction machine (IM) are briefly compared

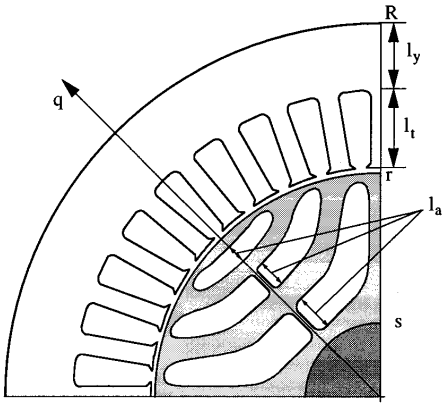

Figure 1.7: Schematic cross-section of a SyncRel with a transverse-laminated rotor [17].

in [18] and [19]. Study shows that by using SynRel machine rotor instead of the IM, the machine efficiency can be improved by 1.5-5%-unit for the power range 90-1.1 [kW] respectively. The major drawback of SyncRel machine is the power factor is lower in comparison to its counterpart IM. A specific SynRel machine with multiple barrier structure was investigated. The overload capacity of the SynRel machine could reach up to 3 times of the nominal load with suitable control. In addition, the air gap length sensitivity analysis suggests keeping air gap length as small as possible. The effect of saturation on machine performance was discussed as well. Generally, saturation increased the maximum torque per ampere (MTPA) optimal current angle beyond 45deg, but it did not have a strong effect on power factor (PF) at least up to the nominal current.

In reference [21], [22] and [17], transverse-laminated type of rotor, as shown in Figure 1.7 is referred from both theoretical and practical points of view. In addition,

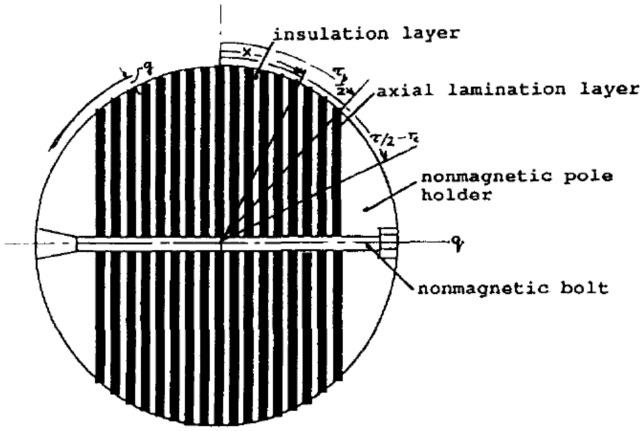

Figure 1.8: A two-pole ALA-rotor with single axial lamination/insulation layers [20].

the concept of separation points between adjacent segments is introduced to represent the rotor iron ribs, which are saturated by stator magneto-motive force (MMF), thus allowing different segments to have different magnetic potentials. When a 5%-10% ripple is tolerated by the application, this result can be achieved without rotor skewing, which represents an additional saving in motor cost, particularly in the case of mass production. In addition, the quadrature reactances are compared, as affecting overload and flux-weakening performances. Last, applicative considerations are given, thus defining the most suitable solution for each field.

A 2-pole, 2.0 hp laboratory axially laminated anisotropic (ALA) rotor structure with high Ld/Lq ratio of 16 under rated magnetic saturation conditions, high power factor of 0.91 was proposed in reference [20], as shown in Figure 1.8. The single lamination/insulation layers are assembled through only three nonmagnetic bolts for

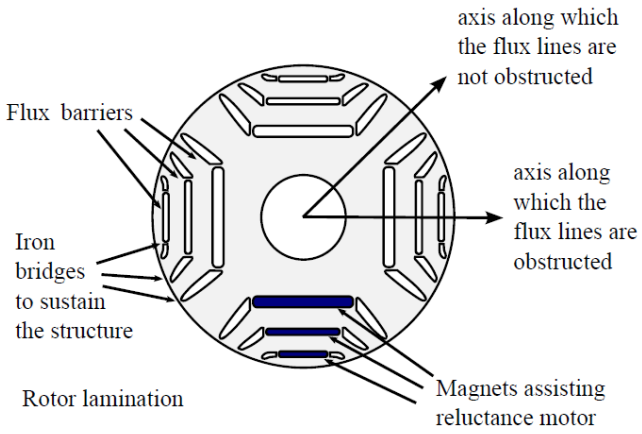

Figure 1.9: Four-pole transversally-laminated PMaSyncRel rotor with three flux barriers per pole [23].

mechanical integrity of the rotor. They do not affect or degrade the magnetic characteristics of the ALA rotor. This configuration reduces the cogging torque and yields $Ld/Lq > 16$, which is much higher than those reported in other publications.

According to Bianchi and Toliyat, SyncRel machines have a drawback of high torque ripple due to the interaction between the spatial harmonics of MMF and the rotor structure [23–26]. When PMs are inserted within the flux barriers, as shown in Figure 1.9, the iron bridges are saturated and power factor is improved. In this case, the SyncRel machine becomes a permanent magnet assisted synchronous reluctance (PMaSyncRel) machine.

1.4.3 Machine design optimization

The implementation of design optimization with multi-objectives for electric machines has been developed recently [12, 27–32]. In [29], a combined design optimization method utilizing Design of Experiments (DOE) and Differential Evolution (DE) algorithms was implemented to optimize a 12-slot, 8-pole, spoke-type, ferrite magnet machine, with fractional-slot concentrated windings. According to Zhang *et al*, DOE techniques combined with Response Surface (RS) methodology are suitable for local design optimization problems with a limited number of geometric design variables, and DE algorithms are suitable for large scale optimization with a significant number of geometric design variables.

In [33], a benchmark study comparing RS and DE algorithms on a permanent magnet synchronous machine design optimization seeking the minimization of total weight and maximization of a goodness function, which is the ratio between the shaft torque and the square root of total power losses, was presented. The results obtained by using DE are compared with the RS method when the optimization employs only a small number of candidate designs. The numerical results point out the superiority of the DE algorithms when more design variables (candidate designs) are considered. Among the various stochastic optimal search methods, such as Genetic Algorithms (GAs) [34, 35], Simulated Annealing (SA), Particle Swarm Optimization (PSO), Differential Evolution (DE), DE and GA are the most popular algorithms for

the electric machine design optimization [27, 28, 36–45].

The DE algorithm was combined with an ultrafast nonlinear electromagnetic FE technique, previously introduced in [46, 47] and further developed under the name of Computationally Efficient FEA (CE-FEA) [30, 38, 40, 48] to implement the multi-objective optimization problem. The CE-FEA method could estimate the sine-wave current regulated performance of synchronous machines, including induced voltage waveforms, average and ripple torque, inductances, and power losses by exploiting the slot-pitch symmetry of the stator magnetic circuit and the periodicity of the electromagnetic field, only uses a minimum number of magnetostatic FE solutions to substantially reduce the computational effort by up to two orders of magnitude.

In reference [49], the automatic design of SynRel machines is considered by means of Finite Element Analysis and Multi-Objective Optimization Algorithms (MOOA). Three popular MOOAs: Multi-Objective Genetic Algorithm (MOGA), Multi-Objective Differential Evolution (MODE) and Multi-Objective Simulated Annealing (MOSA), have been compared, and Differential Evolution gives the best results in terms of time to converge and repeatability of the results. The two objectives to be optimized are the average torque and the torque ripple. Except for the geometric inputs for the circular layers, the phase angle of the current vector in (d,q) synchronous coordinates is also considered in the optimization variables. The current amplitude selected in the examples is twice the machine rated current since the preliminary investigations

revealed that machines with a good torque/torque ripple compromise at overload perform well also at lower current levels, but not vice-versa [14]. A random offset $\Delta\theta_0$ was introduced to simulate the motor positions to overcome the problem of the certain harmonic of the torque ripple aliasing.

CHAPTER 2

Coupled Electromagnetic and Thermal Modeling of Synchronous Machines

2.1 Electromagnetic field models and finite element analysis

The preferred approach for modeling the steady-state operation of a sine-wave current regulated synchronous PM machine with rotating magnetic field is through a succession of magnetostatic solutions, commonly referred to as "snap-shots", which correspond to different time instances, rotor positions and stator current distributions [27, 30, 46, 47].

The magnetostatic field is governed by a subset of the Maxwell equations, which includes the reduced form of Ampere's law:

$$\nabla \times H = J \ , \tag{2.1}$$

and the reduced form of Gauss's law:

$$\nabla \cdot B \ = \ 0 \ . \tag{2.2}$$

The magnetic non-linearity of the material is modeled as:

$$B = B_r + \mu(B)H, \tag{2.3}$$

where the remanence B_r has non-zero values only in the PMs.

Because the magnetostatic fields are solenoidal they can be studied by using a magnetic vector potential (MVP), which is defined as:

$$\nabla \times A = B \tag{2.4}$$

In combination with the Coulomb gauge condition

$$\nabla \cdot A = 0 \tag{2.5}$$

and Gauss' magnetic flux law (2.2), the above (2.4) yields to the magnetic vector potential equation

$$\nabla \cdot (\nabla \times A) \equiv 0 \ . \tag{2.6}$$

The combination of previous equations, results in the Poisson vectorial equation:

$$\nabla \times \left(\frac{1}{\mu} \nabla \times A \right) = J + \left(\frac{1}{\mu} \nabla \times B_r \right). \tag{2.7}$$

The above equation with non-linear magnetostatic fields and isotropic materials can be transferred to:

$$\frac{\partial}{\partial x} \left(\frac{1}{\mu} \frac{\partial A}{\partial x} \right) + \frac{\partial}{\partial y} \left(\frac{1}{\mu} \frac{\partial A}{\partial y} \right) = -J - \left[\frac{\partial}{\partial x} \left(\frac{B_{r,y}}{\mu} \right) - \frac{\partial}{\partial y} \left(\frac{B_{r,x}}{\mu}) \right) \right]. \tag{2.8}$$

In electric machine problems, anti-periodic or periodic boundary conditions are employed to reduce the cross-sectional field analysis to an odd or an even number of poles, respectively:

$$A(r, \theta) = -A \left[\theta + \frac{(2k-1)\pi}{p} \right], \quad A(r, \theta) = -A \left[\theta + \frac{2k\pi}{p} \right], \tag{2.9}$$

where p is the number of pole pairs and r, θ are polar coordinates.

Finite Element Analysis (FEA) uses a complex system of nodes, which serve as a grid basis for subdividing the field region into a mesh of smaller elements [50, 51]. As shown in Figure 2.1, in a point P, which is located within element e, the magnetic vector potential is calculated as a function of A in the np nodes of the respective element and the shape function N:

$$A^e(P) = \sum_{i=1}^{np} N_i^e(P) A_i^e. \tag{2.10}$$

Triangular elements of the first or second order are typically employed in FEA models of electric machines. The first-order elements, $np = 3$, have three nodes, i, j, k, placed in the three verticals as shown in Figure 2.1. The second-order elements have 3 nodes at the verticals and another 3 on the mid-points of each edge.

The shape functions for the first-order elements are:

$$N_i^e(x, y) = \frac{1}{2\Delta^e}(a_i^e + b_i^e x + c_i^e y),\ i = i, j, k \tag{2.11}$$

where

$$\Delta^e = \frac{1}{2}\begin{vmatrix} 1 & x_i^e & y_i^e \\ 1 & x_j^e & y_j^e \\ 1 & x_k^e & y_k^e \end{vmatrix} \tag{2.12}$$

$$\begin{bmatrix} a_i^e & b_i^e & c_i^e \\ a_j^e & b_j^e & c_j^e \\ a_k^e & b_k^e & c_k^e \end{bmatrix} = \begin{bmatrix} x_j^e y_k^e - x_k^e y_j^e & y_i^e - y_k^e & x_k^e - x_j^e \\ x_k^e y_i^e - x_i^e y_k^e & y_k^e - y_i^e & x_i^e - x_k^e \\ x_i^e y_j^e - x_j^e y_i^e & y_i^e - y_j^e & x_j^e - x_i^e \end{bmatrix} \tag{2.13}$$

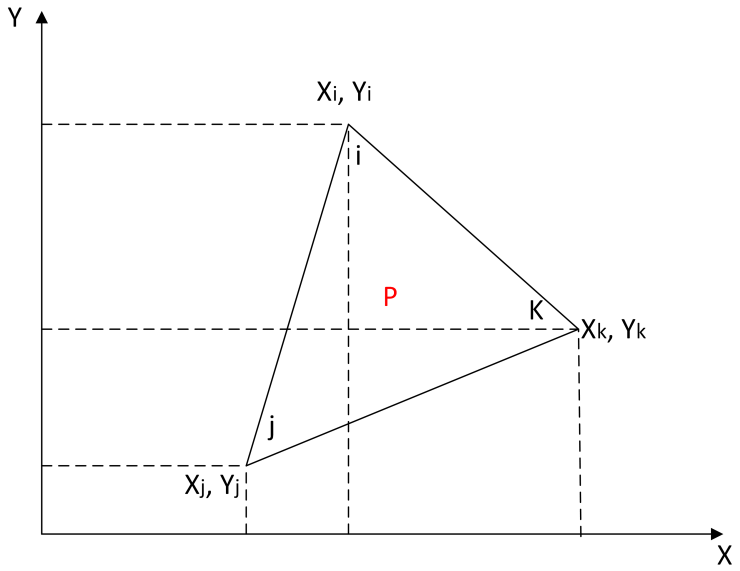

Figure 2.1: Triangular finite element in the xy plane.

For the first-order triangular elements the approximation model for the magnetic vector potential is provided by:

$$A^e(x,y) = \sum_i^k N_i^e(x,y) A_i^e = [N_e]\{A^e\}, \tag{2.14}$$

$$B_x^e = \frac{\partial A^e}{\partial y} = \frac{1}{2\Delta^e} \sum_i^k c_i^e A_i^e = ct \ , \tag{2.15}$$

$$B_y^e = -\frac{\partial A^e}{\partial x} = -\frac{1}{2\Delta^e} \sum_i^k b_i^e A_i^e = ct \ , \tag{2.16}$$

where the summation is performed for $i = i, j, k$ and the superscript identifies the element.

The general form of the magnetostatic field functional is derived from the energy

density as:

$$\mathcal{F} = \int_{\Omega} \left[\int_{0}^{B} \frac{1}{\mu(B)} (B - B_r dB - JA) \right] d\Omega \ . \tag{2.17}$$

For 2D fields, the above equation reduces to:

$$\mathcal{F} = \int_{D} \left\{ \frac{1}{2\mu} \left[\left(\frac{\partial A}{\partial x} \right)^2 + \left(\frac{\partial A}{\partial y} \right)^2 \right] - \left\{ J - \left[\frac{\partial}{\partial x} \left(\frac{B_{r,y}}{\mu} \right) - \frac{\partial}{\partial y} \left(\frac{B_{R,X}}{\mu} \right) \right] \right\} \right\} dxdy. \tag{2.18}$$

This functional is minimized with respect to the unknown magnetic vector potential A over a finite element a mesh with n_t nodes:

$$\frac{\partial \mathcal{F}^e}{\partial A_i} = \sum_{e}^{m_i} \frac{\partial \mathcal{F}}{\partial A_i^e} = 0, \ i = 1, 2, \cdots, n \ , \tag{2.19}$$

where the summation is performed for the m_i elements that have the i node common.

An algebraic system of non-linear equations is obtained:

$$\sum_{e}^{m_i} \sum_{\lambda=i,j,k} K_{i\lambda}^e A_\lambda^e + \sum_{e}^{m_i} G_i^e = 0, \ i = 1, \cdots, n \tag{2.20}$$

with the coefficients:

$$K_{i\lambda}^e = \frac{1}{4\Delta^e \mu(B)} \left[c_i^e c_\lambda^e + b_i^e b_\lambda^e \right], \ \lambda = i, j, k \tag{2.21}$$

$$G_i^e = -\frac{1}{3} \Delta^e J^e + \frac{1}{2} \left[\frac{b_i^e B_{r,y}^e}{\mu_m^e(B^e)} - \frac{c_i^e B_{r,x}^e}{\mu_m^e(B^e)} \right] \tag{2.22}$$

Based on the magnetic vector potential solution, the x and y components of the magnetic flux density are derived from the previous equations and the radial and tangential components can be calculated as:

$$B_r(r, \theta) = B_x \cos\theta + B_y \sin\theta \tag{2.23}$$

$$B_t(r,\theta) = -B_x \sin\theta + B_y \cos\theta \tag{2.24}$$

The flux linkage per turn and per unit along the axial length through a coil with the sides C_1 and C_2 is computed as the difference between the weighted average (surface integral divided by area) of the magnetic vector potential in the coil sides:

$$\Psi_{C_1,C_2} = \frac{1}{S_{C_1}} \int_{C_1} Ads - \frac{1}{S_{C_2}} \int_{C_2} Ads. \tag{2.25}$$

The energy and the coenergy per unit of axial length, respectively, are:

$$W_m = \int_S (\int_0^B HdB) ds \tag{2.26}$$

$$W_m^* = \int_S (\int_0^H BdH) ds \tag{2.27}$$

The electromagnetic torque per unit of axial length can be calculated with the Maxwell stress tensor:

$$T_e = \frac{D_g}{2\mu_0} \int_0^{\pi D_g} B_r B_\theta d\ell \ , \tag{2.28}$$

where D_g is the air-gap diameter, or can be computed through the virtual work theory by differentiating the energy with respect to the angular coordinate at constant flux linkage:

$$T_e = -\frac{\partial W}{\partial \theta}|_{\Psi=const}. \tag{2.29}$$

2.2 Computationally efficient-finite element analysis

2.2.1 Construction of waveforms

For permanent magnet synchronous machines (PMSM) which employ sine-wave current supply, the symmetry of the geometry and electric circuit will result in the following expressions [48]:

$$A_{a+}(\theta + 60^\circ) = -A_{b+}(\theta) \ , \tag{2.30}$$

$$A_{a+}(\theta + 120^\circ) = A_{c+}(\theta) \ , \tag{2.31}$$

where A is the average magnetic vector potential(MVP) in the a, b, c coil sides. Then the tooth flux Φ and the phase flux linkage λ can be expressed as follows:

$$\Phi_a(\theta) = l_{Fe}(A_{a+}(\theta) - A_{a-}(\theta)) \ , \tag{2.32}$$

$$\lambda_a = N_{ph}\Phi_a(\theta) \ , \tag{2.33}$$

where l_{Fe} is the effective stack length and N_{ph} is the number of series turns per phase.

Flux linkages λ in Fourier series form is:

$$\lambda_a(\theta) = \sum_{n=1}^{n_M} \lambda_n cos(n\theta + \phi_n) \ , \tag{2.34}$$

where n_M is the maximum harmonic order and ϕ_n is the phase angle of the flux linkage for the n^{th} harmonic. The corresponding back EMF in Fourier form is:

$$e_a(\theta) = -\frac{d\lambda_a}{d\theta}\frac{d\theta}{dt} = \omega \sum_{n=1}^{n_M} n\lambda_n cos(n\theta + \phi_n). \tag{2.35}$$

Figure 2.2 demonstrates the construction technique for the flux linkage waveform. In order to obtain the flux linkage waveform of one electrical cycle of phase A, firstly the flux linkages of phase B and phase C are phase shifted by 60° and 120°, respectively. The remainder of the flux linkage waveform, between 180° and 360°, is obtained by symmetry.

Similar with the construction of the flux linkage, the flux density waveforms in the stator teeth and yoke can be reconstructed as well. The Fourier series of the elemental flux densities can be created as follows:

$$B_{r,t}(\theta) = \sum_{n=1}^{n_M} B_n cos(n\theta + \phi_n). \tag{2.36}$$

When implementing the CE-FEA method with ANSYS Maxwell software packages, the torque profiles could be estimated with the Fourier analysis conducted on the torque profile obtained from a single CE-FEA evaluation:

$$T_e(\theta) = T_{avg} + \sum_{n=6,12} T_n cos(n\theta + \phi_n). \tag{2.37}$$

Figure 2.3 demonstrates the construction technique of torque waveform. The torque waveform of one electrical cycle is obtained by repeating the torque waveform for the 1/6 electrical cycle six times.

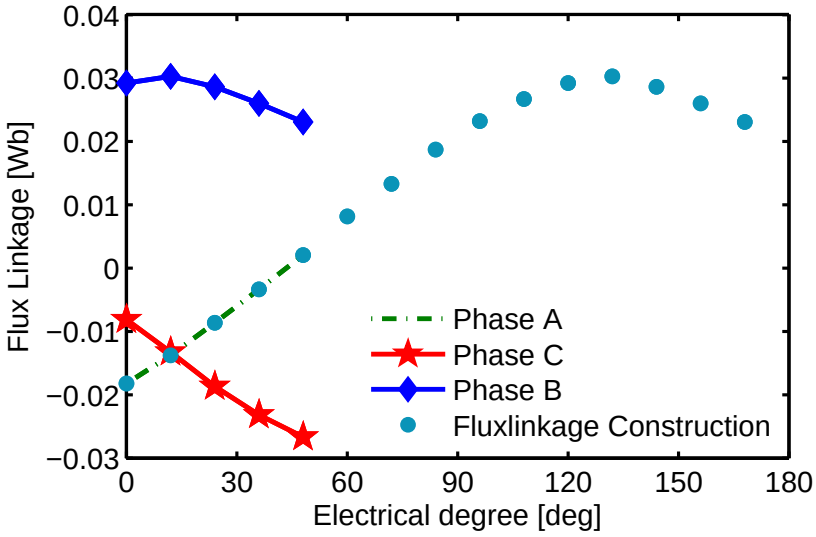

Figure 2.2: Flux linkage construction according to CE-FEA.

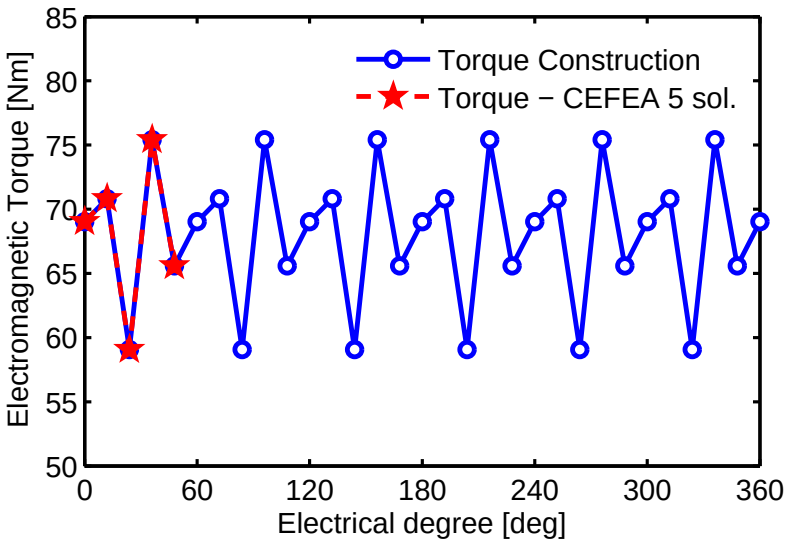

Figure 2.3: Electromagnetic torque waveform construction according to CE-FEA.

2.2.2 Inductance and torque angle calculation for MTPA

The design and analysis of PMSMs are based on the assumption that such machines are running at the maximum torque per ampere (MTPA) load condition. To accurately estimate the performance of electric machine, it is essential to estimate the torque angle for such a load condition [30].

The phasor diagram

The theory of the 2-phase equivalent circuit model (d-q model) is applied for the analysis of motors including PM SM, IM, SyncRel etc. In the rotor reference frame, the direction of the permanent magnet flux is defined as the d-axis, while the q-axis is 90 electrical degrees ahead of the d-axis. Thus the direction of back-emf phasor E aligns with the q-axis.

In the steady state operation with balanced sinusoidal three-phase currents supply, IPM motors can be modeled with the phasor diagram shown in Figure 2.4a. From the diagram, the current phasor leads the d-axis by an angle γ, sometimes known as the "Torque angle". The terminal voltage phasor V leads the q-axis by the angle δ, sometimes known as the "load angle", and the angle between the voltage phasor and the current phasor is defined as "power factor angle" ϕ. Based on Figure 2.4a, the

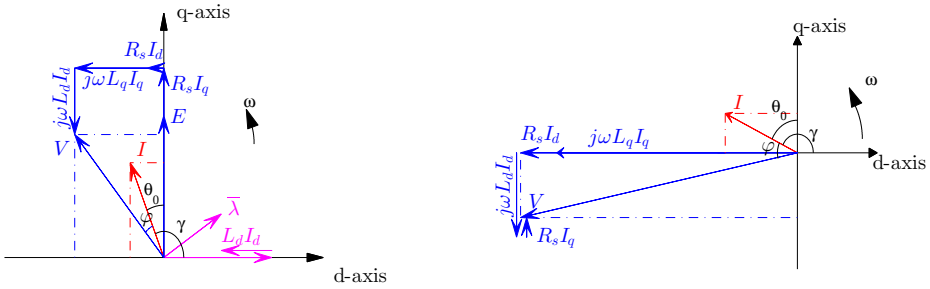

(a) PM machine (b) SynRel machine

Figure 2.4: Synchronous machine phasor diagram expressed in rotor reference frame.

d-axis and q-axis flux linkages, λ_d and λ_q, of the PM machines are:

$$\begin{cases} \lambda_d = \lambda_{PM} + L_d i_d \\ \lambda_q = L_q i_q \end{cases} \tag{2.38}$$

where $\lambda_P M$ is the PM flux linkage, Ł$_d$ and Ł$_q$ are the d-axis and q-axis inductances. Here, ı$_d$ and ı$_q$ are the d-axis and q-axis currents

Maximum torque per ampere (MTPA)

The electromagnetic torque developed by the PM machine is:

$$T_e = \frac{3}{2}\frac{p}{2}(\lambda_d i_q - \lambda_q i_d), \tag{2.39}$$

where P is the number of poles.

Substituting (2.38) into the above equation:

$$T_e = \frac{3}{2}\frac{p}{2}(\lambda_{PM} i_q + (L_d - L_q) i_d i_q). \tag{2.40}$$

When a PM machine is running under the MTPA load condition, substituting $i_d = I\cos(\gamma)$ and $i_q = I\sin(\gamma)$ into (2.40), the electromagnetic torque is reformulated

as follows:

$$T_e = \frac{3}{2}\frac{p}{2}(\lambda_{PM} I sin(\gamma) + (L_d - L_q) I^2 sin(\gamma) cos(\gamma)) \ , \tag{2.41}$$

Equating the derivative of the electromagnetic torque expression to zero yields the angle that gives maximum torque as follows:

$$\frac{dT_e}{d\gamma} = \frac{3p}{4}[\lambda_{PM} I cos(\gamma) + (L_d - L_q) I^2 (2cos^2(\gamma) - 1)] = 0. \tag{2.42}$$

Solving for γ from (2.42), one can express the torque angle for the MTPA load condition as follows [52]:

$$\gamma = \arccos\left(\frac{-\lambda_{PM} I + \sqrt{\lambda_{PM}^2 I^2 + 8(L_d - L_q)^2 I^4}}{4(L_d - L_q) I^2}\right). \tag{2.43}$$

Inductance calculation

This section introduces two different methods to calculate the PM flux linkage λ_{PM} and dq-axes inductances, which are required in order to estimate the torque angle with (2.43). For the purpose of the transformation from abc-frame to dq-frame, Parks transformation is employed [53]:

$$T_s = \frac{2}{3}\begin{bmatrix} cos(\theta) & cos(\theta - 2\pi/3) & cos(\theta - 4\pi/3) \\ -sin(\theta) & -sin(\theta - 2\pi/3) & -sin(\theta - 4\pi/3) \\ 1/2 & 1/2 & 1/2 \end{bmatrix} \ , \tag{2.44}$$

where, $\theta = \theta_0 + \omega t$, is as shown in the phasor diagram from Figure 2.5. Here, θ_0 is the rotor initial position, ωt is the electrical speed.

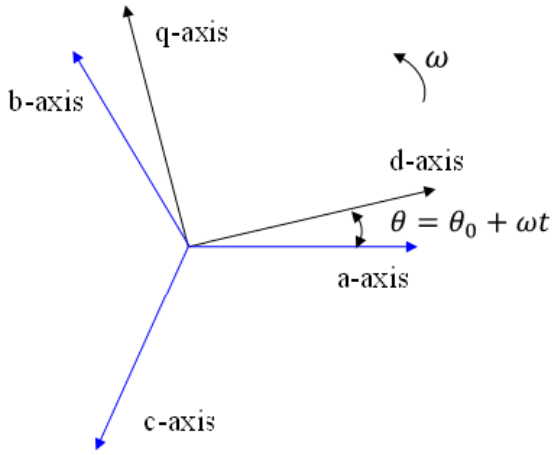

Figure 2.5: Phasor diagram of abc- and dq-reference frames.

Method 1: inductances transformation from abc-phase to dq-frame

Assume that the PMSM is running at 90° torque angle. Under this load condition:

$$i_d = 0, \tag{2.45}$$

$$i_q = I, \tag{2.46}$$

$$\lambda_{PM} = \lambda_d. \tag{2.47}$$

Substitute (2.45), (2.46) and (2.47) into (2.39):

$$T_e = \frac{3}{2}\frac{p}{2}\lambda_{PM} I. \tag{2.48}$$

From (2.48), the flux linkage of the permanent magnets can be calculated as:

$$\lambda_{PM} = T_e/(\frac{3}{2}\frac{p}{2}I)\ , \tag{2.49}$$

where T_e is the electromagnetic torque when the motor operates under the 90° torque

angle load condition, while the flux linkage of permanent magnets, λ_{PM}, calculated by (2.49) will be constant.

The three-phase self and mutual inductance profiles can be expressed as:

$$\begin{cases} L_{aa}(\theta) = L_{sa} + L_{sv}\cos(2\theta) \\ L_{bb}(\theta) = L_{sa} + L_{sv}\cos(2\theta - 4\pi/3) \\ L_{cc}(\theta) = L_{sa} + L_{sv}\cos(2\theta - 2\pi/3) \\ L_{ab}(\theta) = -L_{ma} + L_{mv}\cos(2\theta - 2\pi/3) \\ L_{bc}(\theta) = -L_{ma} + L_{mv}\cos(2\theta) \\ L_{ca}(\theta) = -L_{ma} + L_{mv}\cos(2\theta - 4\pi/3) \end{cases} \tag{2.50}$$

The previous profiles exemplify the self and mutual inductance variations versus the rotor angular position within a complete electric cycle. It should be noted that the inductance calculation function in the ANSYS Maxwell must be enabled to calculate the self and mutual inductances. According to Park's transformation, d-axis and q-axis inductances are:

$$\begin{bmatrix} L_d & 0 & 0 \\ 0 & L_q & 0 \\ 0 & 0 & L_0 \end{bmatrix} = T_s \begin{bmatrix} L_{aa} & L_{ab} & L_{ac} \\ L_{ba} & L_{bb} & L_{bc} \\ L_{ca} & L_{cb} & L_{cc} \end{bmatrix} T_s^{-1} \tag{2.51}$$

With L_d, L_q from (2.51) and λ_{PM} from (2.49), one can obtain the torque angle under the MTPA load condition by substituting them into (2.43).

Method 2: dq-frame formulation of flux linkages and currents

This method is based on the dq-frame formulation of flux linkages and currents expressed as (2.38). One can obtain the expression of d-q inductances from (2.38):

$$\begin{cases} L_d = (\lambda_d - \lambda_{PM})/i_d \\ L_q = \lambda_q / i_q \end{cases} . \tag{2.52}$$

When the simulation model operates at 90° torque angle, the d-axis current is equal to zero. Through Park's transformation, the flux linkage of permanent magnets can be expressed as follows:

$$\lambda_{PM} = \lambda_d = \frac{2}{3}[cos(\theta)\lambda_a + cos(\theta - 2\pi/3)\lambda_b + cos(\theta - 4\pi/3)\lambda_c]. \tag{2.53}$$

When the simulation model operates at 120°, another set of abc-frame flux linkages and currents can be obtained. One can obtain the dq flux linkages and currents through Park's transformation:

$$\begin{bmatrix} \lambda_d \\ \lambda_q \\ \lambda_0 \end{bmatrix} = T_s \begin{bmatrix} \lambda_a \\ \lambda_b \\ \lambda_c \end{bmatrix} \tag{2.54}$$

$$\begin{bmatrix} i_d \\ i_q \\ i_0 \end{bmatrix} = T_s \begin{bmatrix} i_a \\ i_b \\ i_c \end{bmatrix} \tag{2.55}$$

Inductances calculated by the second method can be obtained by substituting (2.53), (2.54) and (2.55) into (2.52).

Inductances and torque angle for an IPM machine with 36 stator slots and 6 poles calculated by these two different methods are exemplified in Table 2.1.

Table 2.1: Comparison of permanent magnet flux linkage, torque angle, L_d and L_q calculated by two different methods.

	CE-FEA (Solutions=5)		CE-FEA (Solutions=7)	
	Method 1	Method 2	Method 1	Method 2
Torque angle [degree]	20.47	18.61	20.46	18.59
PM Flux linkage [Wb]	0.2962	0.2996	0.2962	0.2997
L_d [mH]	3.3	2.2	3.4	2.2
L_q [mH]	7.4	5.8	7.5	5.8

2.2.3 Performance estimation

The general expression of the specific core losses is:

$$w_{Fe} = k_h f B^{\alpha} + k_e f^2 B^2 + k_a f^{1.5} B^{1.5} \ , \tag{2.56}$$

where w_{Fe} is the core losses in W/lb or W/kg, which is under sinusoidal field excitation of frequency f, and k_h, k_e, and k_a are the hysteresis, eddy-current and excess loss coefficients, respectively. Especially, α is the power exponent of the hysteresis losses and B is the field flux density.

In the CE-FEA method, it was assumed that $k_a = 0$ to estimate the core losses:

$$w_{Fe} = k_h(f, B) f B^{\alpha} + k_e(f, B) f^2 B^2 \ , \tag{2.57}$$

where, $k_h(f, B)$ and $k_e(f, B)$ are functions of the flux density, B, and the frequency, f.

The specific hysteresis losses and eddy-current losses in the stator teeth and yoke are [54]:

$$w_h = \sum_{n=1}^{n_M} k_h(B_n)(n f_1) {B_n}^2 \ , \tag{2.58}$$

$$w_e = \sum_{n=1}^{n_M} k_e(B_n)(nf_1)^2 {B_n}^2 \ , \tag{2.59}$$

where, f_1, is the fundamental frequency. The total core losses in the stator can be calculated as follows:

$$w_{Fe} = (w_{hT} + w_{eT})m_T + (w_{hY} + w_{eY})m_Y \ , \tag{2.60}$$

where, m_T and m_Y are the masses of the stator teeth and yokes, respectively. Through simulation results and experiment results, there is a coefficient for the core loss calculation.

With a constant phase current, I, the copper losses are affected by the winding temperature, T_w, through affecting the phase resistance, R, which is given as:

$$W_{Cu}(T_w) = 3R(20^\circ\text{C})[1 + 0.0039(T_w - 20^\circ\text{C})]I^2. \tag{2.61}$$

The efficiency η can be expressed in following equation:

$$\eta = \frac{P_{in}}{P_{out}}, \tag{2.62}$$

where P_{in} and P_{in} are the input and output powers, respectively.

From the balance of power point of view, we have:

$$P_{in} = P_e + W_{Cu} \ , \tag{2.63}$$

where P_e is the electromagnetic power and W_{cu}, see 2.61, is the copper loss. Shaft output power is

$$P_{out} = P_e - W_{Fe} - W_{wfm} = T_m\omega_m \ , \tag{2.64}$$

where W_{Fe} is the iron loss, T_m is the mechanical torque of shaft, W_{wfm} is the windage friction and mechanical loss of 5W. P_e is the electromagnetic power which is mainly supplied by the airgap, which can be expressed as follows:

$$P_e = T_e\omega_m = T_e\omega_e/N_{pp} = T_e 2n\pi/60 \ . \tag{2.65}$$

In (2.65), n is the rated speed, N_{pp} is the number of pole pairs, ω_e is the electrical angular speed, ω_m is the mechanical angular speed.

The power factor can be expressed as follows:

$$\cos\varphi = \frac{P_{in}}{S} = \frac{2\pi n}{60} \cdot \frac{T_e}{3VI} \ , \tag{2.66}$$

where S is the apparent power, V is the rms value of phase induced voltage.

The Goodness is defined as torque per root square of total losses W_T under the rated load condition, which is expressed as follows:

$$G_d = \frac{T_e}{\sqrt{W_T}}. \tag{2.67}$$

2.3 Thermal model analysis using equivalent circuit networks

The methods typically employed for the thermal analysis of electric machines are of two types: numerical field-based and lumped equivalent circuit thermal networks.

The thermal analysis using numerical methods can estimate the temperature distribution at any point in the computational domain, such that, in principle, more

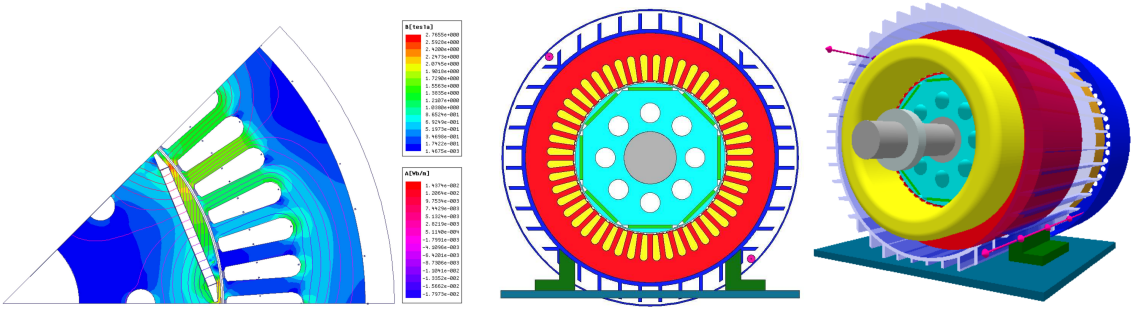

(a) Flux plot for the electromagnetic model.

(b) Radial cross-section of the thermal model.

(c) 3D thermal and air-flow model.

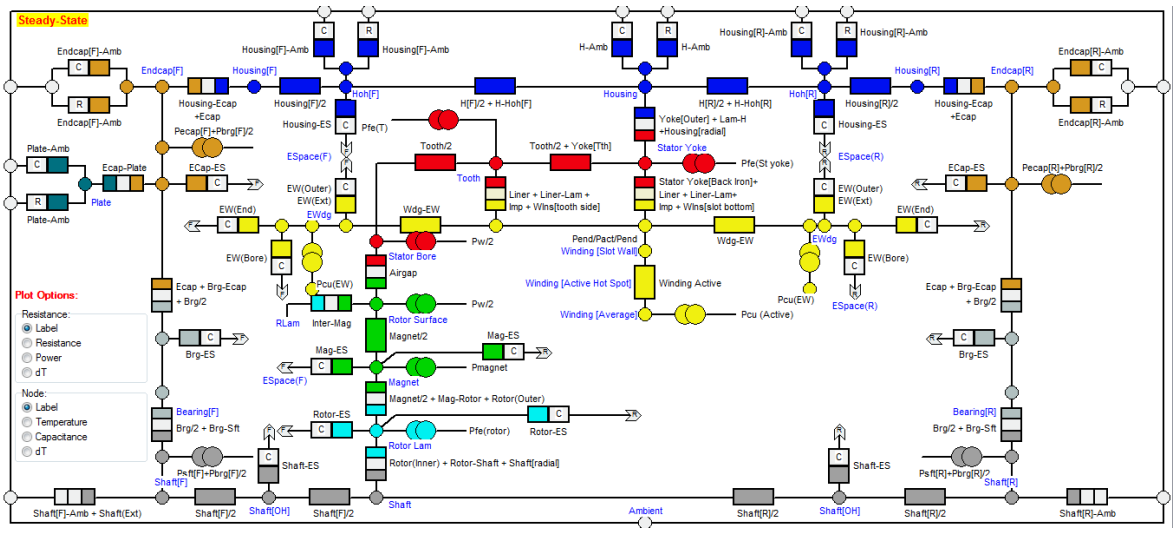

(d) Example steady-state heat transfer network for PM brushless machines.

Figure 2.6: Ultrafast multi-physics analysis employing ANSYS Maxwell2D and MotorCAD as computational engines, which are linked through a specially developed MATLAB scripting using ActiveX.

detailed and precise calculations are possible, leading to the identification of any critical "hot spots" in an electric machine. The most used combination of numerical methods employs FEA for the heat transfer in solid components and the computational fluid dynamics (CFD) to predict flow, especially in complex regions, such as the motor end windings [55].

Thermal-networks are very fast to calculate, but they pose major challenges for defining a circuit that accurately models the main heat-transfer paths. Furthermore, this method only provides a lumped distribution of temperatures, which may lack the details required to identify any "hot spots" [56, 57]. Nevertheless, due to its computational speed, this approach is preferred for large-scale optimization problems, which are implemented run on typical computing equipment employed in industry. Thermal-network analysis combines heat-transfer and air (or liquid coolant) flow modeling, which are as described in the following section.

For the 3D calculation of the temperature and air-flow distribution, a parametric machine model with a detailed equivalent network was developed (Figure 2.6d), and implemented using the scripting language of the Motor Design/Motor-CAD software, which was utilized as a computational engine [58]. This approach was previously demonstrated as achieving the best trade-off in terms of satisfactorily accurate estimations versus computational effort [59–61].

2.3.1 Heat-transfer analysis

The heat transfer is achieved through conduction, convection, and radiation. The equivalent heat-transfer network is similar with an electrical network.

Heat-transfer analysis is the thermal counterpart to electrical-network analysis with the following equivalences: nodal temperature differences to voltages, power losses to current sources, power flow through resistances to current, and thermal resistance to electric resistance. For steady-state models only thermal resistances are used as passive circuit elements to model the heat transfer paths within the machine.

An example thermal network, which includes thermal resistances for the stator back iron, tooth, winding hot-spot, etc, of an electric machine is shown in Figure 2.6d. Power loss are inputs at the corresponding nodes where losses occur.

For the steady-state models, only thermal resistances are used as passive circuit elements. Similarly with Ohm's law for electric circuits,

$$I = \frac{V}{R} \tag{2.68}$$

and, based on the previous analogy, the heat transfer is governed by the equation:

$$P = \frac{\Delta T}{R_T h} \ , \tag{2.69}$$

where P is the power in W, ΔT is the temperature difference rise in °C, h is the heat transfer coefficient in $W/m^2/°C$, and R_T is the thermal resistance $°C/W$ (see Figure 2.7). Due to the complex structure of electric machines, heat transfer takes place by

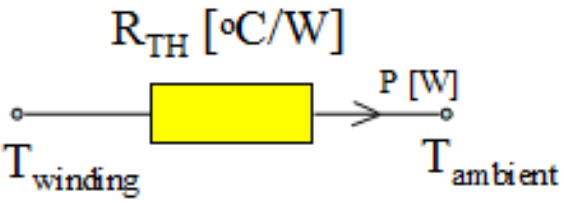

Figure 2.7: Explanatory for the equivalent thermal resistance [2]

.

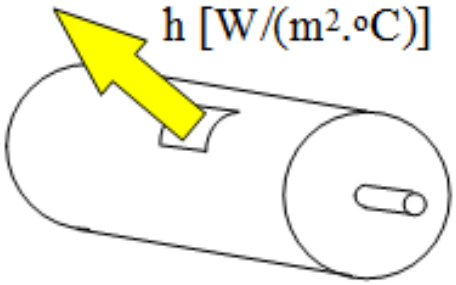

Figure 2.8: Explanatory for the heat transfer coefficient [2]

.

internal conduction through objects in contact, by convection to a fluid at external surfaces, and by non-linear radiation from one surface to another, as summarized in the following.

Conduction heat transfer

Conduction heat transfer in a solid is realized through molecule vibration [2]. This type of heat transfer takes place in between the winding copper and the adjacent stator teeth and back iron through multiple layers of winding insulation, or from the tooth and stator back iron to the stator bore and housing interface. Thermal conduction resistances can be estimated with:

$$R = \frac{L}{kA} \ , \tag{2.70}$$

where L [m] is the path length, A [m^2] is the path cross-section area and k [$W/m/^\circ C$] is the thermal conductivity of the material. Materials with well ordered crystalline structures have typically large values for the thermal conductivity. For example, the k for metals is in the range of 15-400$W/m/^\circ C$. Usually, good electrical conductors are also good thermal conductors. The solid electrical insulator, which is often porous, does not have a well ordered crystalline structure, and its thermal conductivity is typically in the range of 0.1-1$W/m/^\circ C$.

Convection heat transfer

Convection heat transfer, which is realized through fluid motion, includes natural convection and forced convection. Natural convection inside the electric machine is due to the buoyancy forces arising from density changing, which is caused by fluid motion in vicinity of the respective surface. Forced convection is caused by fluid motion produced with an additional device, such as a fan or a pump. Thermal convection resistances can be estimated as:

$$R = \frac{1}{h_C A} \ , \tag{2.71}$$

where A $[m^2]$ is the surface area and h_C $[W/m^2/^\circ C]$ is the convection heat transfer coefficient as shown in Figure 2.8. Convection heat transfer coefficient h_C for all convection surfaces could be predicted by using empirical correlations based on dimensionless numbers, such as Reynolds (Re), Grashof (Gr), Prandtl (Pr) and Nusselt (Nu). These numbers are functions of fluid properties, size (characteristic length), fluid velocity (forced convection), temperature (natural convection) and gravity (natural convection) [2].

Radiation heat transfer

Radiation heat transfer from a surface is realized through energy transfer by electromagnetic waves [2]. Radiation thermal resistances for a given surface can be estimated as follows:

$$R = \frac{1}{h_R A} \ , \tag{2.72}$$

where h_R [W/m^2/C] is the radiation heat transfer coefficient, which can be calculated by the following formula:

$$h_R = \sigma\varepsilon \times F_{1-2} \frac{T_1^4 - T_2^4}{T_1 - T_2} \ , \tag{2.73}$$

where, σ is the Stefan-Boltzmann constant ($5.669 \times 10 - 8\mathrm{W}/m^2/K_4$), ε is the emissivity of radiating surface ($\varepsilon \leq 1$), which is provided in most engineering textbooks [62] [63] [64]. The absolute temperature of radiating surface is denoted by T_1 [K], the absolute temperature of surface radiated to (ambient) is T_2 [K] and F_{1-2} is the view factor for dissipating surface 1 to the absorbing surface 2 (the ambient temperature for external radiation).

2.3.2 Flow-network analysis

A flow-network analysis is performed to predict the flow velocity for the local fluid (air or liquid) through the machine, This flow is a function of the forced convection

heat transfer from a given surface. Pressure, which drops due to duct wall friction and restrictions to flow (bend, expansion, contraction, etc.), can be calculated using the following expression:

$$P = RQ^2 \ , \tag{2.74}$$

where P, in Pa, is the pressure drop, Q is volume flow rate in m^3/s, and R is fluid-dynamic resistance in kg/m^7. The fluid-dynamic resistance is governed by the equation:

$$R = \frac{k\rho}{2A^2} \ , \tag{2.75}$$

where, ρ $[kg/m^3]$ is the air density, A $[m^2]$ is the flow area, and k is the dimensionless coefficient of local fluid resistance. Many empirical formulations are available in the technical literature to calculate the k factor for all changes in the flow section within the motors.

Figure 2.9 is an example of flow network for an electric machine. This is the fluid mechanics counterpart to electrical-network with the following equivalences: pressure drop to voltage, volume flow rate to current, and fluid-dynamic resistance to electrical resistance.

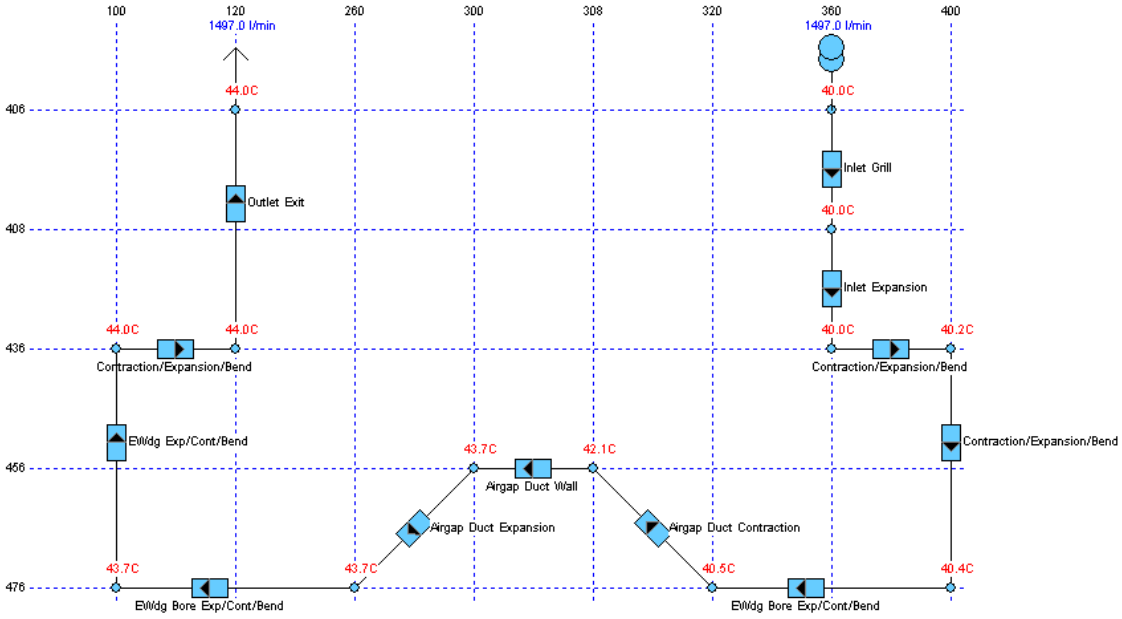

Figure 2.9: Example of flow network for an electric machine. Model created using the MotorCAD software [58].

2.4 Coupled analysis – strong and weak coupling

2.4.1 Principles

In the process of design optimization, it is essential to take into account both the electromagnetic and thermal aspects since the electromagnetic power losses are generating heat, leading to a non-uniform distribution of temperature inside the machine, which, in turn, yields further variations in the power losses [65].

For a more sophisticated coupling, several commercial software packages have been employed for the coupling between thermal analysis and electromagnetic models, as

shown in Figure 2.10. Electromagnetic analysis is performed through specially developed script algorithms that employ the ANSYS Maxwell software by ANSYS/Ansoft as the computational engine. An original implementation of the CE-FEA method, is employed to evaluate the performance and electromagnetic power losses. MotorCAD, which is a specialist analysis package for electric machines, is used to perform thermal analysis. ActiveX, a standard method for linking programs together and transferring data, is utilized to transfer geometric, loss, and temperature data between MotorCAD and ANSYS Maxwell.

To accurately compute the performance of the electric machine models, the temperature distribution is the results of the internal iteration and convergence which is automatically done by MotorCAD. MotorCAD will estimate the temperature distribution based on the input losses and then calculate the losses based on the temperature distribution again, until the losses calculated by the MotorCAD is approximately equal to the input losses from electromagnetic analysis. Finally, ANSYS Maxwell recalculates the losses with more accurate temperature distribution feedback from MotorCAD.

Due to the different parameter expressions in the ANSYS Maxwell software and MotorCAD software, the conversion of the parameter expressions is a necessary step in MATLAB scripting. Figure 2.11 is the example for the conversion between the parameters of the ANSYS Maxwell model and MotorCAD model. For instance, the

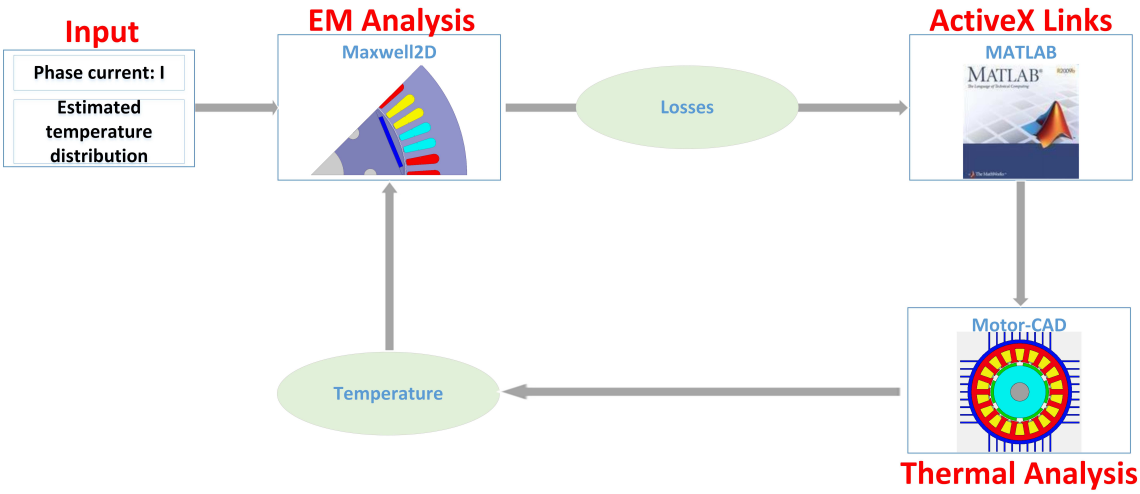

Figure 2.10: Schematic of software framework for coupling electromagnetic and thermal analysis of electric machines.

stator stack length is denoted by "L_{stk}" in Maxwell software and denoted by "Stator_Lam_Length" in MotorCAD software. The conversion of "Stator_Lam_Length=L_stk" in MATLAB can solve the differences of the parameter expressions for the electromagnetic and thermal analysis.

	Parameters Generic	Variable Name	CE-FEA Variable	Conversion Generic to CE-FEA	Motor-CAD Variable	Conversion Generic to Motor-CAD
Stator						
	Stator Outer Diameter	Dso	Rso	Rso=Dso/2	Stator_Lam_Dia	Stator_Lam_Dia=Dso
	Stator Inner Diameter	Dsi	Rsi	Rsi=Dso/2	Stator_Bore	Stator_Bore=Dso
	Tooth Width	Wt	WT	WT=Wt	Tooth_Width	Tooth_Width=Wt
	Slot Depth	Ds	Dss	Dss=Dss	Slot_Depth	Slot_Depth=Dss
	Slot Opening	Wso	Wso	Wso=Wso	Slot_Opening	Slot_Opening=Wso
	Tooth Tip Depth	TTD	TD	TD=TTD	Tooth_Tip_Depth	Tooth_Tip_Depth=TTD
	Slot Corner Radius	Rsc	Rsb	Rsb=Rsc	Slot_Corner_Radius	Slot_Corner_Radius=Rsc
	Stator stack length	Lstk	Lstk	Lstk=Lstk	Stator_Lam_Length	Stator_Lam_Length=Lstk
Rotor						
	Magnet Thickness	PMT	PMW	PMW=PMT	Magnet_Thickness	Magnet_Thickness=PMT
	Web Thickness	TW	BW	BW=TW	Web_Thickness	Web_Thickness=TW
	Shaft Diameter	Dsh	Rri	Rri=Dsh/2	Shaft_Dia	Shaft_Dia=Dsh
	Rotor stack length	Lrs	Lstk	Lstk=Lrs	Rotor_Lam_Length	Rotor_Lam_Length=Lrs
	Magnet Length	PML	PML	PML=PML	Pole_Arc	Pole_Arc
	Variable not in the CE_FEA (only in Motor CAD)					As per the MotorCAD ref. file
	Airgap	hg			Airgap	Airgap=hg
	Magnet Width Reduction	MWR			Magnet_Width_Reduction	Magnet_Width_Reduction=MWR
	Bridge Thickness	TB			Bridge_Thickness	Bridge_Thickness=TB
	Rotor Channel Diameter	Drc			RotorCircularDuctL1ChannelDiameter	RotorCircularDuctL1ChannelDiameter=Drc
	Housing Diameter	DH			Housing_Dia	Housing_Dia=DH
	Tooth Tip Angle	β			Tooth_Tip_Angle	Tooth_Tip_Angle=β
Quantity						
	Teeth per Pole	Nt	Nt	Nt=Nt	Slot_Number	Slot_Number=Nt*Np
	Poles	Np	P	P=Np	Pole_Number	Pole_Number=Np

Figure 2.11: Parameter conversions for the electric machine models in ANSYS Maxwell software and MotorCAD software.

2.4.2 Ultrafast coupling method

The conventional technique for iteratively coupling the electromagnetic and the thermal problems is depicted in Figure 2.12a and comprises one major loop. Iterations are performed until one or several error criteria, e.g. ϵ_w, ϵ_m, related to the initial and updated values of average temperature in the winding, T_w, and/or magnet, T_m, and/or to loss components, are met or a maximum limit is reached for the iteration counter. Although average values are specified for the temperature in the PM and winding, the thermal analysis employs a detailed network (see Figure 2.6d) and other temperatures can be used, if needed, in the iterative process.

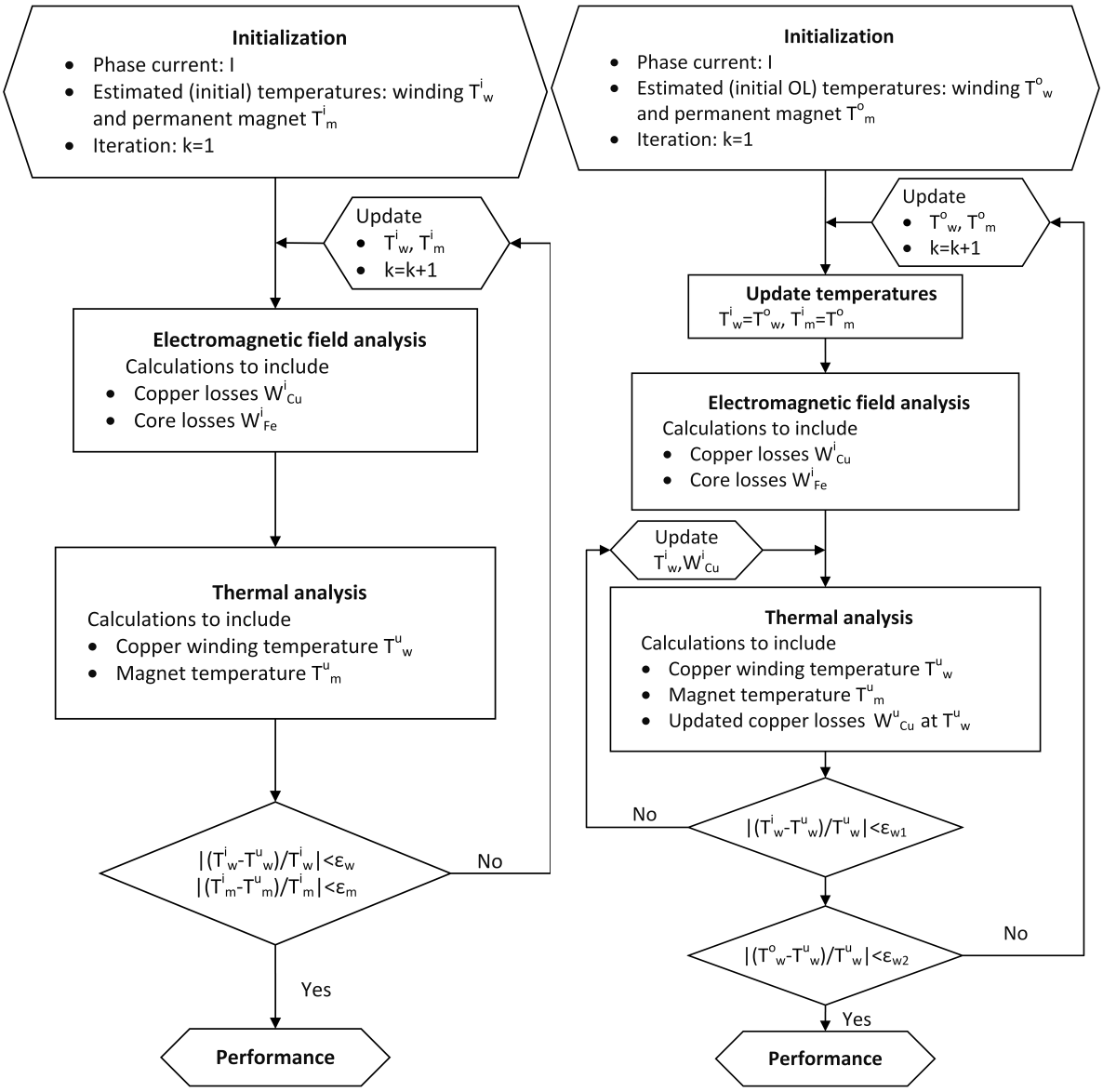

(a) Traditional approach (b) Proposed ultrafast approach

Figure 2.12: Flow charts for the iterative coupling of the electromagnetic and thermal, including air-flow, analysis. The new approach comprises a new thermal inner loop employing a simplified model for updating losses in order to significantly reduce the number of outer loops, which are substantially slower to calculate.

In the typical case, six or more iterations, each comprising electromagnetic and thermal analysis, have been reported in order to reach convergence [66]. Also, it should be noted that the computational efforts for the two problems are largely different. In the implementation previously described, the electromagnetic analysis of a motor design operating under steady-state condition is carried out in the order of tens of seconds, while the thermal and air-flow problem takes only seconds to solve.

The newly proposed technique from Figure 2.12b consists in partially decoupling the problems and introducing one extra inner loop around the thermal calculations, which are ultrafast. For this inner loop, the copper losses are simply updated using equation (2.61). In principle, the core losses could also be updated, using for example a simplified or a best fit model. However, this may not be practically needed, due to the fact that the variation of core losses with temperature at a given current is relatively small, as later discussed in another section of this chapter.

The new approach also fully exploits the fact that in PM and synchronous reluctance motors with distributed windings the rotor losses are typically low, such that their estimation may only be required in the outer loop, which includes the electromagnetic field analysis. It should be noted that in the proposed ultrafast technique depicted in Figure 2.12b there are two initial estimations for the temperature, one for the inner loop and another for the outer loop, respectively. In order to make sure that not only the copper losses, but also the other loss components, most notably the

core losses, are satisfactory estimated together with the temperature distribution, two separate error criteria $\epsilon_{w1}, \epsilon_{w2}$, are employed.

The procedure described has been implemented using MATLAB programming. The ActiveX technology was employed for coupling the electromagnetic computational engine that uses the Maxwell software by ANSYS [67], and the thermal and air-flow computational engine, which is represented the Motor-CAD software by Motor Design [58]. The algorithm and the combination of software ensures a minimum number of electromagnetic field simulations, which are the most time consuming in the current implementation, as they are performed using FEA.

2.5 Examples of analysis

CE-FEA example

This section is an example for the validation of the CE-FEA approach performed on aN IPM machine with 36-slot 6-pole. As shown in Figure 2.13, at least four magnetostatic solutions should be taken into consideration to ensure the accuracy of CE-FEA results. A further increase in the number of static solutions will not provide additional accuracy in the estimation of the average torque. In this case, the CE-FEA approach will utilize two sets of magnetostatic solutions, with five and seven time steps, respectively.

Two sets of CE-FEA results with five and seven magnetostatic solutions were

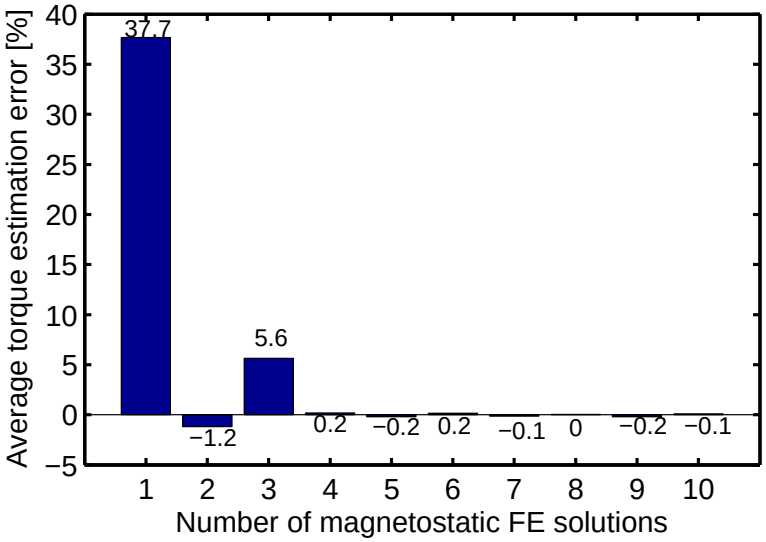

Figure 2.13: Error of the average torque computed with CE-FEA with respect to a detailed TS-FEA simulation.

validated separately by the results of transient time-stepping FEA (TS-FEA) in Table 2.2. The results from seven magnetostatic solutions are more accurate than the results from five magnetostatic solutions. Also the 6th harmonic of the electromagnetic torque from five magnetostatic solutions is significant. For these reasons, following validations are based on the simulation results with seven magnetostatic solutions.

Table 2.2: Comparison of average torque, torque harmonic, torque ripple and stator core losses for CE-FEA with five and seven solutions.

	TS-FEA (180 solutions)	CEFEA (5 solutions)	Difference [%]	CEFEA (7 solutions)	Difference [%]
Simulation Time [s]	323.00	75.00	0.77	78.00	0.76
Average Torque [Nm]	47.77	47.59	0.00	47.60	0.00
Tq. 6th Harmonic [Nm]	0.85	3.55	3.18	0.78	0.08
Tq. 12th Harmonic [Nm]	11.40	10.59	0.07	11.48	0.01
Torque Ripple [%]	56.47	53.82	0.05	54.35	0.04
Stator Core Losses [W]	573.00	645.00	0.13	645.00	0.13
Total Core Losses [W]	698.00	645.00	0.08	645.00	0.08

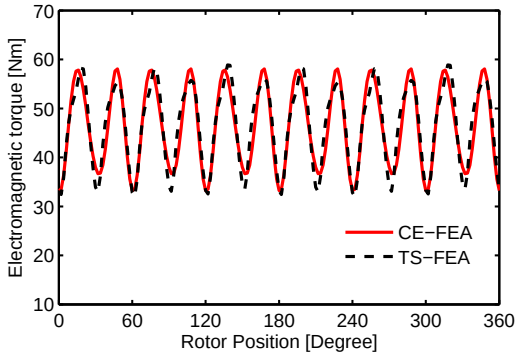

Figure 2.14: Electromagnetic torque with rated current supply of a PM machine with 36 slots and 6 poles (torque angle=120°).

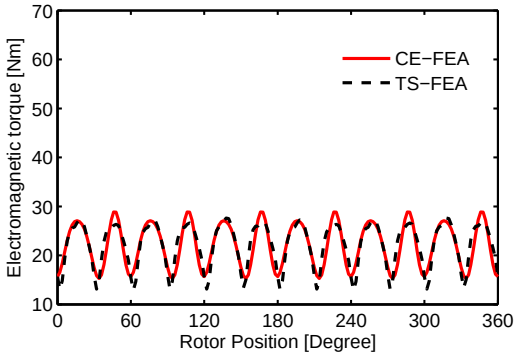

Figure 2.15: Electromagnetic torque with half rated current supply of a PM machine with 36 slots and 6 poles (torque angle=120°).

Shown in Figure 2.14 and Figure 2.15 are the comparison of electromagnetic torques calculated by CE-FEA and TS-FEA, respectively.

The symmetric property of the magnetic circuit of electric machines results in the symmetry flux density distribution in stator core. As showing in Figure 2.16, Y1 and Y2 present two points in the yoke which could present rest flux density distribution in back iron/yoke. The same approach is used to obtain the flux density distribution in the middle of a stator tooth. Figure 2.19 to Figure 2.22 are the waveforms of flux density distributions in the stator core according to Figure 2.16.

Table 2.3 through Table 2.7 provide the values of the average electromagnetic torque, torque harmonics, torque ripple, harmonics and total harmonic distortion of induced voltage as well as harmonics of the flux density in the stator core for different torque angles, respectively.

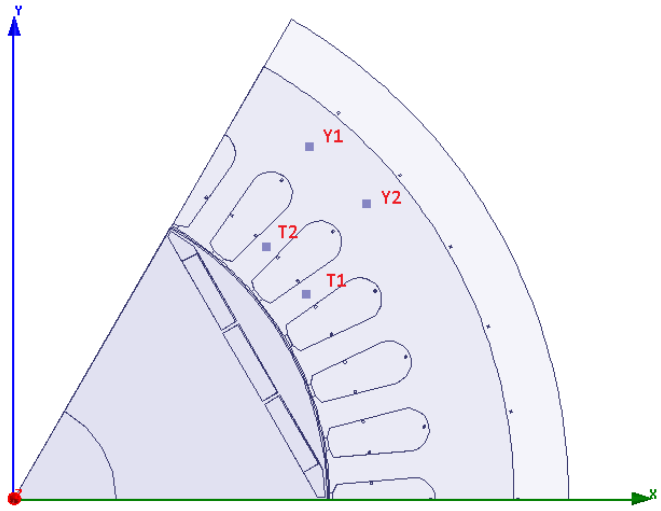

Figure 2.16: Magnetic circuit symmetry and sampling points of flux densities in the stator core.

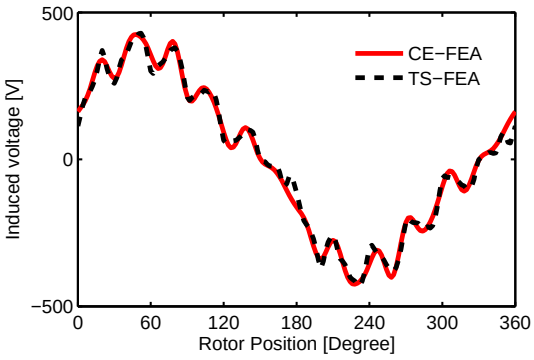

Figure 2.17: Induced voltage profiles of a PM machine with 36 slots and 6 poles (torque angle=120°).

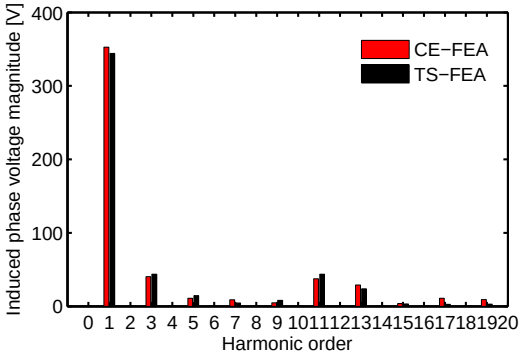

Figure 2.18: Fourier spectrum of the induced voltage calculated from Figure 2.17 (torque angle=120°).

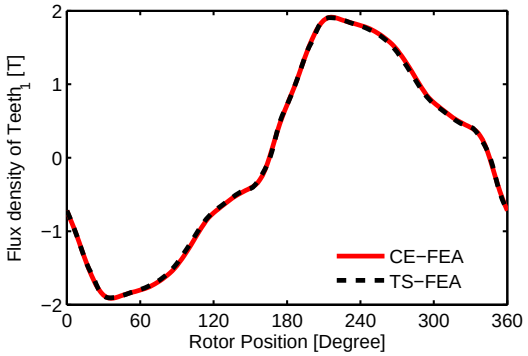

Figure 2.19: Flux density of teeth group 1 of a PM machine with 36 slots and 6 poles (torque angle=120°).

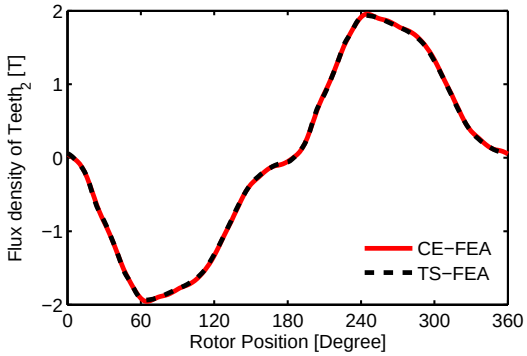

Figure 2.20: Flux density of teeth group 2 of a PM machine with 36 slots and 6 poles (torque angle=120°).

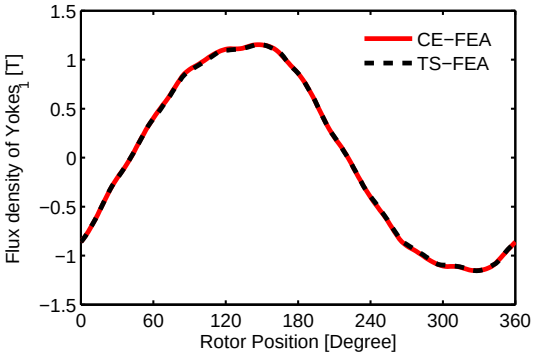

Figure 2.21: Flux density of yokes group 1 of a PM machine with 36 slots and 6 poles (torque angle=120°).

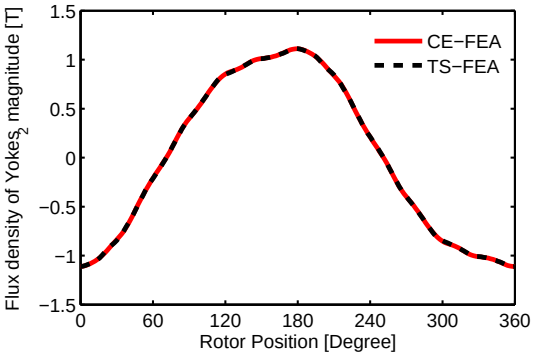

Figure 2.22: Flux density of yokes group 2 of a PM machine with 36 slots and 6 poles (torque angle=120°).

Table 2.3: Performance parameters for various torque angle estimated with CE-FEA employing seven magnetostatic FE solutions and detailed TE-FEA (choose 110°torque angle as reference).

TS-FEA (180 solutions)										
	Electromagnetic Torque				Induced Phase Voltage					
TqAng	AvgTq [pu]	6th [pu]	12th [pu]	Ripple [%]	Fund. [pu]	5th [pu]	7th [pu]	11th [pu]	13th [pu]	THD [%]
90°	0.94	0.02	0.22	53.83	1.07	0.03	0.02	0.08	0.07	10.79
100°	0.99	0.02	0.23	55.30	1.04	0.03	0.02	0.10	0.05	12.38
110°	**1.00**	**0.02**	**0.24**	**56.60**	**1.00**	**0.04**	**0.02**	**0.11**	**0.05**	**15.18**
120°	0.97	0.02	0.24	57.85	0.95	0.04	0.01	0.12	0.07	19.92
130°	0.91	0.02	0.22	59.40	0.90	0.04	0.01	0.13	0.08	25.66
140°	0.81	0.02	0.20	61.67	0.84	0.03	0.00	0.15	0.08	32.56
150°	0.66	0.03	0.17	66.63	0.78	0.02	0.01	0.18	0.10	42.28
160°	0.47	0.03	0.12	71.68	0.72	0.02	0.02	0.23	0.15	55.71
170°	0.24	0.04	0.07	110.72	0.68	0.03	0.03	0.25	0.18	66.39
180°	0.00	0.04	0.04	0.00	0.66	0.04	0.01	0.23	0.15	66.91
CE-FEA (7 solutions)										
90°	0.94	0.01	0.22	54.89	1.10	0.01	0.01	0.07	0.07	9.95
100°	0.98	0.01	0.23	54.90	1.07	0.02	0.02	0.08	0.06	10.81
110°	0.99	0.02	0.24	54.71	1.02	0.02	0.03	0.09	0.06	13.18
120°	0.96	0.02	0.24	54.37	0.98	0.03	0.03	0.10	0.08	18.12
130°	0.90	0.03	0.23	55.75	0.92	0.03	0.02	0.11	0.10	24.05
140°	0.79	0.04	0.20	57.06	0.86	0.03	0.01	0.14	0.10	31.12
150°	0.65	0.04	0.17	59.12	0.80	0.02	0.01	0.17	0.12	40.82
160°	0.46	0.05	0.12	60.99	0.73	0.01	0.03	0.23	0.17	55.30
170°	0.23	0.05	0.06	96.97	0.68	0.02	0.03	0.24	0.20	65.97
180°	0.00	0.05	0.04	0.00	0.66	0.03	0.01	0.22	0.17	66.88

Table 2.4: Flux density in tooth 1 for various torque angle estimated with CE-FEA employing seven magnetostatic FE solutions and detailed TS-FEA (choose 110° torque angle as reference).

Flux density in tooth_1						
TS-FEA (180 solutions)						
Torque Angle [elec. deg.]	Fund. [pu]	5th [pu]	7th [pu]	11th [pu]	13th [pu]	THD [%]
90	1.058	0.061	0.001	0.009	0.006	9.48
100	1.031	0.064	0.003	0.011	0.006	11.40
110	**1.000**	**0.066**	**0.005**	**0.012**	**0.005**	**14.26**
120	0.963	0.065	0.005	0.013	0.006	18.22
130	0.921	0.063	0.003	0.014	0.007	23.26
140	0.879	0.058	0.006	0.014	0.008	29.09
150	0.837	0.053	0.018	0.017	0.008	35.58
160	0.797	0.045	0.034	0.024	0.011	42.25
170	0.769	0.039	0.048	0.024	0.014	48.01
180	0.760	0.040	0.054	0.020	0.015	50.16
CE-FEA (7 solutions)						
Torque Angle [elec. deg.]	Fund. [pu]	5th [pu]	7th [pu]	11th [pu]	13th [pu]	THD [%]
90	1.064	0.062	0.002	0.008	0.007	9.39
100	1.028	0.065	0.001	0.010	0.007	11.20
110	0.998	0.068	0.004	0.012	0.006	13.90
120	0.962	0.067	0.005	0.014	0.006	17.65
130	0.922	0.065	0.003	0.015	0.007	22.53
140	0.879	0.061	0.005	0.015	0.009	28.33
150	0.837	0.054	0.016	0.018	0.009	34.75
160	0.797	0.046	0.032	0.024	0.011	41.36
170	0.768	0.039	0.046	0.026	0.014	47.27
180	0.757	0.039	0.053	0.022	0.015	49.70

Table 2.5: Flux density in tooth 2 for various torque angle estimated with CE-FEA employing seven magnetostatic FE solutions and detailed TS-FEA (choose 110° torque angle as reference).

Flux density in tooth_2						
TS-FEA (180 solutions)						
Torque Angle [elec. deg.]	Fund. [pu]	5th [pu]	7th [pu]	11th [pu]	13th [pu]	THD [%]
90	1.080	0.063	0.005	0.005	0.005	6.83
100	1.044	0.068	0.008	0.006	0.003	9.17
110	**1.000**	**0.072**	**0.009**	**0.007**	**0.003**	**12.82**
120	0.945	0.073	0.007	0.008	0.006	17.99
130	0.882	0.070	0.003	0.010	0.007	24.76
140	0.811	0.063	0.006	0.014	0.006	33.19
150	0.733	0.054	0.018	0.017	0.008	43.46
160	0.654	0.045	0.033	0.020	0.014	55.41
170	0.589	0.044	0.046	0.022	0.014	67.61
180	0.564	0.048	0.050	0.022	0.010	73.30
CE-FEA (7 solutions)						
Torque Angle [elec. deg.]	Fund. [pu]	5th [pu]	7th [pu]	11th [pu]	13th [pu]	THD [%]
90	1.083	0.062	0.004	0.006	0.003	6.74
100	1.047	0.068	0.008	0.007	0.001	9.09
110	1.004	0.072	0.009	0.007	0.002	12.72
120	0.950	0.073	0.007	0.008	0.005	17.84
130	0.887	0.070	0.004	0.010	0.006	24.56
140	0.815	0.063	0.005	0.013	0.005	32.99
150	0.739	0.054	0.016	0.016	0.007	43.21
160	0.660	0.044	0.032	0.020	0.013	55.13
170	0.594	0.042	0.047	0.021	0.014	67.28
180	0.569	0.046	0.052	0.020	0.009	73.22

Table 2.6: Flux density in yoke 1 for various torque angle estimated with CE-FEA employing seven magnetostatic FE solutions and detailed TS-FEA (choose 110° torque angle as reference).

Flux density in yoke_1						
TS-FEA (180 solutions)						
Torque Angle [elec. deg.]	Fund. [pu]	5th [pu]	7th [pu]	11th [pu]	13th [pu]	THD [%]
90	1.066	0.016	0.002	0.007	0.005	2.59
100	1.036	0.018	0.002	0.009	0.004	2.93
110	**1.000**	**0.019**	**0.002**	**0.010**	**0.004**	**3.79**
120	0.955	0.019	0.001	0.011	0.005	5.27
130	0.904	0.019	0.001	0.012	0.007	7.33
140	0.847	0.017	0.002	0.013	0.007	9.91
150	0.786	0.013	0.003	0.016	0.007	13.00
160	0.726	0.009	0.006	0.021	0.012	16.53
170	0.674	0.008	0.009	0.024	0.013	19.91
180	0.648	0.013	0.014	0.021	0.012	21.62
CE-FEA (7 solutions)						
Torque Angle [elec. deg.]	Fund. [pu]	5th [pu]	7th [pu]	11th [pu]	13th [pu]	THD [%]
90	1.072	0.016	0.002	0.007	0.005	2.44
100	1.042	0.018	0.003	0.009	0.004	2.78
110	1.006	0.019	0.002	0.010	0.003	3.63
120	0.961	0.020	0.001	0.011	0.004	5.11
130	0.908	0.019	0.001	0.012	0.006	7.21
140	0.849	0.018	0.001	0.014	0.007	9.86
150	0.787	0.014	0.002	0.017	0.007	13.03
160	0.724	0.009	0.005	0.021	0.011	16.68
170	0.670	0.007	0.009	0.023	0.014	20.24
180	0.642	0.011	0.014	0.020	0.012	22.15

Table 2.7: Flux density in yoke 2 for various torque angle estimated with CE-FEA employing seven magnetostatic FE solutions and detailed TS-FEA (choose 110° torque angle as reference).

Flux density in yoke_2						
TS-FEA (180 solutions)						
Torque Angle [elec. deg.]	Fund. [pu]	5th [pu]	7th [pu]	11th [pu]	13th [pu]	THD [%]
90	1.079	0.017	0.004	0.007	0.005	2.76
100	1.043	0.019	0.003	0.009	0.004	3.82
110	**1.000**	**0.020**	**0.003**	**0.010**	**0.004**	**5.29**
120	0.950	0.020	0.002	0.011	0.005	7.21
130	0.894	0.019	0.001	0.012	0.006	9.57
140	0.834	0.017	0.002	0.014	0.006	12.35
150	0.773	0.016	0.006	0.017	0.008	15.48
160	0.716	0.015	0.012	0.022	0.012	18.68
170	0.675	0.015	0.016	0.023	0.014	21.42
180	0.669	0.012	0.014	0.022	0.013	22.06
CE-FEA (7 solutions)						
Torque Angle [elec. deg.]	Fund. [pu]	5th [pu]	7th [pu]	11th [pu]	13th [pu]	THD [%]
90	1.080	0.017	0.004	0.007	0.005	2.82
100	1.043	0.019	0.004	0.008	0.004	3.87
110	1.000	0.020	0.003	0.010	0.004	5.32
120	0.950	0.020	0.002	0.011	0.005	7.24
130	0.893	0.019	0.001	0.012	0.006	9.61
140	0.833	0.018	0.002	0.013	0.007	12.41
150	0.772	0.016	0.006	0.017	0.008	15.58
160	0.714	0.015	0.011	0.022	0.012	18.90
170	0.673	0.015	0.015	0.023	0.014	21.67
180	0.667	0.013	0.014	0.021	0.012	22.36

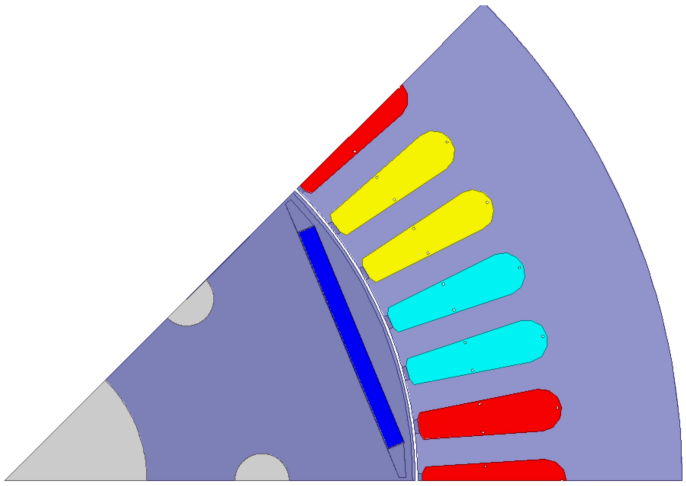

Figure 2.23: Cross-section and geometry of the flat bar-type PM machine with 48-slot 8-pole.

Coupled electromagnetic and thermal analysis

The coupled electromagnetic and thermal analysis was applied for the study of the IPM machine shown in Figure 2.23.

The example results shown in Figures 2.24 and 2.25 for the IPM motor of Figure 2.6a are based on only seven magnetostatic FEA solutions over a 1/6 of an electric cycle and yet demonstrate good agreement with the conventionally and substantially longer transient FEA (TS-FEA).

The temperature affects, among other things, the PM characteristics. An increase in temperature results in a PM B-H curve with lower remanence and a lower average output torque for the same current, as shown in Figure 2.26.

From an equivalent circuit point of view, the effect of the PM temperature, T_m,

on the PM (open-circuit) flux linkage can be quantified as:

$$\lambda_m(T_m) = \lambda_m(20^\circ\mathrm{C})\left[1 - k_r(T_m - 20^\circ\mathrm{C})\right], \tag{2.76}$$

where k_r is the temperature coefficient for the PM remanence. This temperature influence further reflects in the equations of the electromagnetic torque and of the torque angle, γ_M, corresponding to the Maximum Electromagnetic Torque per Ampere (METPA) condition as quantified in (2.77) and (2.78), respectively, where p is the number of poles, L_d and L_q are non-linear inductances, and I is the phase current. Similar equations, but without the PM flux linkage component and with a very strong non-linearity of inductances with respect to currents, are applicable for synchronous reluctance machines.

$$\begin{aligned} T_e &= \frac{3}{2}\frac{p}{2}\left[\lambda_m i_q + (L_d - L_q) i_d i_q\right] = \\ &= \frac{3}{2}\frac{p}{2}\left[\lambda_m(20^\circ\mathrm{C})\left[1 - k_r(T_m - 20^\circ\mathrm{C})\right] I\sin(\gamma) + (L_d - L_q) I^2 \sin(\gamma)\cos(\gamma)\right], \end{aligned} \tag{2.77}$$

$$\begin{aligned} \gamma_M &= \arccos\left(\frac{-\lambda_m I + \sqrt{\lambda_m^2 I^2 + 8(L_d - L_q)^2 I^4}}{4(L_d - L_q) I^2}\right) = \\ &= \arccos\left(\frac{-\lambda_m(20^\circ\mathrm{C})[1 - k_r(T_m - 20^\circ\mathrm{C})] I}{4(L_d - L_q) I^2}\right. \\ &\quad \left. + \frac{\sqrt{\lambda_m^2(20^\circ\mathrm{C})[1 - k_r(T_m - 20^\circ\mathrm{C})]^2 I^2 + 8(L_d - L_q)^2 I^4}}{4(L_d - L_q) I^2}\right) \end{aligned} \tag{2.78}$$

The computational method has been employed for the study of a range of integral horsepower totally enclosed fan cooled (TEFC) IPM motors. Due to space limitations, only examples from a 30hp 1,800rpm, 286 NEMA frame prototype unit with the generic configuration shown in Figure 2.3 are provided in the following.

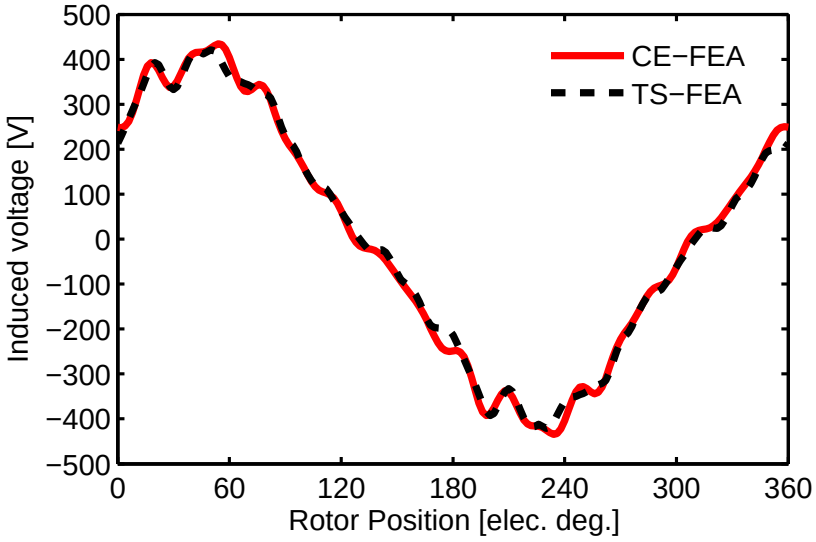

Figure 2.24: Induced voltage per phase for the rated load operation of an example 286 frame 30hp 1,800rpm IPM motor and a PM reference temperature of 60°C.

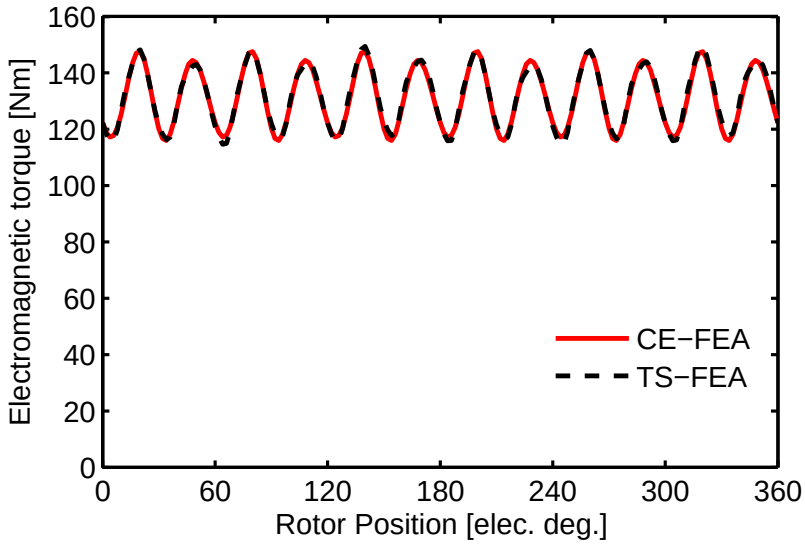

Figure 2.25: Torque for the IPM motor example operating at rated load and 60°C reference PM temperature.

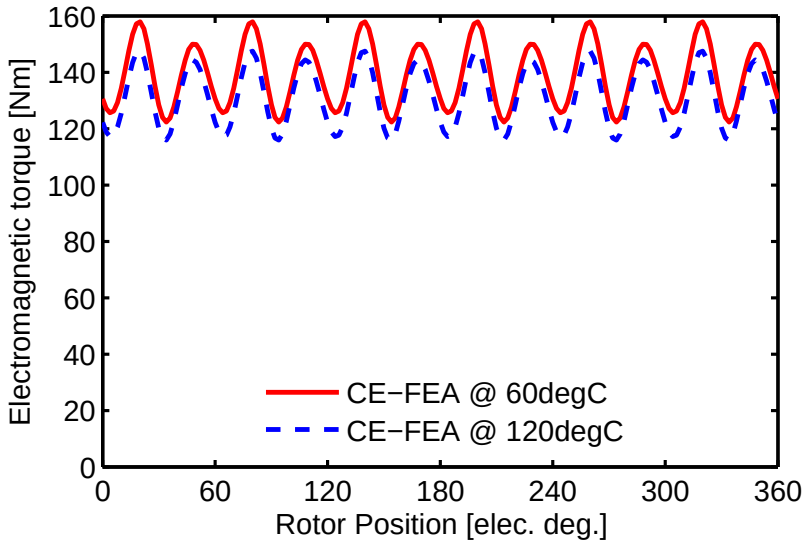

Figure 2.26: Variation of the electromagnetic torque with the PM temperature for rated current and speed for the rated IPM motor example.

Firstly, numerical studies were conducted using solely electromagnetic analysis, and specifying the phase current and the average temperature for the stator winding at the typical reference value of 75°C. As exemplified in Figure 2.27 for rated current, in between the minimum and the maximum temperature specified for the PM, the total core losses are reduced by only 14%. For reference, the electromagnetic torque in this case is also reduced, but only by 10%, while the optimal torque angle for MTPA remains approximately constant at 108deg. Overall, this study supports the proposed implementation in which the core losses are only updated in the outer loop that includes both the electromagnetic and the thermal calculations.

The stability and the convergence of the new multi-physics coupled procedure were verified by starting the iterative process with largely different initial estimates

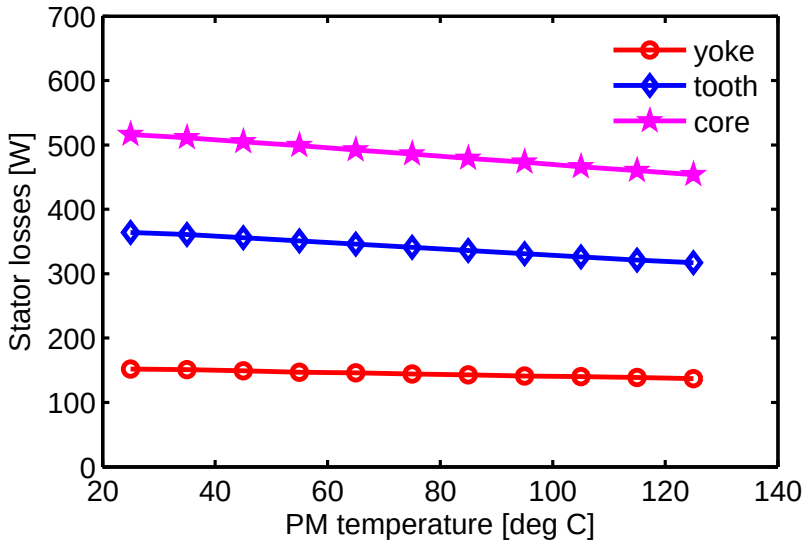

Figure 2.27: Stator core losses at rated current and constant 75°C winding reference temperature in the IPM example motor.

of the average temperature in the winding and the PM. A 5% convergence error was employed for all studies both for ϵ_{w1} and ϵ_{w2} identified in Figure 2.12b. As shown in Table 2.8, for constant current at its rated value, the convergence was quickly reached in only two outer loop electromagnetic and thermal iterations, each incorporating five or six ultrafast inner thermal loops.

Another computational study was performed for over-load with twice the rated current (Table 2.9). In this case, up to four outer loop electromagnetic and thermal iterations are required for convergence. All together, the results show that the computational effort is, of course, influenced by the initial estimation, which in the overload example was purposely selected substantially different from the final result.

It should be noted that the numerical model was validated through satisfactory

Table 2.8: Steady-state rated load simulations showing that convergence was reached in only two iterations. The results also compared satisfactorily with the measured average values for stator winding and PM temperature.

Winding Temperature [°C]			PM Temperature [°C]			Final Losses	
Initial T_w^o	1st iteration	2nd iteration	Initial T_{PM}^o	1st iteration	2nd iteration	Core losses [W]	Copper losses [W]
25.0	71.7	**68.3**	25.0	68.2	**65.5**	492.0	394.7
25.0	64.1	**68.6**	125.0	62.0	**65.7**	490.5	400.0
125.0	71.7	**68.3**	25.0	68.2	**65.5**	492.0	394.7
125.0	64.1	**68.6**	125.0	62.0	**65.7**	490.6	400.0
65.0	**68.9**	N/A	60.0	**65.9**	N/A	495.3	402.3

Table 2.9: Steady-state simulations for overload at twice rated current and 1,800rpm.

Winding	Initial T_w^o	[°C]	25.0	25.0	125.0	125.0	65.0	160.0
	1st iteration	[°C]	137.8	169.8	137.8	169.8	149.3	**163.5**
Temperature	2nd iteration	[°C]	171.3	160.9	171.3	160.9	167.3	N/A
	3rd iteration	[°C]	160.1	**163.7**	160.1	**163.7**	161.5	N/A
	4th iteration	[°C]	**163.6**	N/A	**163.6**	N/A	**163.3**	N/A
PM	Initial iteration	[°C]	25.0	125.0	25.0	125.0	60.0	140.0
	1st iteration	[°C]	120.9	146.2	120.9	146.2	130.0	**141.2**
Temperature	2nd iteration	[°C]	147.3	139.2	147.3	139.2	144.2	N/A
	3rd iteration	[°C]	138.5	**141.4**	138.5	**141.4**	139.6	N/A
	4th iteration	[°C]	**141.3**	N/A	**141.3**	N/A	**141.0**	N/A
Final	Core losses	[W]	658.8	663.2	658.8	663.4	660.0	664.1
	Copper losses	[W]	2097.8	2096.1	2097.8	2096.2	2090.8	2090.5

Table 2.10: Experimental and simulation results for 1,800rpm rated operation with and without fan.

		TEFC		TE - no fan	
		Experiment	Simulation	Experiment	Simulation
Total losses	[W]	1065	1013	1081	1150
R LL hot	[ohm]	0.215	0.208	0.247	0.255
Current	[A]	35.2	35.5	35.8	35.5
Wcu	[W]	399	402	473	485
Wwf	[W]	116	116	90	90
WFe	[W]	550	495	518	575
WFe back iron	[W]	N/A	147	N/A	136
WFe Tooth	[W]	N/A	348	N/A	314
T rise TC	[°C]	47.6	45.9	97.3	112.5
Temp Wdg TC	[°C]	70.6	68.9	120.3	135.5
Temp PM	[°C]	67.1	65.9	117.4	128.9

comparison with the measurements performed on a dyne equipped with an automatic control and data acquisition system (Table 2.10 and Figure 2.28). The reported averages for the winding and the PM temperatures have been determined through off line resistance and back-emf measurements immediately following the steady-state load test. The algorithm was also employed for the heat-run test and simulation of the same IPM motor, but with the fan physically removed and the air-flow set to zero in the simulation. In line with engineering expectations, the temperature rise in this case was significantly higher, the results from Table 2.10 illustrating the benefits of forced ventilation, ultimately resulting in lower losses and higher efficiency.

The model was also satisfactorily validated on the slow-transient heat run test with a constant rated current for the same IPM motor. Multiple thermocouples have been placed in various parts of the motor and example results for the frame, winding

Figure 2.28: Experimental system with automatic dyne controls and data acquisition system.

and core, are shown in Figure 2.29.

Extensive simulations were performed with the coupled electromagnetic and thermal model at various speeds and loads, i.e. different current supply. The results from Figure 2.30, which illustrate that the variation of core losses with load is relatively reduced, are a typical finding that supports the proposal for not updating these losses as part of the inner loop of the newly developed iterative approach. In an alternative approach, a simplified model for core losses could also be implemented in connection with the inner loop, noticing that these losses are dominated by the open-circuit field due to the PMs, hence the relatively limited variation with load.

The results from Figure 2.31 show that in a TEFC construction, as well as in

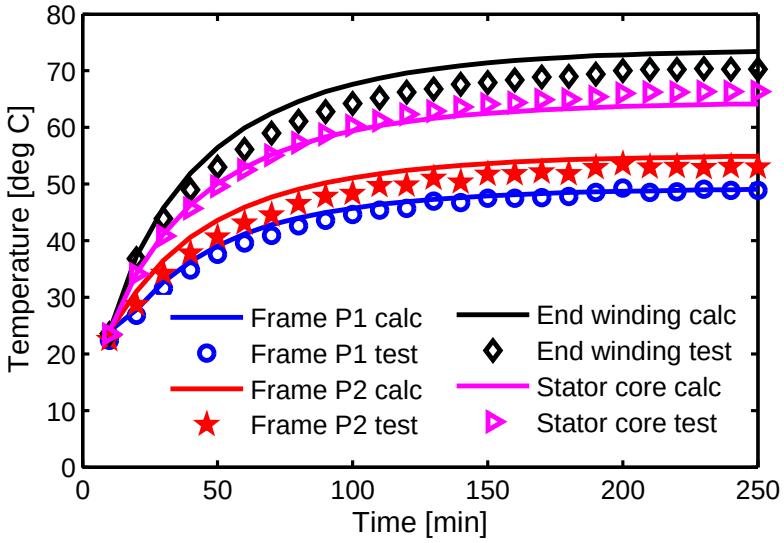

Figure 2.29: Heat run test and simulation at constant rated load and speed.

a design which is forced cooled on the outer surface of the stator, despite typical misconception, the temperature in the PM is comparable with that of the winding. The entire equivalent thermal and air-flow network contributes, of course, to this outcome, but it is interesting to note that the relatively large air-gap typical to PM machine designs ensures basically a thermal insulation of the rotor with respect to the stator.

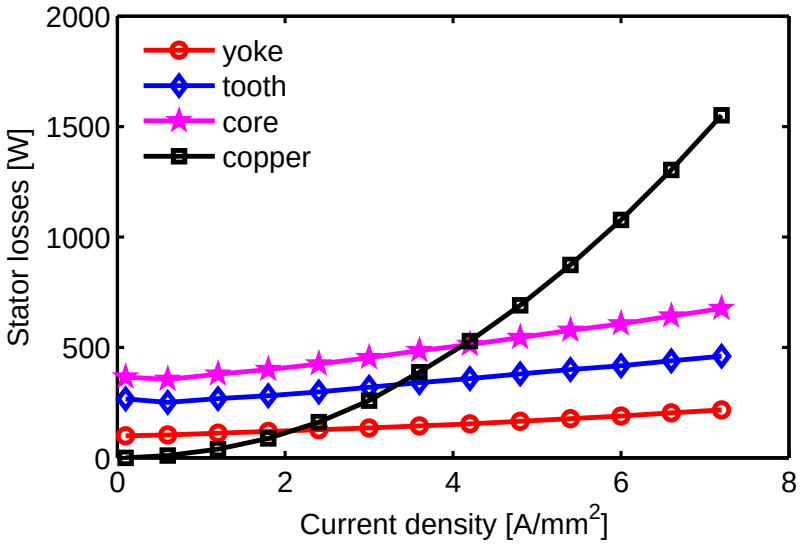

Figure 2.30: Variation of stator losses with load at constant rated speed.

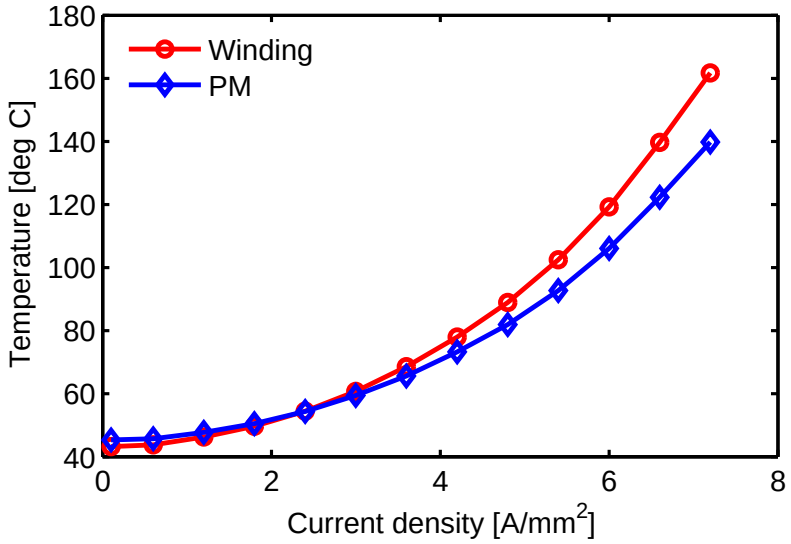

Figure 2.31: Average temperature variation with load at constant rated speed.

CHAPTER 3

Parameterization and Optimization

3.1 General concepts for ratio parameterized FEA models

Thousands of the DE designs are typically evaluated by the CE-FEA method during an optimization process. In order to obtain a robust parametric model and avoid the geometric overlapping in the automated design optimization procedure, some of the geometric parameters were defined by ratio expressions. For better illustrating the concept, a ratio parameterized model of the slot for the 36-slot 6-pole IPM machine and 36-slot 4-pole SyncRel machine is shown in Figure 3.1. For instance, the stator inner radius, R_{si}, tooth width, T_W, and the slot opening width, w_{SO}, were defined using the ratio expressions of $k_{si},\ k_{wt}$ *and* k_{tip}. These parametric ratios, along with several real geometry variables, such as the airgap height h_g and the width of the back iron in the stator Y_T, are defined as the input for the DE design optimization in forms of matrix $[k_{si}, k_{wt}, k_{tip}, h_g, Y_T]$ with the corresponding variable ranges provided in Table 3.1. For the stator geometry shown in Figure 3.1, the input stator geometric parameters are given as follows:

- Independent stator geometric parameters:

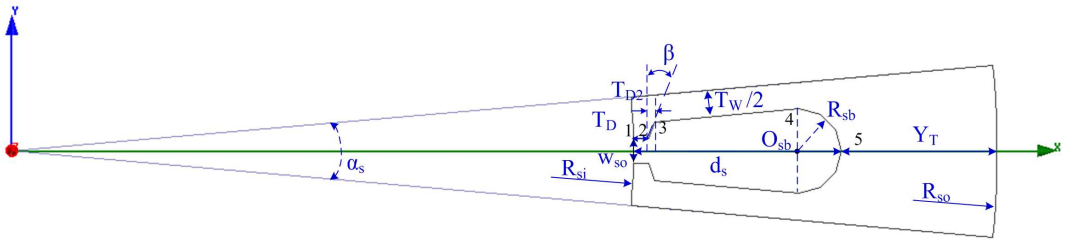

Figure 3.1: Cross-section and geometry parameters of stator slot.

1. N_s : number of stator slots
2. R_{so} : stator outer radius
3. k_{si}: split ratio between the stator inner radius and outer radius, $k_{si} = R_{si}/R_{so}$
4. h_g: airgap height
5. k_{wt}: tooth width ratio, $k_{wt} = \alpha_{wt}/\alpha_s$
6. Y_T: width of back iron in the stator
7. k_{tip}: tooth tip angle ratio, $k_{tip} = \alpha_{tip}/(\alpha_s - \alpha_{wt})$
8. T_D: width of wedges
9. T_{D2}: tooth tip length

- Auxiliary calculated geometric variables and expressions can be deduced based on the independent geometric variables, which are listed as follows:

1. α_s: slot pitch, mechanical degree, $\alpha_s = 360/N_s$
2. R_{si}: stator inner radius, $R_{si} = k_{si}R_{so}$

3. T_W: tooth width, $T_W = 2R_{si}\sin(k_{wt}\alpha_s/2)$

4. R_{slot}: stator slot bottom radius, $R_{slot} = R_{so} - Y_T$

5. w_{so}: slot opening width, $w_{so} = Y_T/2/\sin(\alpha_s/2)$

6. R_{sb}: slot bottom radius,

   $R_{sb} = [R_{slot}\tan(\alpha_s/2) - T_W/2/\cos(alpha_s/2)]/[1+\tan(\alpha_s/2)]$

$$
\begin{cases} x_{p1} = \sqrt{R_{si} - (w_{so}/2)^2} \\ y_{p1} = w_{so}/2 \end{cases}
\begin{cases} x_{p2} = x_{p1} + T_D \\ y_{p2} = y_{p1} \end{cases}
\begin{cases} x_{p3} = (R_{si} + T_D + T_{D2})\cos[(1 - k_{wt}\alpha_s/2)] \\ y_{p3} = (R_{si} + T_D + T_{D2})\sin[(1 - k_{wt}\alpha_s/2)] \end{cases}
\begin{cases} x_{p4} = R_{slot} - R_{sb} \\ y_{p4} = R_{sb} \end{cases}
\begin{cases} x_{p5} = R_{slot} \\ y_{p5} = 0 \end{cases}
\tag{3.1}
$$

Table 3.1: Specification of independent geometric parameters for the parametric model depicted in Figures 3.1.

Variable	Unit	Minimum value	Maximum value
Y_T	[mm]	12.7	19.05
h_g	[mm]	0.7	1.3
k_{si}		0.55	0.72
k_{wt}		0.35	0.55
k_{tip}		0.3	0.8

3.2 Mathematical formulation of the optimization problem

Suppose that there are n performance indices, such as the efficiency, material cost and torque ripple, are taken into consideration in the optimal design procedure. These performance indices can be defined as objectives to be minimized or maximized:

$$f_1(X), f_2(X), \cdots, f_n(X) \ , \tag{3.2}$$

where $f_n(X)$ is the mathematical function of the n^{th} physical performance index which is dependent on m independent variables:

$$X = [x_1, x_2, \cdots, x_m] \ , \tag{3.3}$$

such as the ratios described in 3.1, airgap, stator diameter, etc.

For the optimization problems, which are subject to constraints:

$$G = [g_1(X), g_2(X), \cdots, g_l(X), h_{l+1}(X), h_{l+2}(X), \cdots, h_{l+j}(X)] \ , \tag{3.4}$$

where $g_l(X) \leq 0$ is the l^{th} inequality constraint and $h_{l+j}(X) = 0$ is the j^{th} equality constraint, the penalty function method is applied to solve the constrained optimization problem. A substantial amount of constraint violation can be employed to punish an infeasible solution so that it is less likely to survive into the next generation than a feasible solution.

3.3 Differential evolution algorithm

Differential evolution (DE), which was proposed by Storn and Price in 1995 [68], is highly-recommended method for multi-objective design optimization of electric machines, such as IPM, and SyncRel machines. The algorithm includes processes of initialization, mutation, crossover, and selection, which are explained as follows:

- Initialization

  The initial population of DE is randomly generated through a random process within the upper bounds (X_U) and lower limits (X_L). The initial value of the j^{th} design variable of the i^{th} vector in the initial population can be expressed as [52]:

$$x_{j,i,1} = rand_j(0,1) \cdot (x_{j,U} - x_{j,L}) + x_{j,L} \ , \tag{3.5}$$

  where $0 \leq rand_j(0,1) < 1$, and j indicates that a new random value is generated for each design variable.

- Mutation Operation

  The mutant vector, which is the combination of three different, randomly chosen vectors by the differential mutation process, is defined by

$$\vec{v}_{i,g} = \vec{x}_{r1,g} + F \cdot (\vec{x}_{r2,g} - \vec{x}_{r3,g}) \ , \tag{3.6}$$

where the scale factor, $F \in (0, 1+)$, is a positive value without upper limit, the subscripts $r1$, $r2$, and $r3$ represent mutually different integers that are different from the the target index i and that are randomly generated over [1, Np]. The population of DE consists of N_P-dimensional vectors:

$$\vec{x}_{i,g} = (\vec{x}_{i,1,g}, \vec{x}_{i,2,g}, \cdots, \vec{x}_{i,n,g}),\ i = 1, 2, \cdots, N_P \tag{3.7}$$

where g denotes the generation number.

- Crossover

The crossover procedure generates a new trail generation through mixing the target vector $\vec{x}_{i,g}$ with the mutant vector $\vec{v}_{i,g}$. The trial vector can be formulated as follows [69]:

$$u_{i,g} = (u_{j,i,g}),\ \text{where}\ u_{j,i,g} = \begin{cases} v_{j,i,g},\ \text{if}\ rand_j(0,1) \leq C_r\ \text{or}\ j = j_{rand} \\ x_{j,i,g},\ \text{otherwise} \end{cases} \tag{3.8}$$

where $i = 1, 2, ..., N_p, j = 1, 2, ..., n$, and the crossover control parameter, $C_r \in [0, 1]$, is a user-defined value that controls the fraction of variables' values that are copied from the mutant process. In the above equation, $rand_j(0, 1)$ is the jth evaluation of a uniform random number generator and index j_{rand} is a randomly selected integer within the range [1, n].

- Selection

In the selection step, the trial vector $\vec{u}_{i,g}$ is compared against the target vector in the current generation, $\vec{x}_{i,g}$, to generate a better target vector for the next

generation:

$$x_{i,g+1} = \begin{cases} u_{i,g}, \text{ if } f(\vec{u}_{i,g}) \leq f(\vec{x}_{i,g})) \\ x_{i,g}, \text{ otherwise} \end{cases} \tag{3.9}$$

Once a new generation is obtained and analyzed by the CE-FEA approach, the process of mutation, crossover and selection is repeated until the stopping criteria are satisfied.

The above procedures are repeated until the maximum number of function evaluations is satisfied.

In our research work, a newly proposed method by Wang and Cai [70] , named Combing Multi-objective Optimization with Differential Evolution (CMODE), is utilized to solve constrained optimization problems. In CMODE method, the mutation and crossover operations of the DE, which serves as the search engine, are applied to generate the offspring population. However, the selection operation is not utilized.

The main CMODE process includes the procedures of initialization, mutation, and crossover, which is as shown in Figure 3.2. In the initialization step, an initial population of N_P individuals, $P_{(g)} = \{\vec{x}_1, \vec{x}_2, ..., \vec{x}_{N_p}\}$, where g denotes the generation number and $g = 1$ for the initial population, is randomly generated through a random process within the decision space$[X_{U_i}\ X_{L_i}]$, $1 \leq i \leq n$.

In the second step, set Q, which has λ individuals, is randomly selected to be deleted from P_g. For each individual in set Q, an offspring is created by using the mutation and crossover procedures. Subsequently, λ offspring (set C) are generated

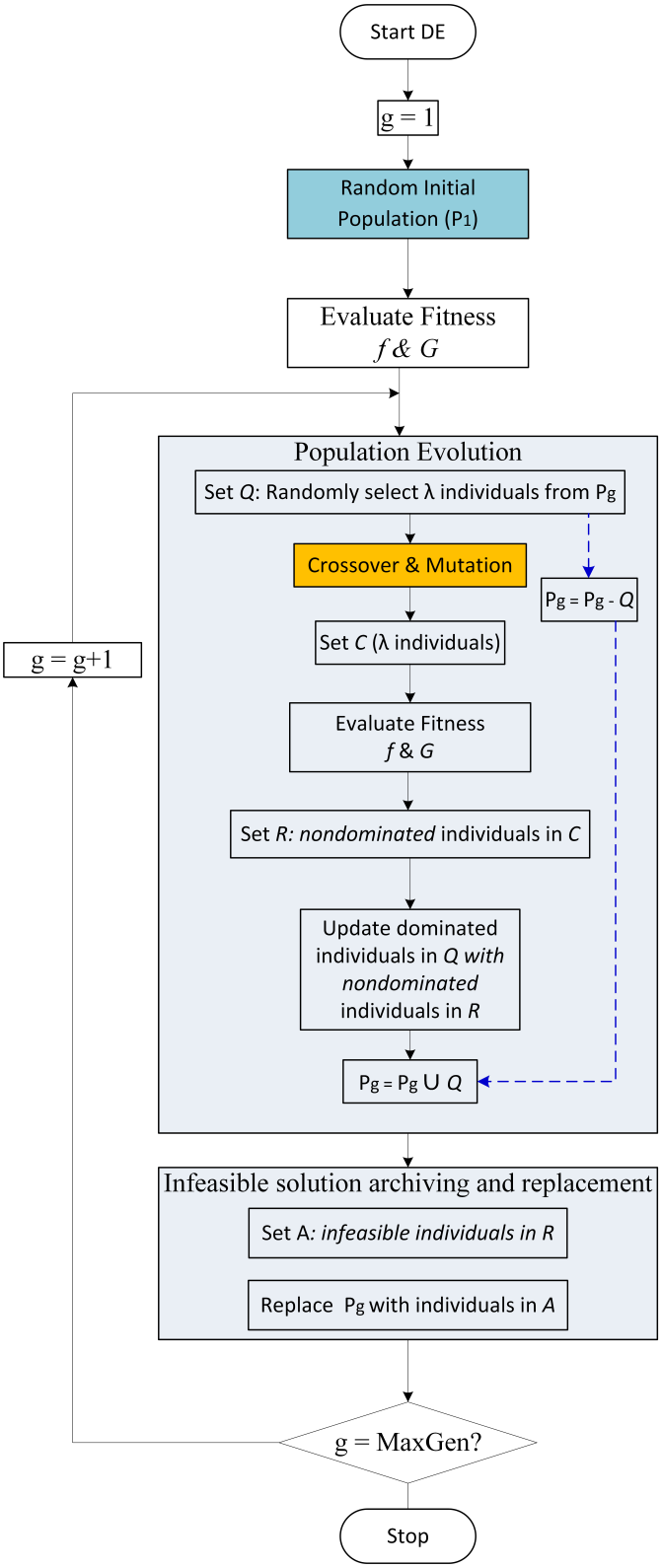

Figure 3.2: Framework of CMODE for DE optimization.

from Q, in which are the nondominated individuals (set R) from set C. Assuming that there are m nondominated individuals, which are defined as $\vec{x}_1, .., \vec{x}_m$, and n individuals in Q are dominated by $\vec{x}_1$, then one of the dominated individuals chosen at random will be replaced by $\vec{x}_1$. Thereafter, the remaining nondominated individuals of set R will continue the same process for the updated set Q in turn, then update P_g by combining the updated Q and original P_g.

The third step is the infeasible solutions archiving and replacement. If set R does not contain any feasible solutions, then the infeasible individual with the lowest degree of constraint violation in R, $\vec{x}$', is stored into archive A. The infeasible individuals in A are used to replace the same number of individuals in P_g for every k generation.

3.4 Pareto fronts and best design selection

Pareto dominance, which is used to compare and rank decision vectors, is an important concept of the multi-objective optimization. In multi-objective optimization problem, each objective can be either a minimization or a maximization of an output. A solution is defined as Pareto optimal if and only if there is no other solution that dominates it. The set of all Pareto optimal solutions is called the Pareto optimal set. Pareto front, the illustration of the Pareto optimal set in the objective space, is as shown in Figure 3.3. In general, the best design with compromise solution can be selected on the Pareto front, on which the improvement in one objective can only be

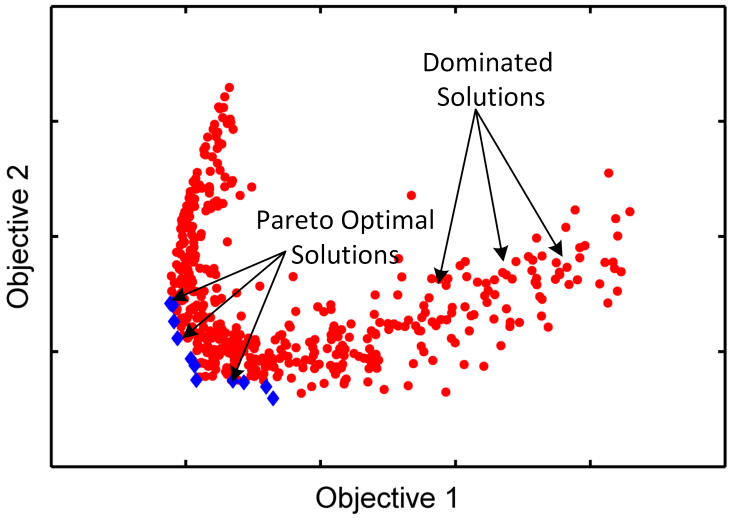

Figure 3.3: Illustration of Pareto front for a biobjective optimization problem.

achieved through a deterioration in another objectives.

Take the minimization problem as an example, the optimization is aimed at minimizing the Objective 1 and 2 as shown in Figure 3.3. For the application of the muti-objective optimization with multiple constraints for the electric machine design, where conflicts may exist between objectives, the decision-making based on a Pareto-front are more complicated. The comparison and study on the optimal designs selection from the Pareto front, including an engineering decision process and a tradeoff study, will be introduced in the case study section.

3.5 Implementation of a DE algorithm in MATLAB combination with CE-FEA and coupled analysis

Provided in Figure 3.4 is the work flow of the design optimizaiton procedure considering the electromagnetic field and thermal analysis In general, this work flow are the combination of the three parts: optimization algorithm, CE-FEA and optional files for thermal analysis and Time-stepping Transient analysis. A brief description of these MATLAB files is provided as follows:

- **Main_Optimization.m**: Main entrance for the multi-objective optimization, including initialization of the upper and lower bounds for the independent variables, number of generations and individuals in each generation, invoking of other two functions: DEoperations_Fn.m and Models_Fn.m

- **DEoperations_Fn.m**: This script code is used to generate set C which includes λ offspring mentioned in Section 3.3.

- **Models_Fn.m**: This file is used to update the designs with the nondominated individuals in set R.

- **Main_EmgThm.m**: This is the main routine of the coupling between the electromagnetic and thermal analysis.

- **General_Data.m**: Geometric parameters and variables which will be stored in MainData.mat are defined in this file. Also flags which determine whether to implement certain optional functions, such as result comparison and thermal analysis, will be stored in AnalysisType.mat. Extract ANSYS-Maxwell input data from MainData.mat and generate DesignProperties.mat.

- **StatorSlotArea_Fn.m**: Invoked by General_ Data.m, to calculate the stator slot area.

- **Cell2csv_Fn.m**: Convert the independent variables in the matrix to a csv file so that the inputs could imported to optimetrics in Maxwell 2D which is used for the Distributed Solve (parallel processing).

- **Extract_results_Fn.m**: This function is to extract results for each candidate design from the results matrix which is directly read from the CSV file exported from ANSYS Maxwell.

- **CEFEA_Fn.m**: This file is the main function for the implementation of the CE-FEA method, in which the performances of torque, induced voltages, flux linkage and losses can be evaluated.

- **RunANSYS_Fn.m**: This file will run ANSYS Maxwell-2D as the electromagnetic computational engine. Torque, flux linkage and back EMF will be stored in ANSYSOutput.mat. And flux linkages in the stator teeth and yoke will

be stored in Fluxlinkage.mat. Inductance will be stored in ANSYSLs.mat if the function of induction and torque angle calculation is enabled. Under this condition, inductance matrix calculation is enabled in ANSYS Maxwell.

- **IndTqAng_Fn.m**: This function is to calculate the inductance and torque angle based on the method 1 mentioned in 2.2.2.

- **Fluxlinkage_PM_Fn.m**: This file is used to calculate permanent magnet fluxlinkage at 90° torque angle. This is the first step of d-q inductance and torque calculation utilizing the method 2 mentioned in section 2.2.2.

- **Inductance_120deg_Fn.m**: Second step of torque caluculation utilizing the method 2 mentioned in section 2.2.2.

- **RunANSYS_Trans_Fn.m**: This file will run ANSYS Maxwell as the electromagnetic computational engine in which the model will be simulated over full electrical cycle. Torque, fluxlinkage and back EMF will be stored in ANSYSOutput_Trans.mat and flux linkages in the stator teeth and yoke will be stored in Fluxlinkage_Trans.mat. Flux density in the teeth and yokes calculated by the field calculator in the ANSYS Maxwell software will be exported to ANSYSOutput_B_field.mat if AnalysisType.Field =1.

- **Trans_Fn.m**: This function is to extract torque, induced voltages, flux-linkage and flux density from the simulation results of transient FEA.

- **Compare_CEFEA.m**: This file is to compare and check the waveform of torque, induced voltage, flux linkage and flux density in the stator teeth and yoke obtained from CE-FEA and transient FEA.

- **RunMotorCAD_Fn.m**: this files invokes the MotorCAD to run the thermal analysis.

- **PerformanceCost_Fn.m**: Calculate and display the output data such as the average torque, torque ripple, core losses and material cost on the screen.

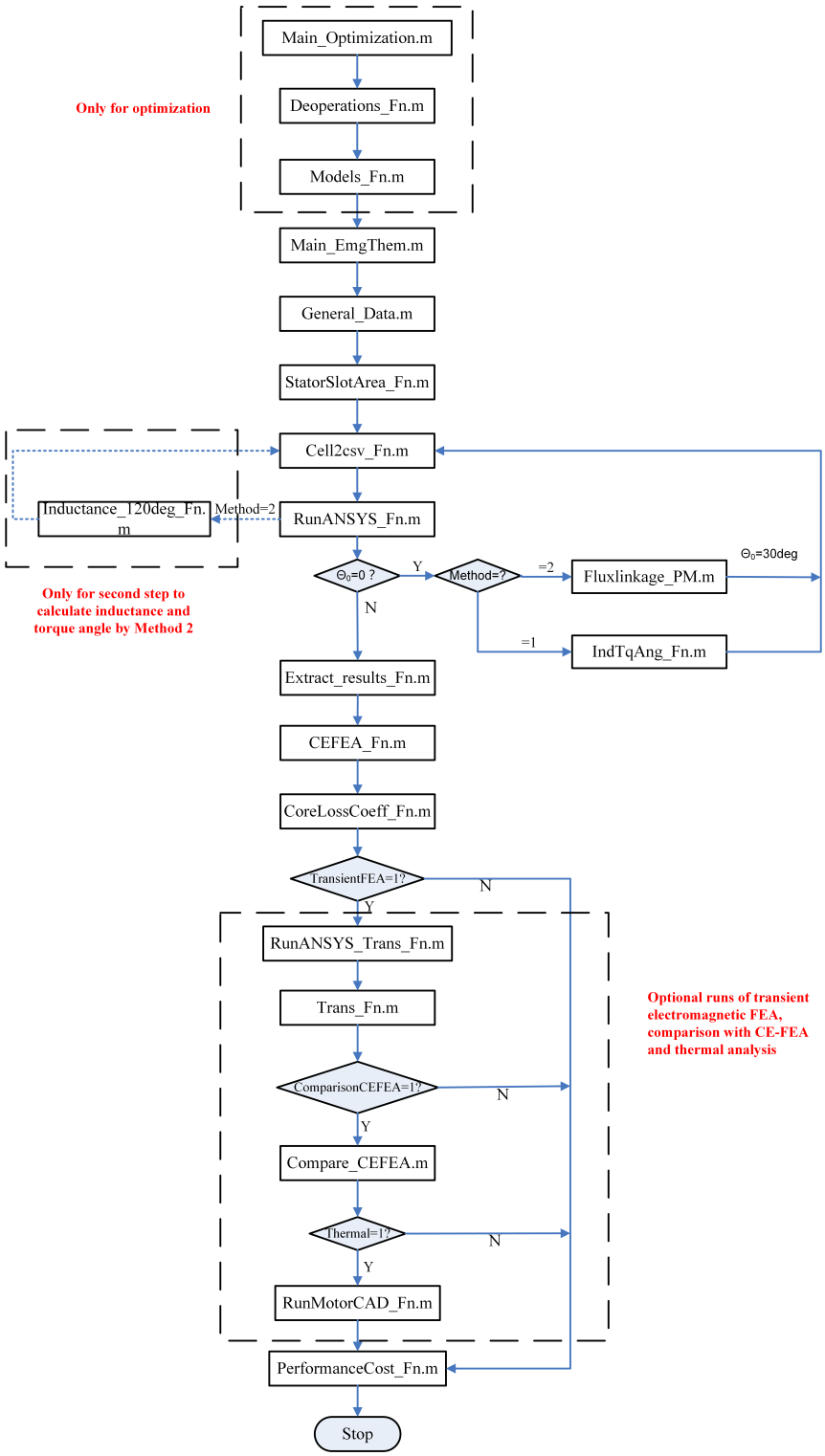

Figure 3.4: Script work flow for coupling.

CHAPTER 4

Optimal Design Studies

In this chapter, an approach for solving constrained optimization problems, based on combining multi-objective optimization with differential evolution (CMODE) proposed by Yong Wang and Zixing Cai, is employed to optimize an IPM synchronous machine and a SyncRel machine [70]. In this automated design optimization method, the DE algorithm is used as a global design optimization tool and CE-FEA is used to calculate machine's performances including the torque profile, emf/induced voltage and losses (stator iron and copper), etc.. In order to speed up the optimization process, the distributed solve option (DSO) of ANSYS Maxwell software package is employed.

4.1 IPM synchronous machine example

In this section, an automated design optimization utilizing CE-FEA and DE algorithm is performed on a prototyped IPM, for which the cross-section is shown in Figure 4.1. Following are the design specifications for this IPM machine:

- Rated power: 10hp
- Rated speed: 1800rpm

- Motor frame: 210-frame
- Stator specifications:
  - 36 slots
  - outer diameter: 233.3mm
  - three phase distributed winding (as shown in Figure 4.2)
  - slot fill factor: 0.4
  - winding current density: $4.3 A_{rms}/mm^2$
- Rotor specifications:
  - 6 poles
  - shaft diameter: 23.8mm
  - interior V-type PM
  - PMs operating at a temperature resulting in $\mu_R = 1.05, Br = 1.10T$.

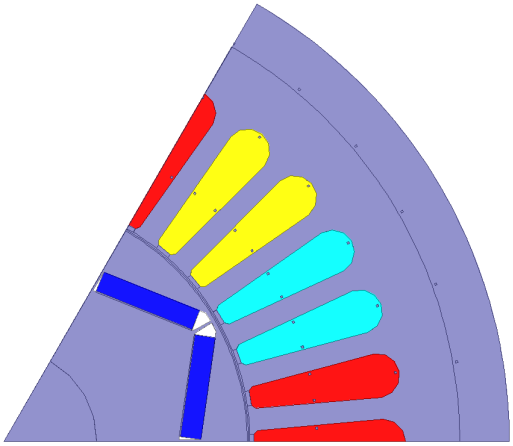

Figure 4.1: Cross-section and geometry of the V-type IPM machine with 36-slot 6-pole.

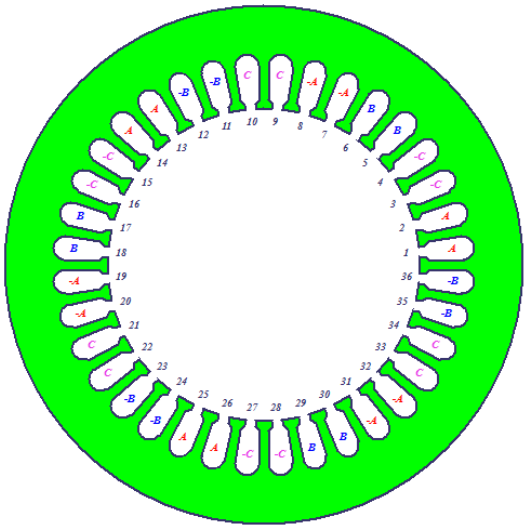

Figure 4.2: Explanatory of the distributed winding for the 36-slot 6-pole IPM machine.

4.1.1 Objectives and constraints

Objectives

In the process of automated multi-objective optimization of the IPM machine, two objectives and two constraints are taken into consideration:

1. Minimize the material costs, with the cost estimation function as follows:

$$cost = 64 \cdot m_{PM} + 8.25 \cdot m_{Cu} + 1 \cdot m_{Fe} \ , \tag{4.1}$$

   where m_{PM}, m_{Cu} and m_{Fe} are the masses of the permanent magnet, copper and steel which are in unit of kg, respectively.

2. Minimize the total losses of the electric machine with the following function:

$$P_{loss} = P_{Cu} + P_{stator\_Fe} + P_{PM} + P_{mech} \ , \tag{4.2}$$

   where P_{Cu} is the copper loss, P_{stator_Fe} is the stator core loss, P_{PM} is the permanent magnet loss and P_{mech} is the mechanical loss.

Constraints

1. Minimum flux density in permanent magnet, B_{min}, under rated load, greater than $0.3B_r$, where B_r is the retentivity which is equal to 1.1T in this work.

2. Torque ripple $\leq 20\%$, where $torque\ ripple = \frac{T_{e\_max} - T_{e\_min}}{T_{e\_ave}}$

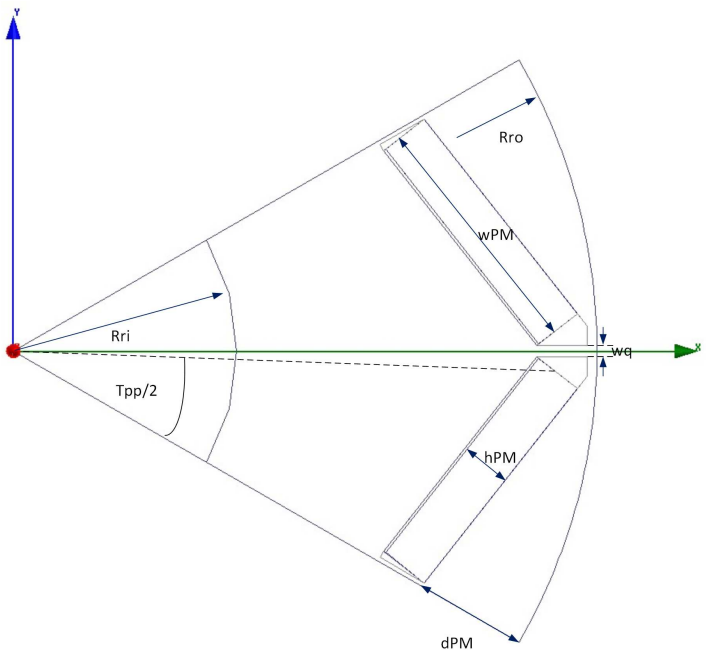

Figure 4.3: Cross-section and geometric parameters of the rotor for the 36-slot 6-pole IPM V-type machine.

4.1.2 Parametric models and independent variables

The stator parametric model for the IPM machine in this case study is previously described by Figure 3.1 in section 3.1. For the V-type PM layout with 2 segments per pole as shown in Figure 4.3, the independent rotor geometric parameters are given as follows:

1. h_{PM}: PM height in the direction of magnetization

2. r_{wpm}: PM width ratio, $r_{wpm} = w_{PM}/w_{PM\_max}$

3. r_{dpm}: PM depth ratio, $r_{dpm} = R_{ro}/R_{ri}$

Table 4.1: Specification of independent geometric parameters for the 36-slot 6-pole IPM prototype machine.

Stator			
Variable	Unit	Minimum value	Maximum value
Y_T	[mm]	12.7	19.05
h_g	[mm]	0.7	1.3
r_{si_so}		0.55	0.72
r_{t_sp}		0.35	0.55
r_{tip_so}		0.3	0.8
Rotor			
h_{PM}	[mm]	2.5	4.75
r_{wpm}		0.8	0.93
r_{dpm}		0.21	0.55
r_{wq}		0.2	0.7
τ_{pp}	[deg]	40	54.5

4. r_{wq}: q-axis bridge width ratio, $r_{wq} = wq/wq_{max}$, where wq is the q-axis bridge width and wq_{max} is the maximum q-axis bridge width

5. τ_{pp}: pole coverage

Provided in Table 4.1 are the ranges for the independent variables. For each candidate design, the stack length was scaled to achieve the rated power.

4.1.3 Optimization studies

One of the objectives in this optimization problem is to test the DSO(s), including the accuracy and speed. In the process of optimization, the DE algorithm generated one initial population which included 70 individuals per generation, and 50 generations (70 individuals in each generation). As a results, 3,570 designs were analyzed.

Table 4.2: Comparison of optimization with and without DSO(s).

	Optimization with 10 DSOs	Optimization without DSO
Individuals in initial population	70	70
Total generations	50	50
Individuals in one generation	70	70
Total number of DE designs	3570	3570
Total computational time [hours]	58.7	75.4
Average computational time for one design [seconds]	29.6	38

Furthermore, to accurately estimate the performance of the designs, torque angle estimation was performed, which lead to that each design was simulated twice by ANSYS Maxwell. As shown in Table 4.2, the computational time has been reduced by utilizing the DSO function in ANSYS Maxwell. The expected computational time using DSOs should be reduced linearly according to the number of DSOs utilized. A benchmark study on the relationship between the computational time and the number of DSOs utilized is presented in section 4.1.4.

Provided in Figure 4.4 to Figure 4.7 are the side by side comparison of the optimization results with and without DSO(s), which indicate that not only the parallel processing has been implemented, but also the results are comparable with the results of the series optimization. The scatter plot for all DE designs for the IPM machine is shown in Figure 4.6. Furthermore, to check the stability of the parallel processing, a second run of the optimization with 10 DSOs is utilized. The results of the first run and second run are compared side by side showing in (a) and (b) from Figure 4.4 to Figure 4.7. Shown in Figure 4.7 are the designs with a torque ripple lower than 20%.

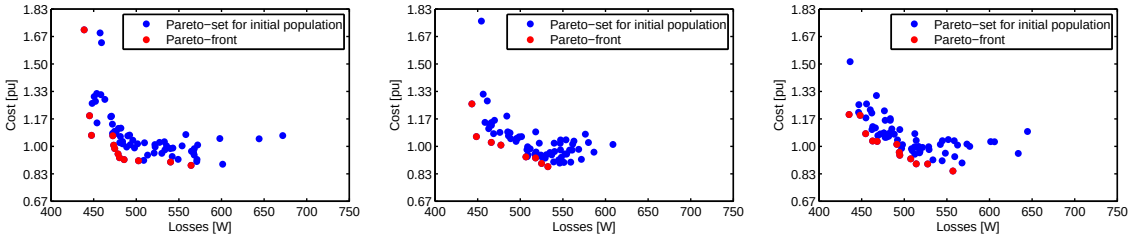

(a) Optimization with 10 DSOs (b) Optimization with 10 DSOs (second run) (c) Optimization without DSO

Figure 4.4: Scatter plot of initial population for the 36-slot 6-pole V-type IPM machine.

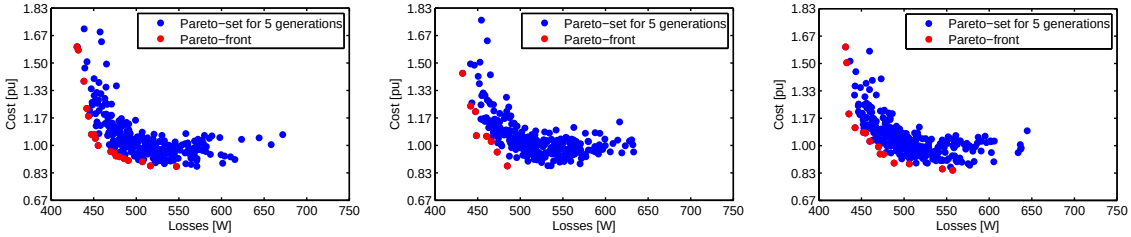

(a) Optimization with 10 DSOs (b) Optimization with 10 DSOs (second run) (c) Optimization without DSO

Figure 4.5: Scatter plot of 5 DE generations for the 36-slot 6-pole V-type IPM machine.

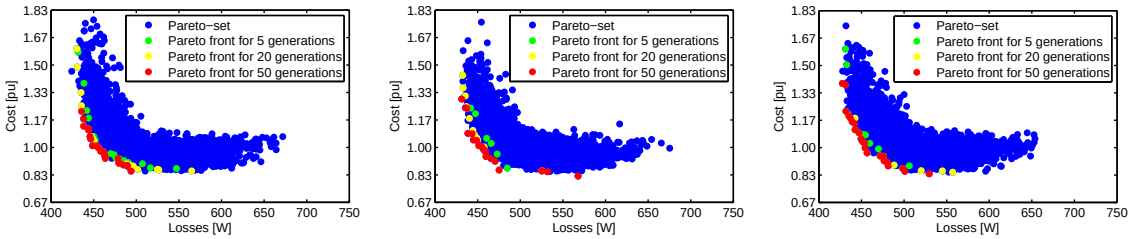

(a) Optimization with 10 DSOs (b) Optimization with 10 DSOs (second run) (c) Optimization without DSO

Figure 4.6: Scatter plot of all DE designs for the 36-slot 6-pole V-type IPM machine.

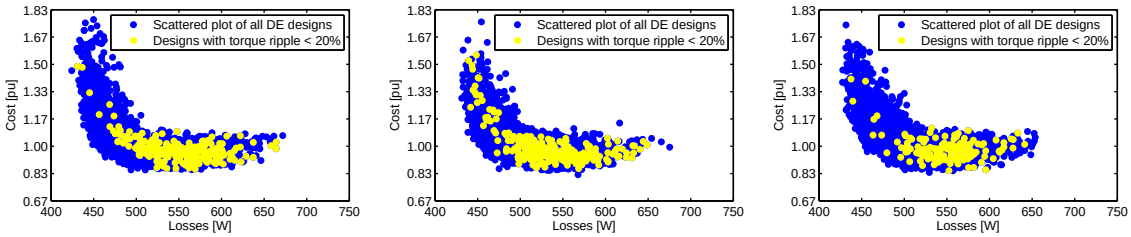

(a) Optimization with 10 DSOs. (b) Optimization with 10 DSOs, second run. (c) Optimization without DSO.

Figure 4.7: Scatter plot of all DE designs and the designs with the torque ripple lower than 20% for the 36-slot 6-pole V-type IPM machine.

4.1.4 Benchmark study

A benchmark study focusing on the relationship between the simulation time and the number of DSOs used was performed on the IPM machine. The results in Table 4.3 indicate that although a reduction in time can be achieved using the distributed solving option (DSO), but the reduction was not linear with the number of parallel solvers employed.

It should also be noted that the differences recorded in between computers were not necessarily expected being given the hardware characteristics, and that there may be possible software installations and operating system variations. Yet another possible cause could be the fact that the analysis method is indeed very fast but requires significant time for data communication. Finally, more investigations are required on this topic.

Table 4.3: Total time for automatically simulating 3 generations (70 designs per generation, 210 designs in total).

Workstation characteristics				
Model	Dell Precision T7600		Dell Precision T7600	
CPU	2 x Intel (R) Xeon (R) E5-2667 0 - 2.90GHz		2 X Intel (R) Xeon (R) E5-2620 0 - 2.0GHz	
Cores	24		24	
Installed memory (RAM)	32GB		16GB	
Number of DSO	Total time [h]	Total time [s]	Total time [h]	Total time [s]
1	4h25m41s	15941	6h24m15s	23041
4	3h50m30S	13830	3h12m42s	12062
5	3h08m35s	11315	2h55m58s	10558
6	3h08m20s	11300	2h51m29s	10289
7	3h09m58s	11398	2h40m14s	9614
8	3h06m52s	11212	3h03m19s	10999
9	3h08m56s	11336	3h24m47s	12287
10	3h26m58s	12418	2h59m33s	10773

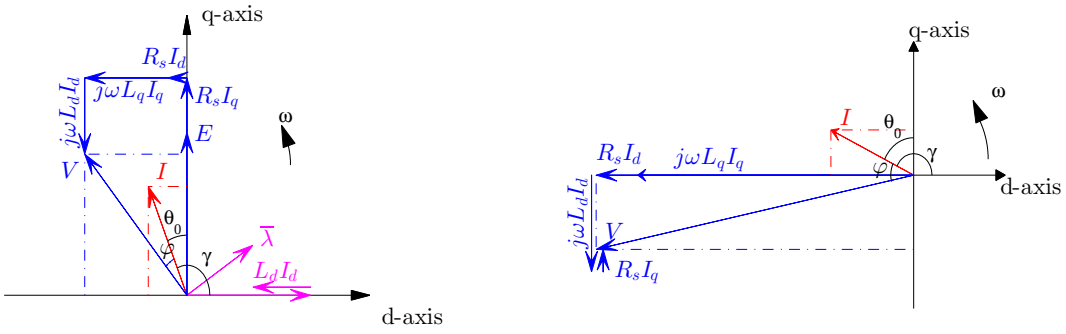

(a) PM machine

(b) SynRel machine

Figure 4.8: Synchronous machine phasor diagram expressed in rotor reference frame.

4.2 Synchronous reluctance machine example

In this section, the design optimization and modeling for a synchronous reluctance machine (286-frame, 36-slot and 4-pole) utilizing CE-FEA and CMODE [70] is described. According to Cupertino and Pellegrino, to reduce the computational time per candidate machine, the torque angle is considered as an independent variable in this optimization problem [49]. In the process of optimization, the DE algorithm generated one initial population which included 100 individuals, and 50 generations (100 individuals per generation). As a result, 5100 designs were analyzed.

Provided in Figure 4.8b is the phasor diagram of the SynRM in steady state in the d-q axes reference frame linked to rotor, where φ is the power factor angle and γ is the torque angle , and θ_0 current space phasor angle.

4.2.1 Objectives and constraints

Five optimization problems of SyncRel machines have been studied. Based on the literature review in Chapter 1, high torque ripple and low power factor are the characteristics of SyncRel machines. "Badness", defined as the ratio of the total losses to the electromagnetic torque, which is a comprehensive representative of the losses and torque. Thus, it can be considered as an objective. Also, to prevent the motor drive from the over-modulation operation, the induced phase voltage should be taken into consideration. Thus, the toruqe ripple, power factor, badness and induced voltage are considered as objectives and/or constraints in five different optimization problems and will be described in detail in each problem.

4.2.2 Parametric model and independent variables

In this section, three different rotor typologies, four barriers per pole (see Figure 4.9), three barriers per pole and PMaSyncRel, for which three permanent magnets could be inserted into the "U" parts or only the bottom of the three flux barriers, will be described and studied in this section. The 36-slot stator is the one from the 36-slot 4-pole V-Type IPM machine with 10hp Rating at 1800rpm, which is previously described in section 3.1. Mean while, in order to robust the parametric model and avoid overlapping in the design optimization procedure, the geometric parameters are ratio parameterized. For the independent geometric variables, the minimum and

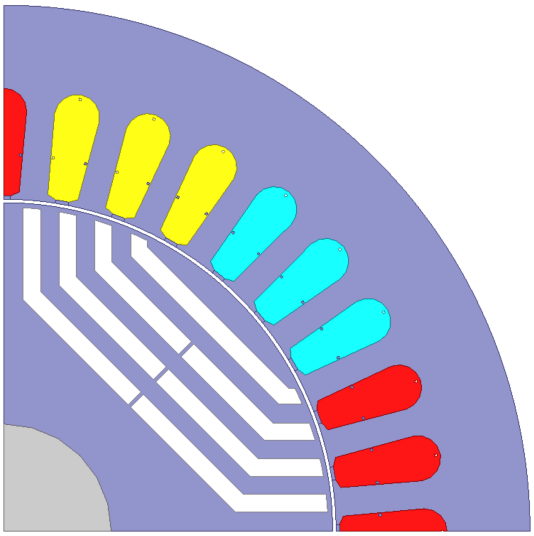

Figure 4.9: ANSYS Maxwell model of a synchronous reluctance machine (286 frame 36-slot 4-pole) with 4 rotor layers per pole.

maximum values are always set in the typical range of ± 20% of the conventional parameters, and for the current phase angle, θ_0, is in the range of 50°and 75°.

Synchronous reluctance rotor with four flux barriers

For the synchronous reluctance machine with 4 layers per pole as shown in Figure 4.10, the descriptions of all the geometric parameters are given as follows:

- Independent rotor geometric parameters:

  1. P: number of rotor poles
  2. R_{ri}: rotor inner radius
  3. R_{ro}: rotor outer radius

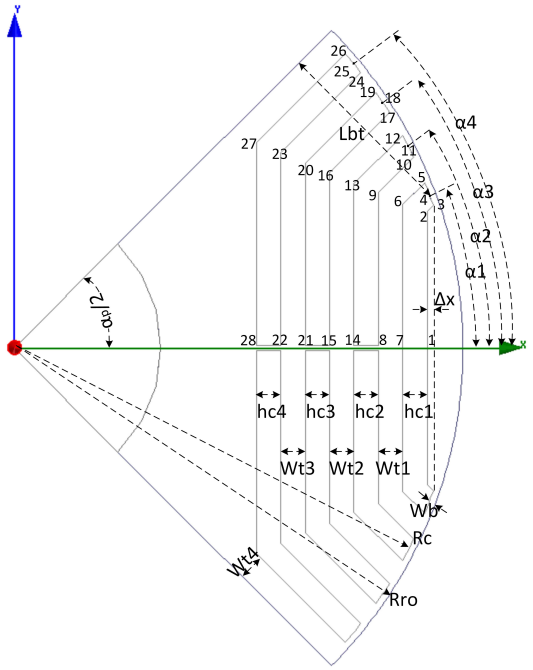

Figure 4.10: Cross-section and geometric parameters of a synchronous reluctance machine with 4 layers per pole.

4. Wb: bridge width from the top of the rotor barrier to the rotor outer surface

5. Wbb: rotor barrier bridge width

6. Δx: displacement factor, accounting for how deeply are the barriers positioned, radial wise.

7. Kbt: the ratio of the total length of the barriers and flux tubes to the maximum total length, $Kbt = \dfrac{Lbt}{Rc \cdot sin(\alpha_p/2)}$

8. Kb: the ratio of the total barrier thicknesses to the total length of the flux barriers and tubes, $Kb = \dfrac{hct}{Lbt}$

9. $Kb1$: the ratio of the thicknesses of the first barrier to the total barrier thicknesses, $Kb1 = \dfrac{hc1}{2 \cdot hct}$

10. $Kb2$: the ratio of the thicknesses of the second barrier to the total barrier thicknesses of the second, third and fourth barrier, $Kb2 = \dfrac{hc2}{hct - hc1/2}$

11. $Kb3$: the ratio of the thicknesses of the third barrier to the total barrier thicknesses of the third and fourth barrier, $Kb3 = \dfrac{hc3}{hct - hc1/2 - hc2}$

12. $Kb4$: the ratio of the thicknesses of the fourth barrier to the sum of the fourth barrier thickness and tube width,
$Kb4 = \dfrac{hc4}{Lbt - hc1/2 - hc2 - hc3 - Wt1 - Wt2 - Wt3}$

13. $Kt1$: the ratio of the first flux tube width to the total tube width, $Kt1 = \dfrac{Wt1}{Wt}$

14. $Kt2$: the ratio of the second flux tube width to the total width of the second, third and fourth flux tube, $Kt2 = \dfrac{Wt2}{Wt - Wt1}$

15. $Kt3$: the ratio of the third flux tube width to the total width of the third and fourth flux tube,$Kt3 = \dfrac{Wt3}{Wt - Wt1 - Wt2}$

- Auxiliary calculated geometric variables and expressions can be deduced based on the input geometric variables, which are listed as follows:

1. α_p: pole pitch, mechanical degree, $\alpha_p = 360/P$

2. Rc: radius of the barrier top central, $Rc = Rro - Wb$

3. α_1: angular position of the first barrier at the airgap, $\alpha_1 = \alpha_p/2 - asin((Wt4 + Wt3 + Wt2 + Wt1 + hc4 + hc3 + hc2 + hc1/2)/Rc)$
4. α_2: angular position of the second barrier at the airgap, $\alpha_2 = \alpha_p/2 - asin((Wt4 + Wt3 + Wt2 + hc4 + hc3 + hc2/2)/Rc)$
5. α_3: angular position of the third barrier at the airgap, $\alpha_3 = \alpha_p/2 - asin((Wt4 + Wt3 + hc4 + hc3/2)/Rc)$
6. α_4: angular position of the fourth barrier at the airgap, $\alpha_4 = \alpha_p/2 - asin((Wt4 + hc4/2)/Rc)$
7. α_{p3}: angular position of point 3, $\alpha_{p3} = \alpha_1 - asin(hc1/2/Rc)$
8. α_{p5}: angular position of point 5, $\alpha_{p5} = \alpha_1 + asin(hc1/2/Rc)$
9. α_{p10}: angular position of point 10, $\alpha_{p10} = \alpha_2 - asin(hc2/2/Rc)$
10. α_{p12}: angular position of point 12, $\alpha_{p12} = \alpha_2 + asin(hc2/2/Rc)$
11. α_{p17}: angular position of point 17, $\alpha_{p17} = \alpha_3 - asin(hc3/2/Rc)$
12. α_{p19}: angular position of point 19, $\alpha_{p19} = \alpha_3 + asin(hc3/2/Rc)$
13. α_{p24}: angular position of point 24, $\alpha_{p24} = \alpha_4 - asin(hc4/2/Rc)$
14. α_{p26}: angular position of point 26, $\alpha_{p24} = \alpha_4 + asin(hc4/2/Rc)$
15. Lbt: total length of the flux barriers and tubes, $Lbt = Kbt \cdot Rc \cdot sin(\alpha_p/2)$
16. hct: total barrier thickness, $hct = Lbt \cdot Kb$

17. Wt: total width of the flux tube, $Wt = Lbt - hct$

18. $Wt1$: width of the first flux tube, $Wt1 = Wt \cdot Kt1$

19. $Wt2$: width of the second flux tube, $Wt2 = (Wt - Wt1) \cdot Kt2$

20. $Wt3$: width of the third flux tube, $Wt3 = (Wt - Wt1 - Wt2) \cdot Kt3$

21. $Wt4$: width of the fourth flux tube, $Wt4 = hc4/Kb4 - hc4$

22. $hc1$: thickness of the first barrier, $hc1 = 2hct \cdot Kb1$

23. $hc2$: thickness of the second barrier, $hc2 = (hct - hc1/2) \cdot Kb2$

24. $hc3$: thickness of the third barrier, $hc3 = (hct - hc1/2 - hc2) \cdot Kb3$

25. $hc4$: thickness of the fourth barrier, $hc4 = (Lbt - hc1/2 - hc2 - hc3 - Wt1 - Wt2 - Wt3) \cdot Kb4$

For the points defining the outlines of the geometry of the rotor cross-section shown in Figure 4.10, the x-y position/coordinate functions can be expressed as follows:

$$
\begin{cases} x_{r1} = x_{r2} \\ y_{r1} = 0 \end{cases}
$$

$$
\begin{cases} x_{r2} = x_{r3} - \Delta x \\ y_{r2} = y_{r3} - \Delta x \cdot \tan(\alpha_p/2) \end{cases}
$$

$$
\begin{cases} x_{r3} = Rc \cdot \cos(\alpha_{p3}) \\ y_{r3} = Rc \cdot \sin(\alpha_{p3}) \end{cases}
$$

$$
\begin{cases} x_{r4} = Rc \cdot \cos(\alpha_1) \\ y_{r4} = Rc \cdot \sin(\alpha_1) \end{cases}
$$

$$
\begin{cases} x_{r5} = Rc \cdot \cos(\alpha_{p5}) \\ y_{r5} = Rc \cdot \sin(\alpha_{p5}) \end{cases}
$$

$$
\begin{cases} x_{r6} = x_{r1} - hc1 \\ y_{r6} = y_{r5} - (x_{r5} - x_{r6}) \cdot \tan(\alpha_p/2) \end{cases}
$$

$$
\begin{cases} x_{r7} = x_{r1} - hc1 \\ y_{r7} = Wbb \end{cases}
$$

$$
\begin{cases} x_{r8} = x_{r1} - Wt1 \\ y_{r8} = Wbb \end{cases}
$$

$$
\begin{cases} x_{r9} = x_{r8} \\ y_{r9} = y_{r10} - (x_{r10} - x_{r9}) \cdot \tan(\alpha_p/2) \end{cases}
$$

$$
\begin{cases} x_{r10} = Rc \cdot \cos(\alpha_{p10}) \\ y_{r10} = Rc \cdot \sin(\alpha_{p10}) \end{cases}
$$

(4.3)

$$
\begin{cases} x_{r11} = Rc \cdot \cos(\alpha_2) \\ y_{r11} = Rc \cdot \sin(\alpha_2) \end{cases}
$$

$$
\begin{cases} x_{r12} = Rc \cdot \cos(\alpha_{p12}) \\ y_{r12} = Rc \cdot \sin(\alpha_{p12}) \end{cases}
$$

$$
\begin{cases} x_{r13} = x_{r9} - hc2 \\ y_{r13} = y_{r12} - (x_{r12} - x_{r13}) \cdot \tan(\alpha_p/2) \end{cases}
$$

$$
\begin{cases} x_{r14} = x_{r13} \\ y_{r14} = Wbb \end{cases}
$$

$$
\begin{cases} x_{r15} = x_{r14} - Wt2 \\ y_{r15} = Wbb \end{cases}
$$

$$
\begin{cases} x_{r16} = x_{r15} \\ y_{r16} = y_{r17} - (x_{r17} - x_{r16}) \cdot \mathtt{tan}(\alpha_p/2) \end{cases} \tag{4.4}
$$

$$
\begin{cases} x_{r17} = Rc \cdot \mathtt{cos}(\alpha_{p17}) \\ y_{r17} = Rc \cdot \mathtt{sin}(\alpha_{p17}) \end{cases}
$$

$$
\begin{cases} x_{r18} = Rc \cdot \mathtt{cos}(\alpha_3) \\ y_{r18} = Rc \cdot \mathtt{sin}(\alpha_3) \end{cases}
$$

$$
\begin{cases} x_{r19} = Rc \cdot \mathtt{cos}(\alpha_{p19}) \\ y_{r19} = Rc \cdot \mathtt{cos}(\alpha_{p19}) \end{cases}
$$

$$
\begin{cases} x_{r20} = x_{r16} - hc3 \\ y_{r20} = y_{r19} - (x_{r19} - x_{r20}) \cdot \mathtt{tan}(\alpha_p/2) \end{cases}
$$

$$
\begin{cases} x_{r21} = x_{r20} \\ y_{r21} = Wbb \end{cases}
$$

$$
\begin{cases} x_{r22} = x_{r21} - Wt3 \\ y_{r22} = Wbb \end{cases}
$$

$$
\begin{cases} x_{r23} = x_{r22} \\ y_{r23} = y_{r24} - (x_{r24} - x_{r23}) \cdot \texttt{tan}(\alpha_p/2) \end{cases}
$$

$$
\begin{cases} x_{r24} = Rc \cdot \texttt{cos}(\alpha_{p24}) \\ y_{r24} = Rc \cdot \texttt{sin}(\alpha_{p24}) \end{cases}
$$

$$
\begin{cases} x_{r25} = Rc \cdot \texttt{cos}(\alpha_4) \\ y_{r25} = Rc \cdot \texttt{sin}(\alpha_4) \end{cases} \tag{4.5}
$$

$$
\begin{cases} x_{r26} = Rc \cdot \texttt{cos}(\alpha_{p26}) \\ y_{r26} = Rc \cdot \texttt{sin}(\alpha_{p26}) \end{cases}
$$

$$
\begin{cases} x_{r27} = x_{r23} - hc4 \\ y_{r27} = y_{r26} - (x_{r26} - x_{r27}) \cdot \texttt{tan}(\alpha_p/2) \end{cases}
$$

$$
\begin{cases} x_{r28} = x_{r27} \\ y_{r28} = Wbb \end{cases}
$$

Synchronous reluctance rotor with three flux barriers

The synchronous reluctance machine with three rotor barriers in Figure 4.11 could be obtained by eliminating the 4th barrier determined by hc4 in Figure 4.10. The expressions of $hc1$, $hc2$, $Wt1$, $Wt2$ are same as expressions for the 4 barriers rotor. The differences are the expressions of $hc3$, $Wt3$, α_1, α_2 and α_3:

- $hc3$: thickness of the third barrier, $hc3 = (Lbt - hc1/2 - hc2 - Wt1 - Wt2) \cdot Kb3$

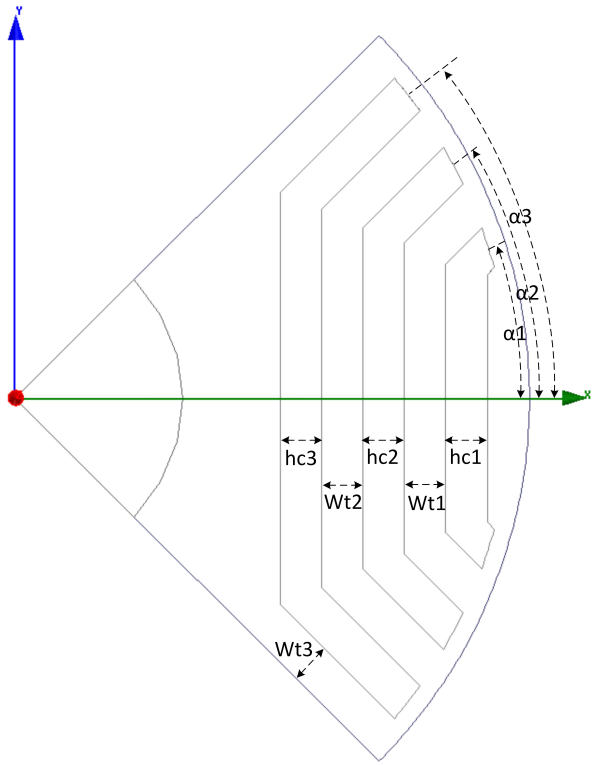

Figure 4.11: Cross-section and geometric parameters of a synchronous reluctance machine with three flux barriers per pole.

- $Wt3$: width of the third flux tube, $Wt3 = hc3/Kb3 - hc3$
- α_1: angular position of the first barrier at the airgap, $\alpha_1 = \alpha_p/2 - asin((Wt3 + Wt2 + Wt1 + hc3 + hc2 + hc1/2)/Rc)$
- α_2: angular position of the second barrier at the airgap, $\alpha_2 = \alpha_p/2 - asin((Wt3 + Wt2 + hc3 + hc2/2)/Rc)$
- α_3: angular position of the third barrier at the airgap, $\alpha_3 = \alpha_p/2 - asin((Wt3 + hc3/2)/Rc)$

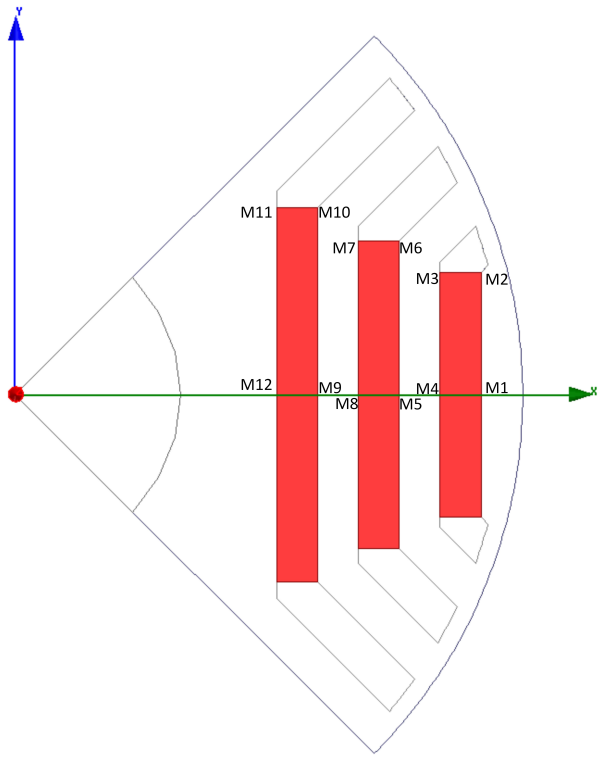

Figure 4.12: Cross-section and geometric parameters of a PM assisted synchronous reluctance machine with three layers per pole. In this example, rectangular blocks of permanent magnets completely fill in the barriers.

PM assisted synchronous reluctance rotor with three flux barriers

For the PMaSyncRel machine with three layers per pole shown in Figure 4.12, three additional geometric parameters are introduced:

- $Kpm1$: the width ratio of the first PM to the first flux barrier, $Kpm1 = \frac{y_{M2}}{y_{r2}}$
- $Kpm2$: the width ratio of the second PM to the second flux barrier, $Kpm2 = \frac{y_{M3}}{y_{r9}}$
- $Kpm3$: the width ratio of the third PM to the third flux barrier, $Kpm3 = \frac{y_{M10}}{y_{r16}}$

For the points defining the outlines of permanent magnets shown in Figure 4.12, the x-y position/coordinate functions can be expressed as follows:

$$
\begin{cases} x_{M1} = x_{r1} \\ y_{M1} = y_{r1} \end{cases}
\begin{cases} x_{M2} = x_{r2} \\ y_{M2} = y_{r1} \end{cases}
\begin{cases} x_{M3} = x_{r7} \\ y_{M3} = Kpm1 \cdot y_{r2} \end{cases}
\begin{cases} x_{M4} = x_{r7} \\ y_{M4} = y_{r1} \end{cases}
\begin{cases} x_{M5} = x_{r8} \\ y_{M5} = y_{r8} \end{cases}
\begin{cases} x_{M6} = x_{r8} \\ y_{M6} = Kpm2 \cdot y_{r9} \end{cases}
\begin{cases} x_{M7} = x_{r14} \\ y_{M7} = Kpm2 \cdot y_{r9} \end{cases}
\begin{cases} x_{M8} = x_{r14} \\ y_{M8} = y_{r14} \end{cases}
\begin{cases} x_{M9} = x_{r15} \\ y_{M9} = y_{r15} \end{cases}
\begin{cases} x_{M10} = x_{r15} \\ y_{M10} = Kpm3 \cdot y_{r16} \end{cases}
\tag{4.6}
$$

$$\begin{cases} x_{M11} = x_{r21} \\ y_{M11} = y_{r10} \end{cases}$$

$$\begin{cases} x_{M12} = x_{r21} \\ y_{M12} = y_{r21} \end{cases}$$

4.2.3 Problem A - minimize badness and torque ripple

For the first optimization problem performed on the SyncRel machine with four layers per pole, two objectives and one constraint are taken into consideration:

- **Objectives**

  1. Minimize "badness", i.e. the function:

$$B_d = \frac{\sqrt{W_T}}{T_e} \ , \tag{4.7}$$

     where W_T is the total losses [W] and T_e is the average electromagnetic torque [Nm].

  2. Minimize the torque ripple of the electric machine with the following function:

$$T_{rpk} = \frac{T_{e\_max} - T_{e\_min}}{T_e} \ , \tag{4.8}$$

     where T_{e_max} and T_{e_min} are the maximum and minimum value of the electromagnetic torque.

- **Constraints**

  1. Minimum power factor 0.7

- **Independent variables**

  - Kb, Kbt, $Kb4$, $Kb3$, $Kb2$, $Kb1$, $Kt3$, $Kt2$, $Kt1$, θ_0

The Pareto-set of the badness and torque ripple for problem A is as shown in Figure 4.13. Provided in Figure 4.14 is the scatter plot of all candidate designs and the designs which meet the constraints mentioned above. An optimum design 4863 is selected from the Pareto-front and marked in Figure 4.14. The corresponding cross-section of the ANSYS Maxwell model is shown in Figure 4.31a and design information is provided in Table 4.4, respectively.

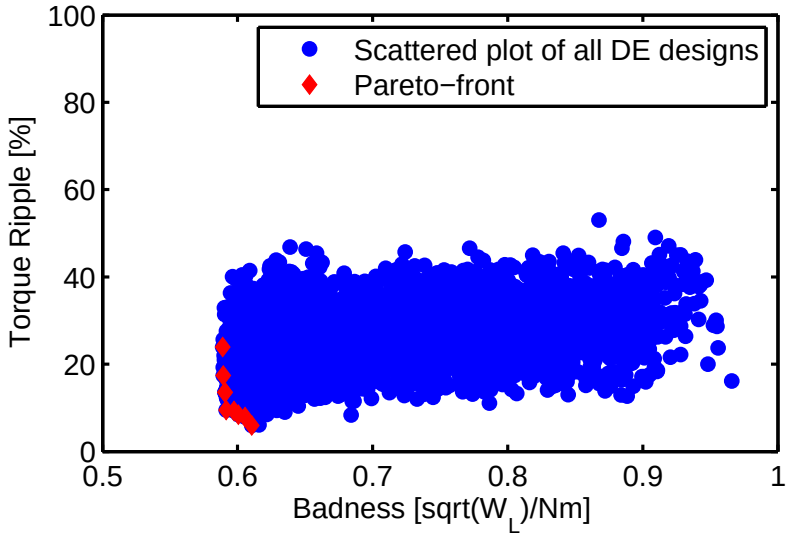

Figure 4.13: Problem A - Scatter plot of 5100 candidate SyncRel designs with four layers computed by the CE-FEA method (with torque ripple and badness as two objectives, power factor as the constraint).

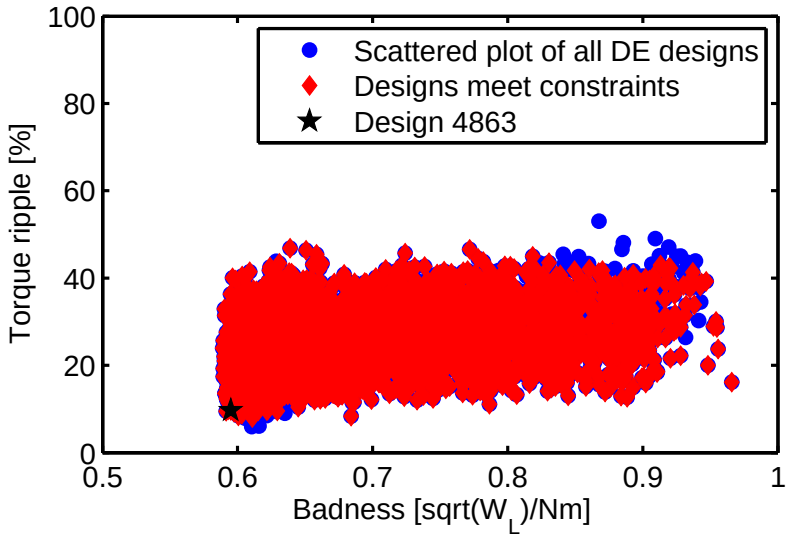

Figure 4.14: Problem A - Scatter plot of all candidate SyncRel designs with four layers and the designs meet the constraints (minimum power factor 0.7).

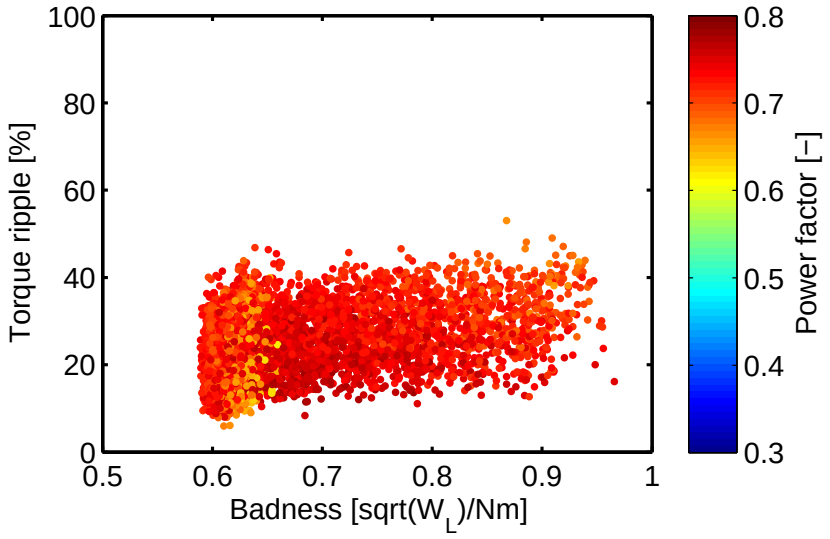

Figure 4.15: Problem A - Scatter plot of 5100 candidate SyncRel designs with four layers computed by the CE-FEA method (with torque ripple and badness as two objectives, power factor as the constraint).

4.2.4 Problem B - minimize badness and maximize power factor for both the SyncRel and PMaSyncRel

Synchronous reluctance machine optimization

In the second optimization problem, two objectives and one constraint are taken into consideration for the SyncRel and PMaSyncRel machines:

- **Objectives**

  1. Minimize the badness.

  2. Maximize power factor.

- **Constraints**

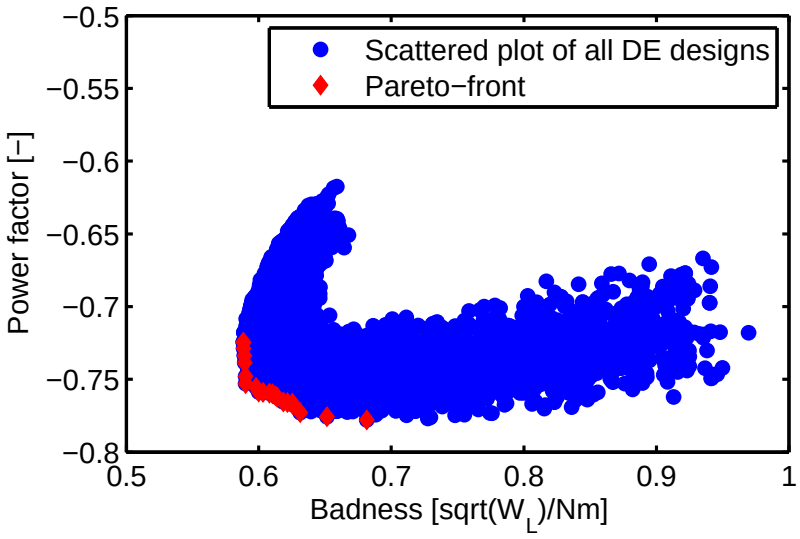

Figure 4.16: Problem B - Scatter plot of 5100 candidate SyncRel designs with four layers computed by the CE-FEA method (with power factor and badness as two objectives, torque ripple as the constraint).

1. Maximum torque ripple 20%

- **Independent variables**

  - For SyncRel machine: Kb, Kbt, $Kb4$, $Kb3$, $Kb2$, $Kb1$, $Kt3$, $Kt2$, $Kt1$, θ_0
  - For PMaSyncRel machine: Kb, Kbt, $Kb3$, $Kb2$, $Kb1$, $Kt2$, $Kt1$, θ_0, $Kpm1$, $Kpm2$, $Kpm3$

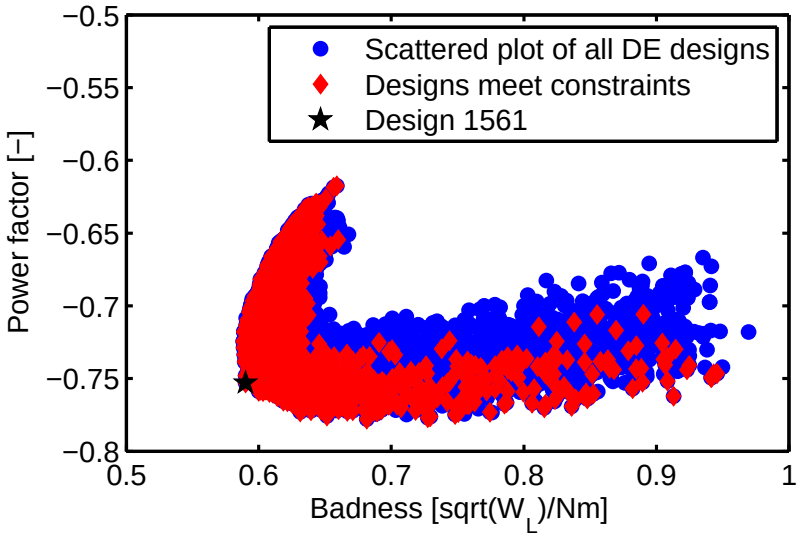

Figure 4.17: Problem B - Scatter plot of all candidate SyncRel designs with four layers and the designs meet the constraints (maximum torque ripple 20%), one recommended design 1561 is identified on the Pareto-front.

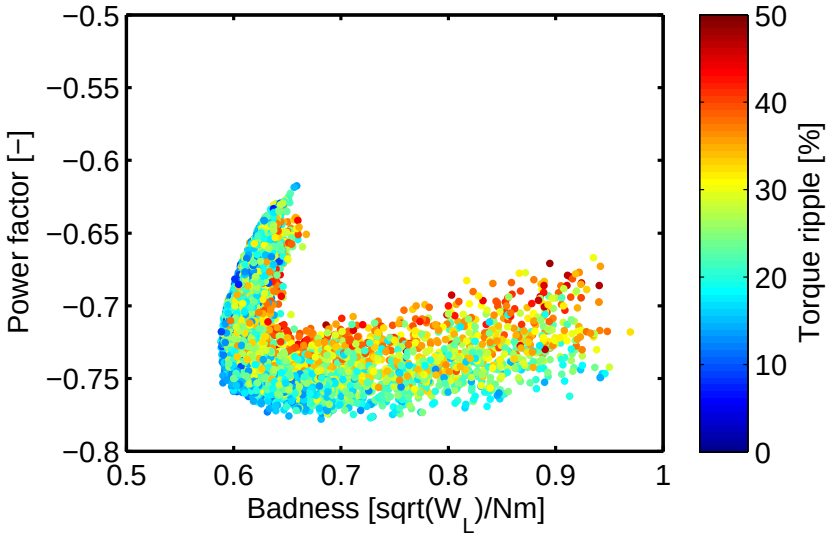

Figure 4.18: Problem B - Scatter plot of 5100 candidate SyncRel designs with four layers computed by the CE-FEA method (with power factor and badness as two objectives, torque ripple as the constraint).

The reason for selecting 20% as the maximum torque ripple is that even with skew effect reducing the torque ripple to half, *i.e.* 10%, which is typically acceptable for most applications. Shown in Figure 4.16 is the scatter plot of 5,100 candidate designs. Provided in Figure 4.17 is the scatter plot for all candidate designs and the designs which meet the constraints described previously. An optimum design 1561 is marked in Figure 4.17. The corresponding ANSYS Maxwell model is shown in Figure 4.31b and design information is provided in Table 4.4, respectively.

PM assisted synchronous reluctance machine optimization

To obtain a higher power factor, a PMaSyncRel machine, as shown in Figure 4.24a, was considered and optimized. The width of the PMs are determined by the PM width ratios Kpm1, Kpm2 and Kpm3.

Shown in Figure 4.19 is the scatter plot of 5,100 candidate designs from the design optimization of PMaSyncRel machines. Provided in Figure 4.20 is the scatter plot of all candidate designs and the designs which meet the constraints (torque ripple $< 20\%$). Th optimum designs, 1115 and 4508, were selected from these designs with toque ripple lower than 20% and marked in Figure 4.20. Another Pareto-set was obtained with a different range of θ_0, which is between 50°and 75°, as shown in Figure 4.22. Design 3824 was selected from the Pareto-front. The corresponding ANSYS Maxwell model is shown in Figure 4.24c and design information provided in Table 4.4, respectively.

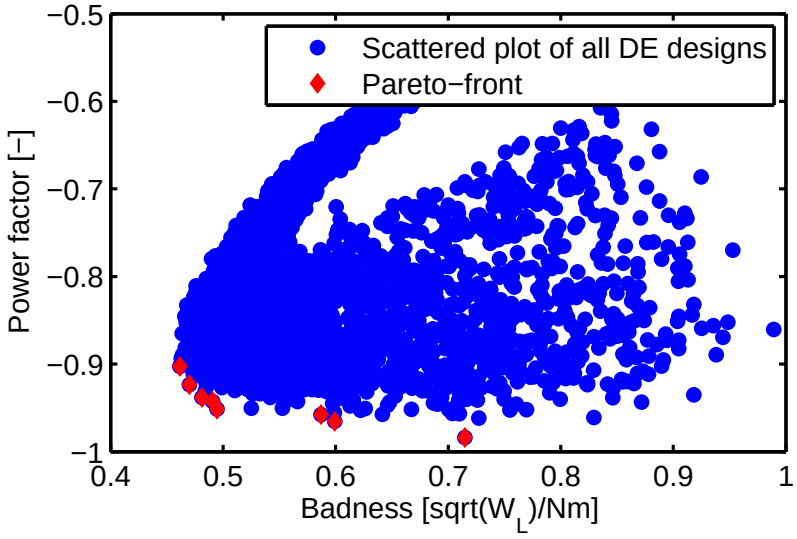

Figure 4.19: Problem B - Scatter plot of 5,100 candidate PMaSyncRel designs computed by the CE-FEA method (with power factor and badness as two objectives, torque ripple as the constraint).

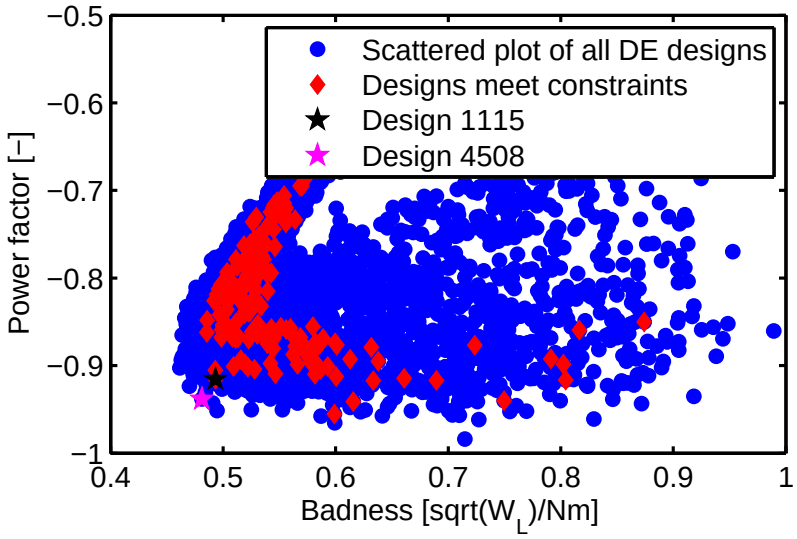

Figure 4.20: Problem B - Scatter plot of all candidate PMaSyncRel designs and the designs meet the constraints, maximum torque ripple 20%. One recommended design 1115, with a power factor of 0.916, badness of 0.493 and torque ripple of 18.4%,is identified on the Pareto-front. The upper and lower bounds of θ_0 are 30°to 75°.

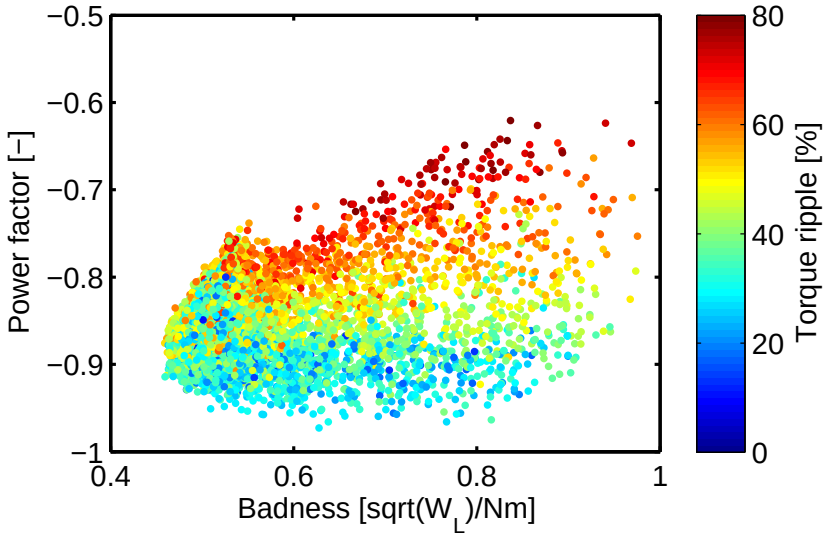

Figure 4.21: Problem B - Scatter plot of 5,100 candidate PMaSyncRel designs computed with the CE-FEA method (with power factor and badness as two objectives, torque ripple as the constraint).

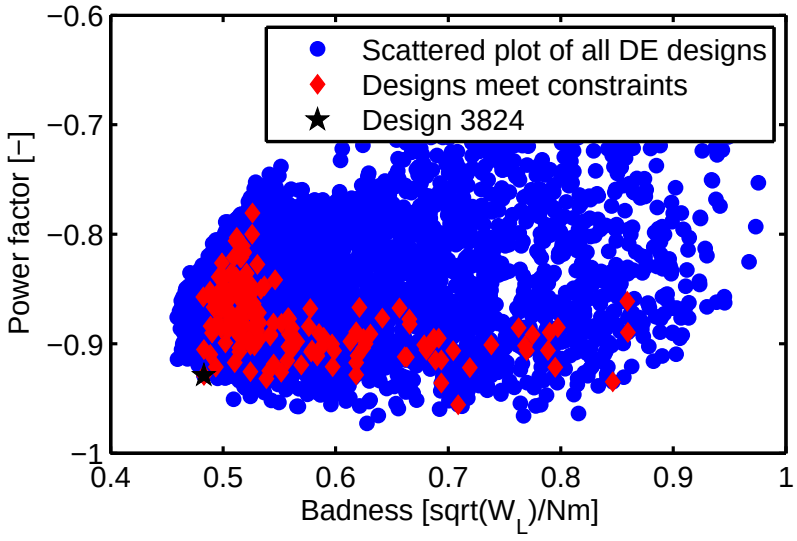

Figure 4.22: Problem B - Scatter plot of all candidate PMaSyncRel designs and the designs meet the constraint, torque ripple $\leq$ 20%. One recommended design 3824, which with power factor of 0.929, badness of 0.483 and torque ripple of 16%, is identified on the Pareto-front. The upper and lower bounds of θ_0 are 50°to 75°.

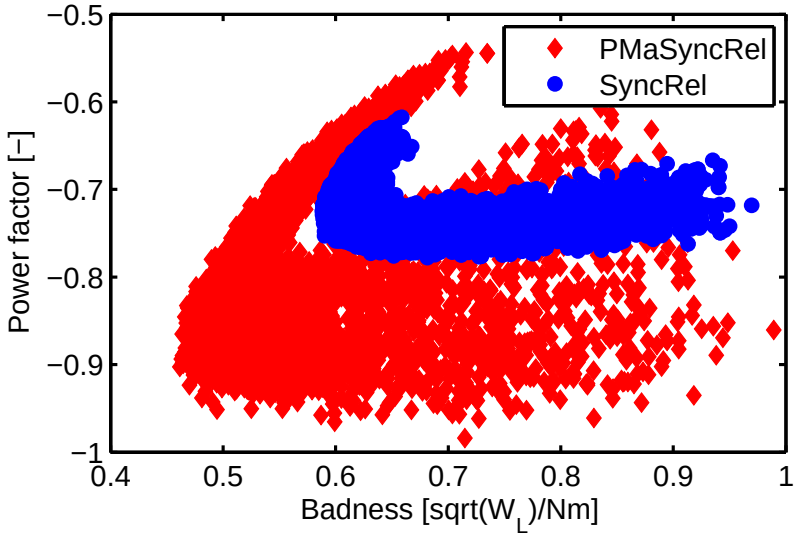

Figure 4.23: Problem B - Pareto-set comparison of optimization for SyncRel machine and PM assisted SyncRel machine to maximize power factor, minimize badness and limit torque ripple lower than 20%.

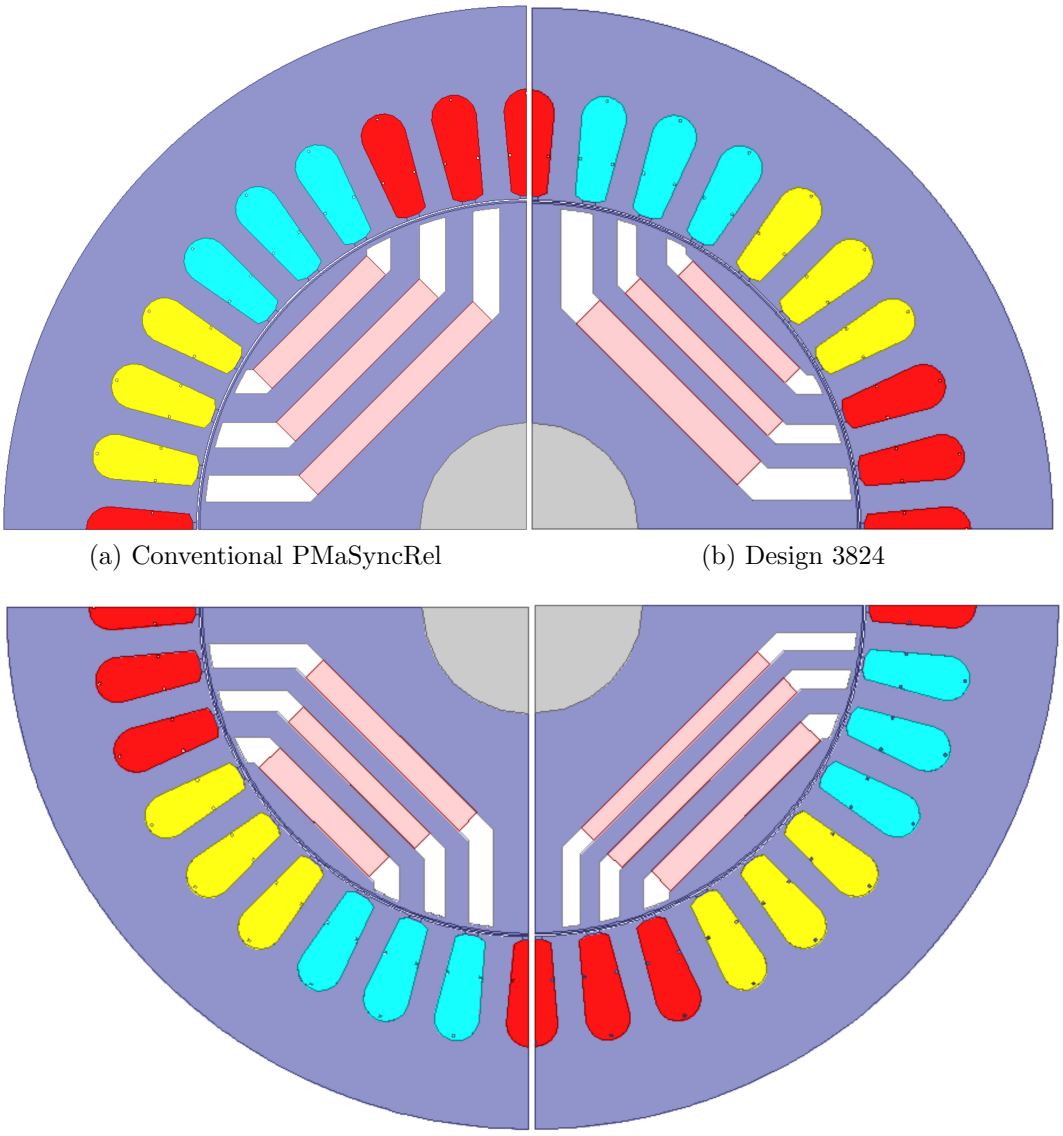

(a) Conventional PMaSyncRel (b) Design 3824

(c) Design 1115 (d) Design 4508

Figure 4.24: Cross-sections of PM assisted synchronous reluctance machines.

4.2.5 Problem C - maximize power factor, minimize badness and torque ripple

In the third optimization problem, three objectives are taken into consideration:

- **Objectives**
  1. Minimize badness
  2. Minimize torque ripple
  3. Maximize power factor
- **Constraints**
  1. This is a nonconstrained problem
- **Independent variables**
  - Kb, Kbt, $Kb4$, $Kb3$, $Kb2$, $Kb1$, $Kt3$, $Kt2$, $Kt1$, θ_0

As shown in Figure 4.25 is the scatter plot of 5,100 candidate designs. The results of the optimization study in the two-dimensional (2D) plane of badness versus power factor is shown in Figure 4.26. An optimum design 2165 is marked in Figure 4.26, for which the corresponding ANSYS Maxwell model is shown in Figure 4.31c and design information is provided in Table 4.4, respectively.

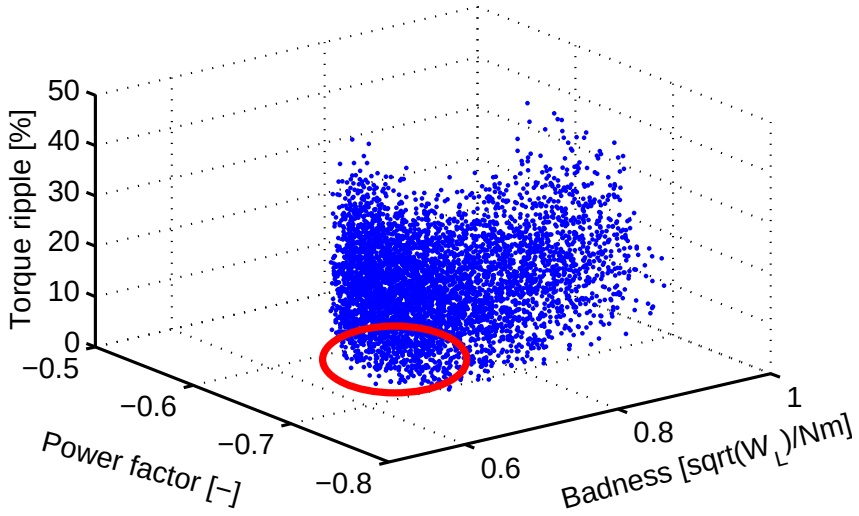

Figure 4.25: Problem C - 3D Scatter plot for optimization of SyncRel machine with 4 rotor barriers with 3 objectives.

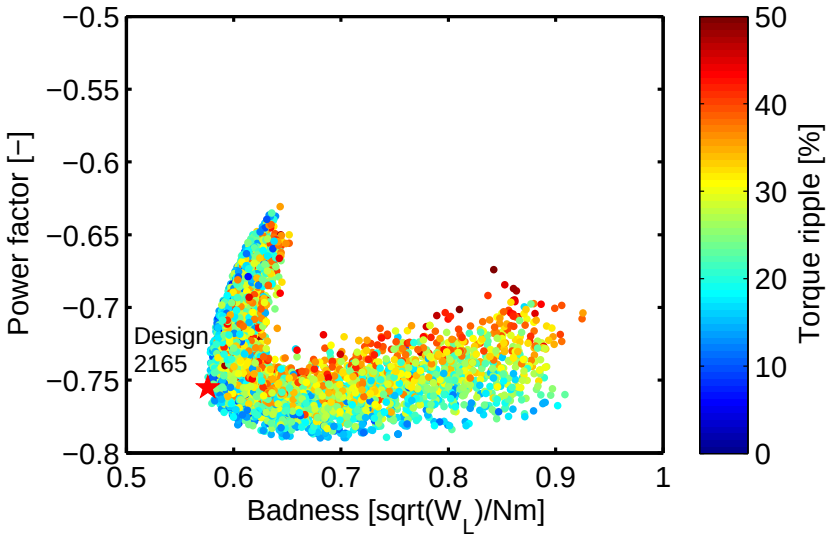

Figure 4.26: Problem C - Scatter plot of 5,100 candidate SyncRel designs with 4 rotor barriers computed by the CE-FEA method.

4.2.6 Problem D - maximize power factor only

In the fourth optimization problem performed on the SyncRel designs with four layers, the objective and constraint are:

- **Objectives**

  1. Maximize power factor.

- **Constraints**

  1. Maximum badness 0.65 $[\sqrt{W_L}/Nm]$.

- **Independent variables**

  - Kb, Kbt, $Kb4$, $Kb3$, $Kb2$, $Kb1$, $Kt3$, $Kt2$, $Kt1$, θ_0

The low power factor is a characteristic for synchronous reluctance machines as already acknowledged in literature [20]. In order to make sure that the full potential is fully exploited, an optimization on emphasis on the power factor has been conducted. A single objective optimization for maximizing power factor with constraint for minimum badness of 0.65 $[\sqrt{W_L}/Nm]$ was investigated.

As shown in Figure 4.28, most of the designs are grouped in the "badness" region of 0.6 to 0.65. However, the results for power factor are spread over a wide range. For each generation, the multi-generational improvement of the power factor can not be simply achieved. From an engineering point of view, this confirmed that the power

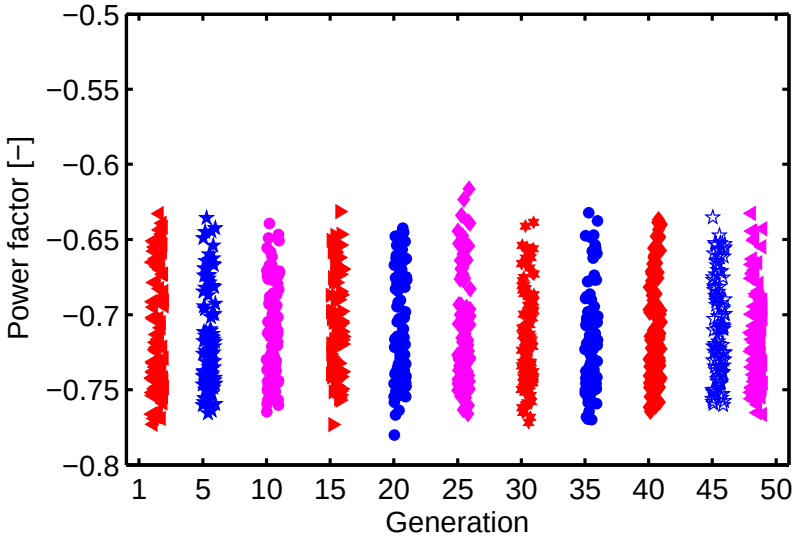

Figure 4.27: Problem D - Power factor of the candidate SyncRel designs with four layers.

factor can not be further improved. Nevertheless, further mathematical investigation, which is beyond the scope of the current project, is recommended as future work.

Further investigation was performed for the designs, which with high power factor over 0.77, indicates that these designs have high badness as well. Shown in Figure 4.30 are the cross-sections of the selected designs with high power factors and high badness. For Design 2103, with power factor of 0.780 and badness of 0.74, the manufacturing may become challenging and the mechanical strength could be an issue since the thickness of the second flux guide is only 2.99mm. Design 3092, shown in Figure 4.31d, is selected from the designs with the power factor in the range of 0.750 to 0.775 and the badness lower than 0.65.

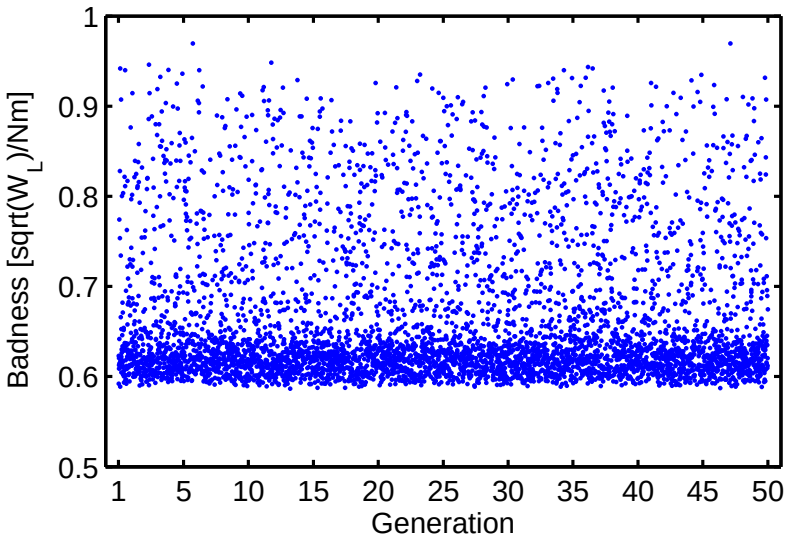

Figure 4.28: Problem D - Scatter plot of 5100 candidate SyncRel designs with four layers showing the minimum for the specified constraints rating and badness limitation.

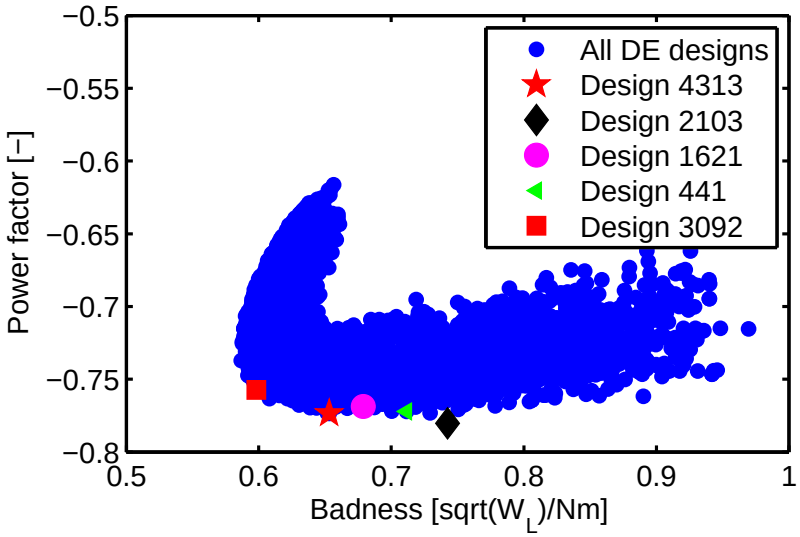

Figure 4.29: Problem D - Scatter plot of 5100 candidate SyncRel designs with four layers computed by the CE-FEA method.

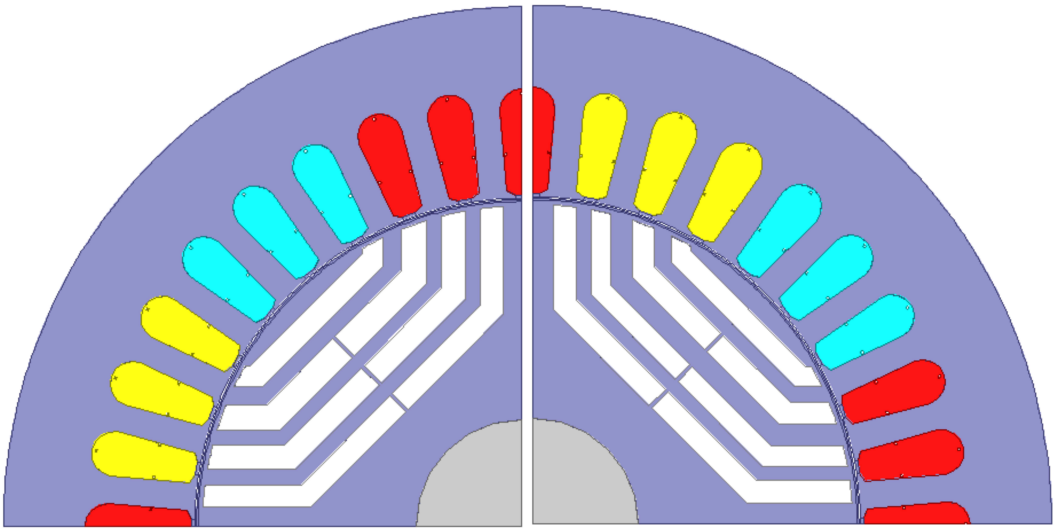

(a) Design 2103

(b) Design 4313

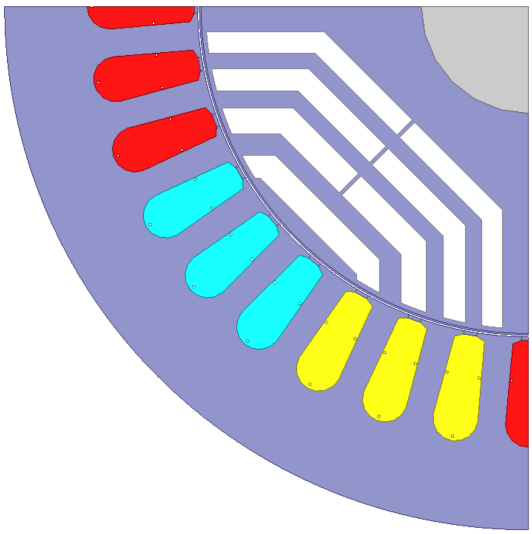

(c) Design 2342

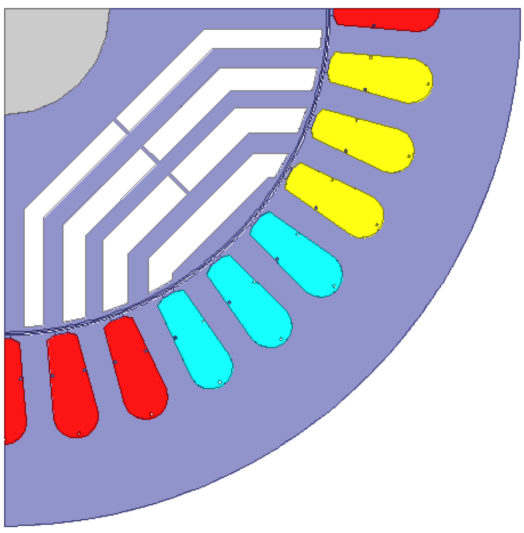

(d) Design 441

Figure 4.30: Cross-sections of four designs marked in Figure 4.29 with high power factors and high badness.

4.2.7 Performance comparison for selected candidate designs

Shown in Fig 4.31 are the rotor cross-section comparison for designs 4863, 1561, 2165 and 3092, and the corresponding performances are provided in Table 4.4. For the motor drive supply system, the dc bus voltage is approximately 250V, which is used to limit the number of turns in the stator winding. The phase induced voltages with reasonable number of turns should not exceed the dc bus voltage of 250V to prevent the motor drive from the over-modulation operation. Thus, the four candidate designs, Design 4863, 1561, 2165 and 3092 provided in Table 4.4, employ a different number of turns per coil in the stator winding [29]. For instance, in the optimization procedure, the number of turns in the stator winding is fixed at 1 turn per coil and the induced voltage of the Design 4863 is 11.9V for one turn winding. In order to meet the dc bus voltage limitation, the final number of turns is 250V/(11.9V/Turn)≈ 21Turns. The total current supplied to the stator winding could be expressed as:

$$I_{rms} = J_{rms} A_{slot} S_{fill} / N_{Turns} \ , \tag{4.9}$$

where the slot fill factor S_{fill}, slot area A_{slot} and current density J_{rms} are constant for all of the DE designs, which leads to that the total current supply for the stator winding is proportional to the number of turns N_{Turns}. Thus the number of turns per coil will not effect the power factor and the efficiency. This conclusion is supported by the first and second sections of Table 4.4.

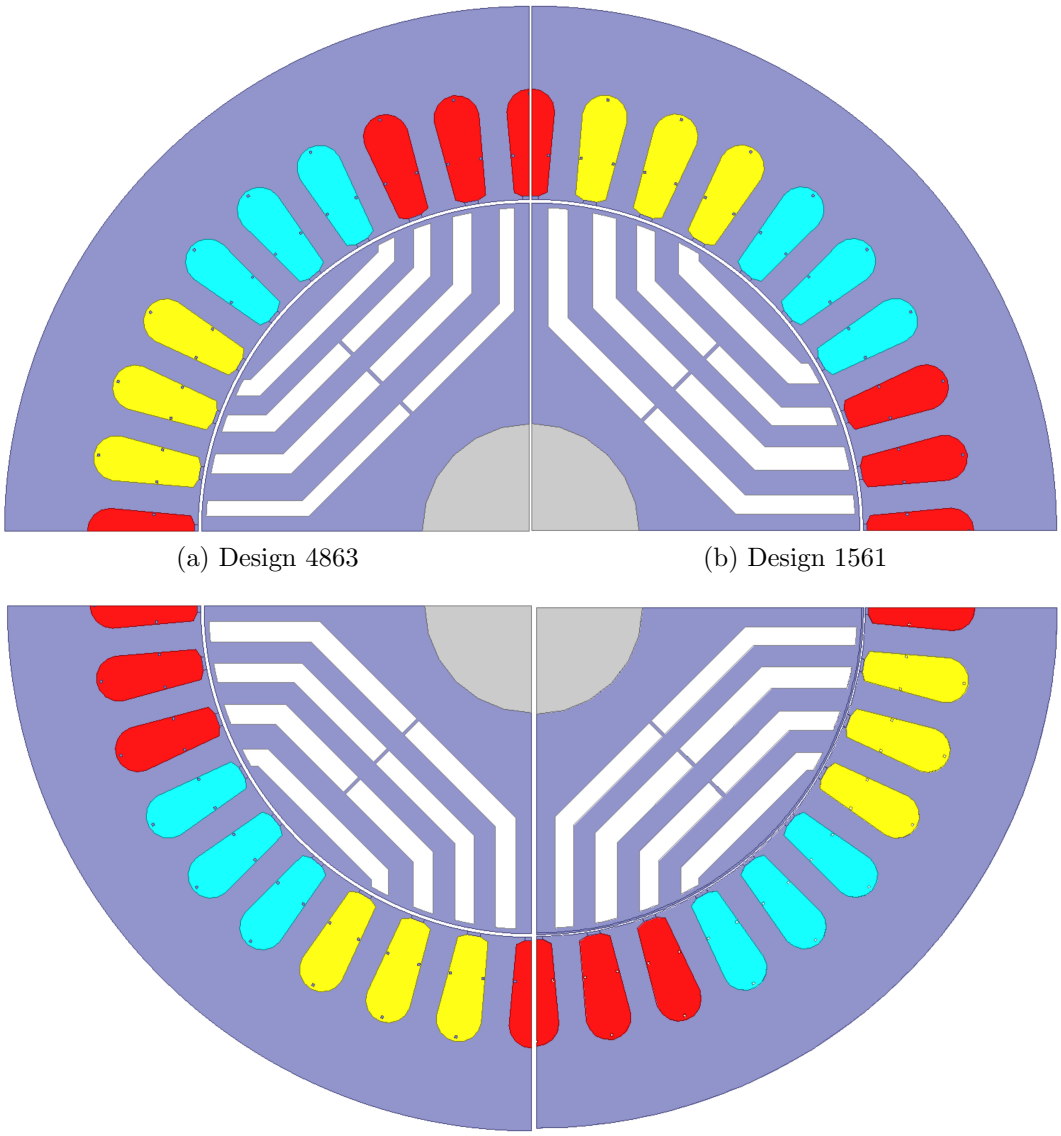

(a) Design 4863 (b) Design 1561

(c) Design 2165 (d) Design 3092

Figure 4.31: Cross-sections of four candidate designs.

Table 4.4: Performance comparison of the optimum designs obtained by there sets of optimization: A is the optimization to minimize the torque ripple and badness, B is the optimization to maximize the power factor and minimize the badness, C is the optimization to maximize the power factor, minimize the badness and torque ripple, and D is the optimization to maximize the power factor only.

Opt. Type	Design ID	Badness $[\frac{\sqrt{W_L}}{Nm}]$	Power Factor [-]	Torque Ripple [%]	Torque [Nm]	Torque Angle [Deg]	EM Power [W]	EM Eff. [%]	Turns* [-]	Current* [A]	Induced Voltage* [V]
Performance at maximum output electromagnetic power											
A	4863	0.58	0.714	9.2	40.0	57.5	7320.8	93.2	21	15.0	245.7
B	1561	0.57	0.726	12.7	40.2	57.5	7372.1	93.3	21	15.0	245.7
C	2165	0.57	0.722	10.1	40.2	57.5	7368.3	93.3	21	15.0	245.7
D	3092	0.57	0.724	12.3	40.1	57.5	7356.5	93.3	21	15.0	243.6
Performance at maximum output electromagnetic power with 21 turns (no scaling)											
A	4863	0.55	0.726	10.7	40.2	57.5	7417.0	93.9	21	15.0	203.5
B	1561	0.55	0.733	12.4	40.1	57.5	7409.0	93.9	21	15.0	201.3
C	2165	0.55	0.728	10.5	40.1	57.5	7393.2	93.9	21	15.0	202.4
D	3096	0.55	0.729	13.0	40.0	57.5	7377.1	93.9	21	15.0	201.7
Performance at maximum power factor with 21 turns (no scaling)											
A	4863	0.66	0.786	12.7	30.7	70.0	5701.3	93.2	21	15.0	146.0
B	1561	0.67	0.791	11.9	29.9	70.0	5558.3	93.2	21	15.0	141.5
C	2165	0.67	0.787	12.5	30.1	70.0	5593.7	93.2	21	15.0	143.1
D	3092	0.67	0.786	12.6	30.1	70.0	5576.4	93.1	21	15.0	142.9
Performance at maximum power factor											
A	4863	0.64	0.761	11.9	33.6	67.5	6192.8	93.0	26	12.1	241.8
B	1561	0.64	0.770	13.0	33.2	67.5	6125.9	93.1	27	11.6	245.7
C	2165	0.60	0.767	12.4	33.4	67.5	6161.3	93.1	27	11.6	248.4
D	3092	0.60	0.765	15.2	36.2	65.0	6659.0	93.3	25	12.6	247.5

* Number of turns, input current and phase induced voltage scaled according to induced voltage with one turn winding

4.2.8 Problem E - Comparison for three barriers and four barriers topologies

In order to investigate the impact of the number of flux-barriers on the performance of SyncRel machine with emphasis on the power factor and torque ripple, another two sets of optimization were performed for the SyncRel machines with three barriers. The optimization for four and three barriers are compared in this section.

Optimization for minimizing torque ripple and badness

Figure 4.33 through Figure 4.35 compared the optimization results with minimizing the badness and torque ripple. From Figure 4.32 and Figure 4.33, one can observe that the SyncRel machines with four barriers could obtain slightly lower torque ripple and badness. From Figure 4.35, another observation is that machines with four barriers could ensure higher power factors.

Optimization for minimizing badness and maximizing power factor

Figure 4.37 through Figure 4.39 compared the optimization results with minimizing the badness and maximizing power factor. From Figure 4.36 and Figure 4.37, the SyncRel machines with four barriers could obtain slightly higher power factor. Observation from Figure 4.35 is that machines with four barriers could ensure lower torque ripple.

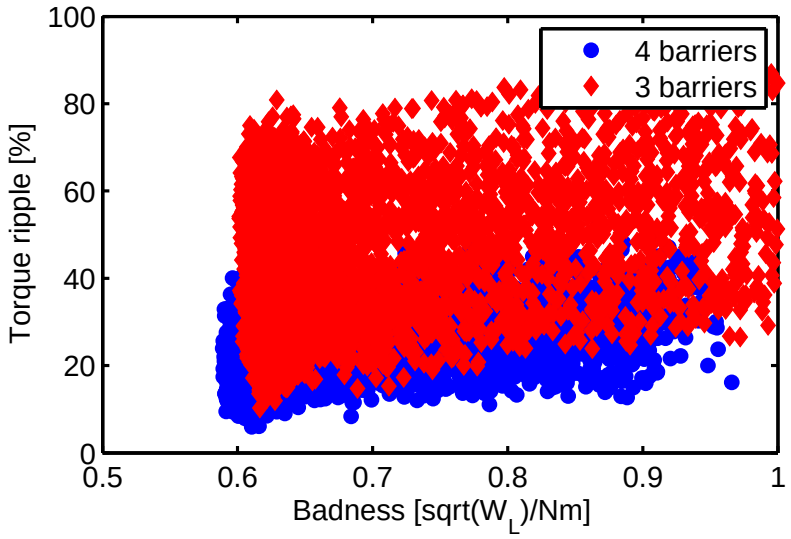

Figure 4.32: Problem E - DE results for the SyncRel machine with four barriers and three barriers (obtained from optimization with torque ripple and badness as two objectives, power factor as constraints).

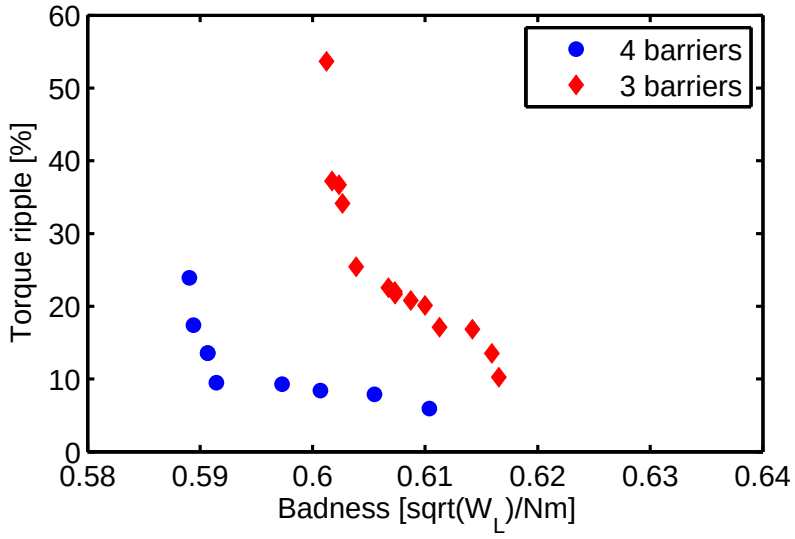

Figure 4.33: Problem E - Optimal Pareto-fronts corresponding to Figure 4.32 on zoomed scales (obtained from optimization with torque ripple and badness as two objectives, power factor as the constraints).

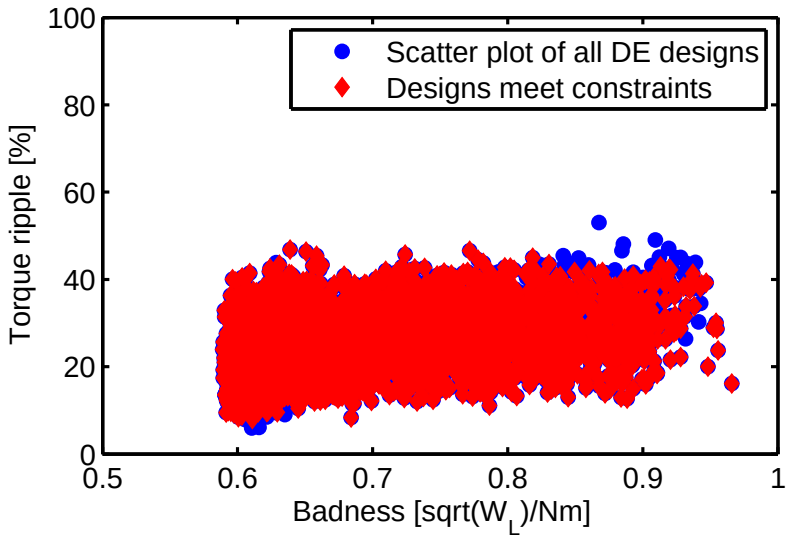

(a) 4 barriers

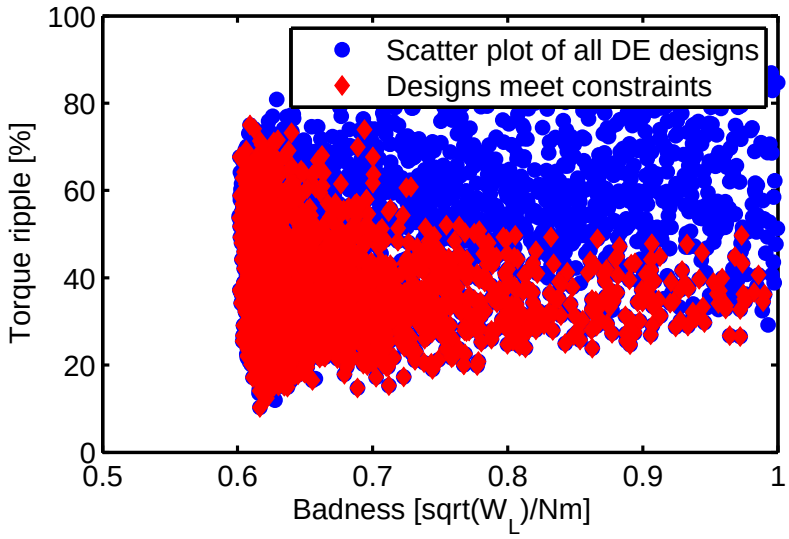

(b) 3 barriers

Figure 4.34: Problem E - Scatter plot of all candidate designs and the designs meet the constraints (minimum power factor 0.7).

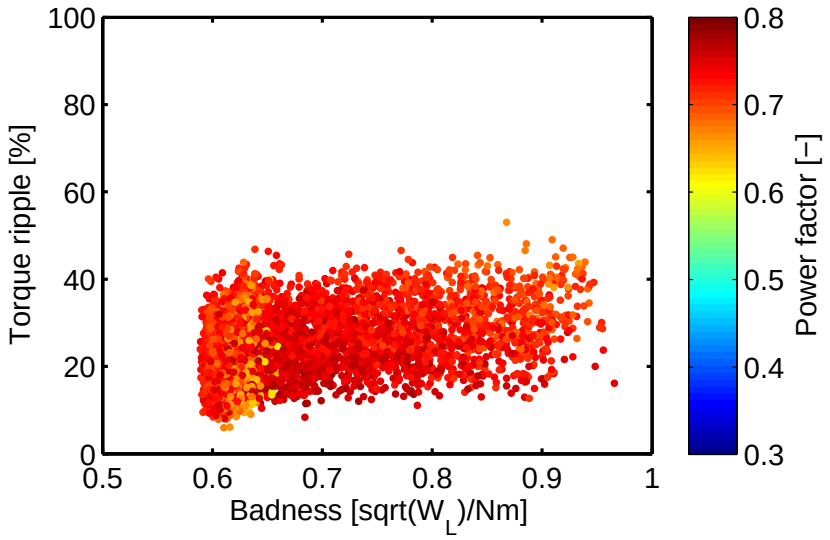

(a) 4 barriers

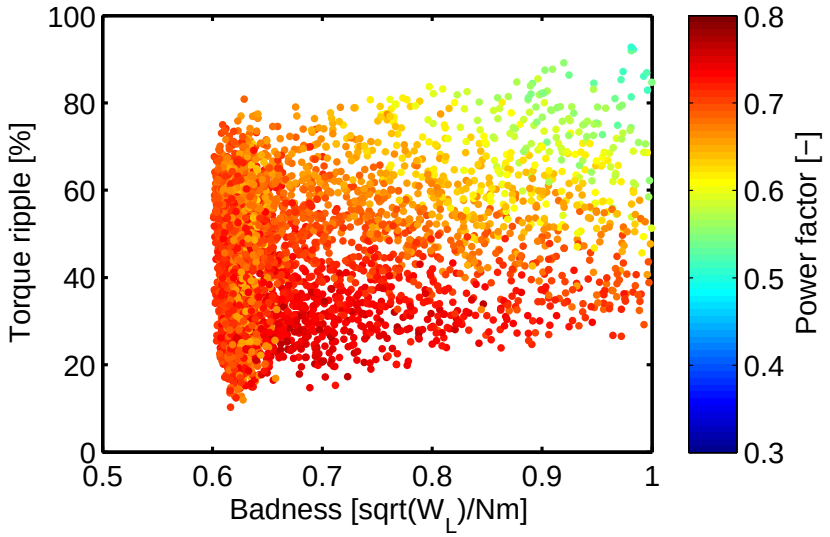

(b) 3 barriers

Figure 4.35: Problem E - Scatter plot for the SyncRel machine with 4 and 3 rotor barriers (obtained from optimization with torque ripple and badness as two objectives, power factor as the constraints).

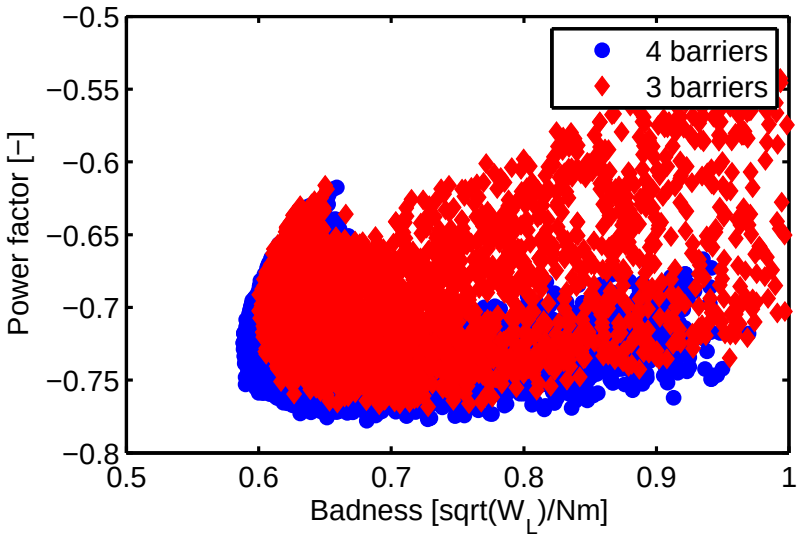

Figure 4.36: Problem E - DE results for the SyncRel machine with four barriers and three barriers (obtained from optimization with power factor and badness as two objectives, torque ripple as the constraints).

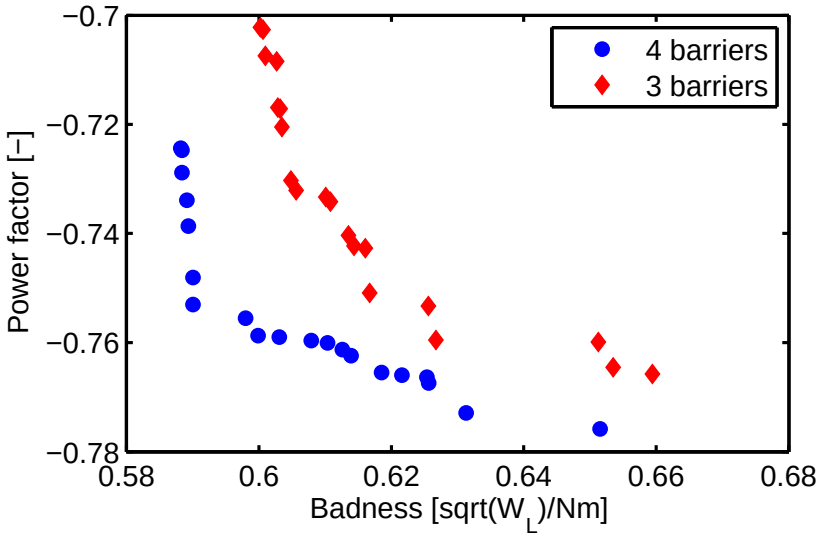

Figure 4.37: Problem E - Optimal Pareto-fronts corresponding to Figure 4.36 on zoomed scales (obtained from optimization with power factor and badness as two objectives, torque ripple as the constraints).

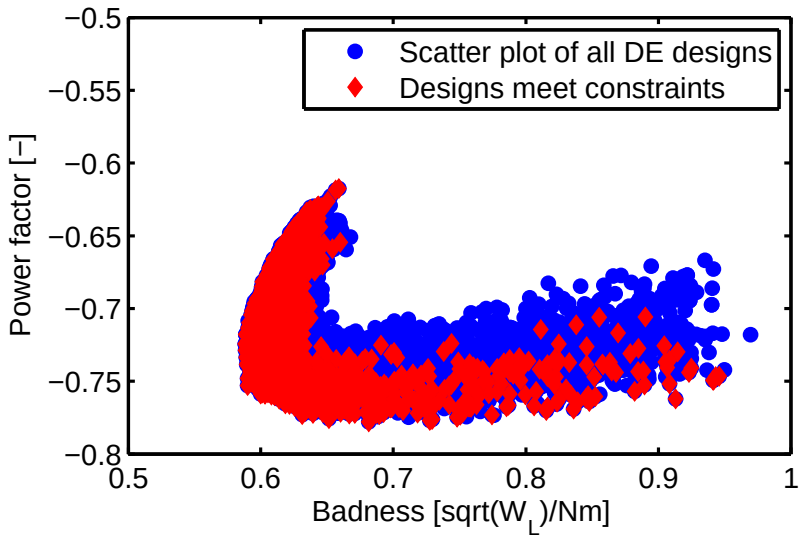

(a) 4 barriers

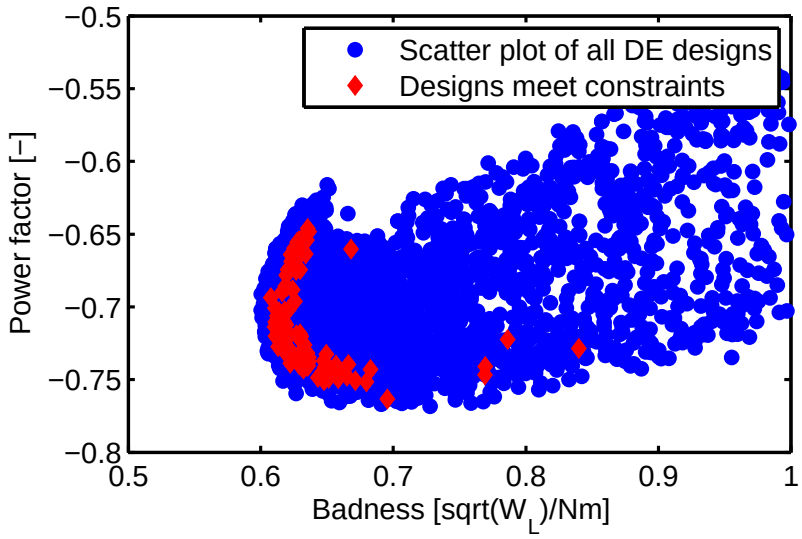

(b) 3 barriers

Figure 4.38: Problem E - Scatter plot of all candidate designs and the designs meet the constraints (maximum torque ripple 20%).

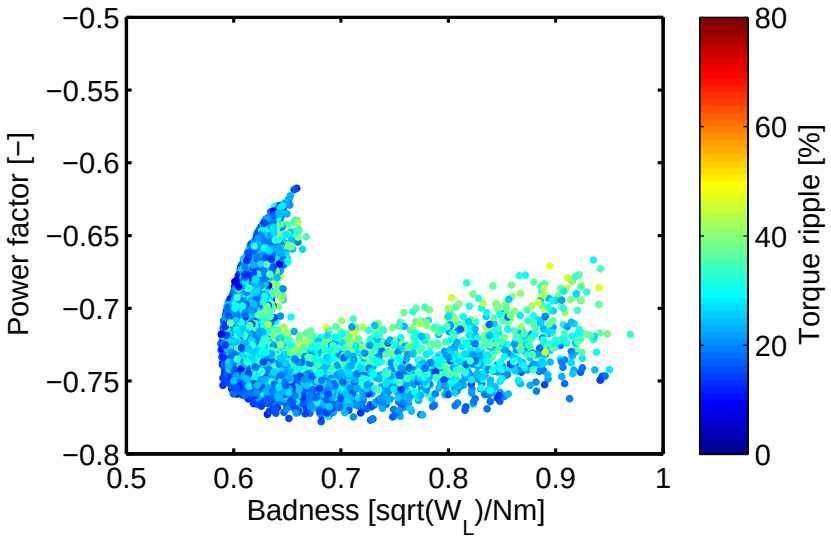

(a) 4 barriers

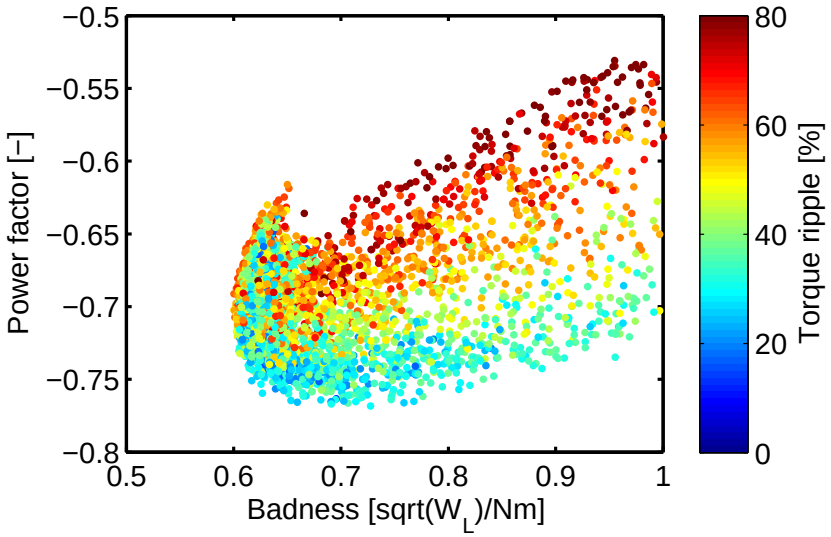

(b) 3 barriers

Figure 4.39: Problem E - Scatter plot for the SyncRel machine with four and three rotor barriers (obtained from optimization with power factor and badness as two objectives, torque ripple as constraints).

4.3 Experimental Validation

A conventional SyncRel machine rotor prototype has been built, as shown in Figure 4.40. The steady-state performance of the prototype was simulated by TS-FEA with two different solvers (ANSYS Maxwell and Motor Design/Motor-CAD) and by CE-FEA, which was implemented through scripting using ANSYS Maxwell as the computational engine. The FEA results are in good agreement, and it should also be noted that CE-FEA is one order of magnitude faster.

The prototype was tested on an active dyno set-up with a computer data acquisition system. A comprehensive on-load test for constant speed of 1,500rpm and current angle from 45° to 70° in increments of 2.5° was performed (see Table 4.5). Other tests, which are not included here, were are also performed.

In Table 4.5, I_{PA} is the current phase angle, V_{ave} is the average line-to-line voltage, V_{ph} is the phase induced voltage, and I_{ave} is the average value of the phase current. The power factor is estimated as:

$$PF = \frac{P_{in}}{S} = \frac{2\pi n}{60} \cdot \frac{T_{EM}}{3V_{ph}I_{ave}} \ , \tag{4.10}$$

where S is the apparent power, and T_{EM} is the electromagnetic torque. The shaft torque is denoted by T_{sh}, and P_{in} and P_{out} are the input and output power in watts, respectively, W_{Cu} is the copper loss, W_{wf} is the windage and friction loss, and W_{Fe}

is the total core loss. The electromagnetic power which is calculated as:

$$P_{EM} = \frac{2\pi n T_{EM}}{60} \ , \tag{4.11}$$

where n is the rotational speed in rpm. The phase displacement (φ) is measured between voltage and current, and Disp PF is the power factor calculated by the fundamental phase displacement:

$$Disp\ PF = \cos(\varphi) \ . \tag{4.12}$$

In the same table, torque ripple [%] is denoted by T_r.

The separation of losses, considered for copper losses, W_{Cu}, only a component due to the DC resistance at a reference winding temperature of 20°C, and a typical value for this motor frame and construction for the windage and friction losses, W_{wf}. All other losses were attributed to core losses, W_{Fe}.

At relatively high values of the torque angle, the computed and the measured results are in satisfactory agreement. Differences are noted for the lower values of the torque angle, for which both the d and q axis current components are significant, and the saturation, including any cross-saturation effects, is high as shown in Table 4.6 and Figs. 4.41, 4.42, and 4.43. Because the FE computed results, which were produced with different solvers and techniques, are in satisfactory agreement, a main reason for the deviation with respect to measurements is identified as the possible variation of the laminated steel B-H magnetization characteristics. The simulation

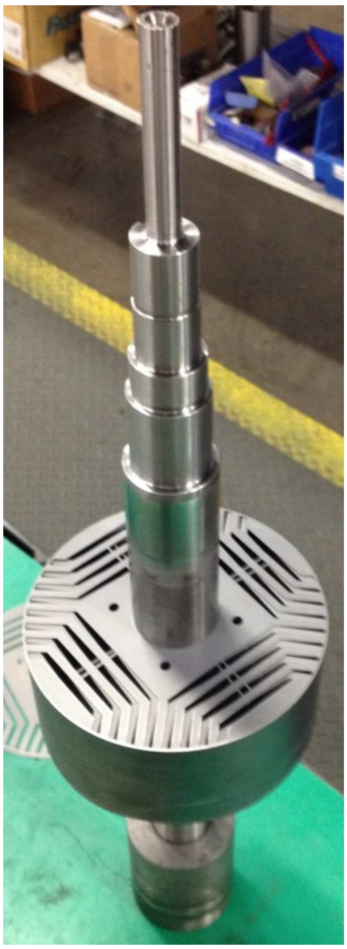

Figure 4.40: RBC SyncRel rotor prototype.

used a material model based on catalog values, while the actual characteristics of the material employed in the prototype were not measured.

Table 4.5: Tested and calculated performance of the conventional SyncRel machine running at 1,500rpm.

	I_{PA}	V_{ave}	V_{ph}	I_{ave}	PF	T_{sh}	P_{in}	P_{out}	Eff	W_{Cu}	W_{wf}	W_{Fe}	P_{EM}	T_{EM}	φ	Disp PF	T_r
	[deg]	[V]	[V]	[A]	[-]	[Nm]	[W]	[W]	[%]	[W]	[W]	[W]	[W]	[Nm]	[Deg]	[-]	[%]
Test	45.0	441.3	254.8	15.3	0.470	30.4	5480.5	4782.7	87.3	331.6	91.0	275.2	5148.9	32.8	56.7	0.549	N/A
CEFEA	**45.0**	**437.5**	**252.6**	**15.3**	**0.592**	**39.8**	**6861.7**	**6245.6**	**91.0**	**340.0**	**91.0**	**185.1**	**6521.7**	**41.5**	**53.4**	**0.597**	**23.2**
Trans	***45.0***	***415.5***	***239.9***	***15.3***	***0.628***	***40.4***	***6919.1***	***6352.6***	***91.8***	***340.0***	***91.0***	***135.5***	***6579.1***	***41.9***	***53.7***	***0.592***	***26.2***
MotorCAD	*45.0*	*437.9*	*253.5*	*15.3*	*0.615*	*41.9*	*7159.2*	*6578.4*	*91.9*	*340.4*	*91.0*	*149.4*	*6818.8*	*43.4*	*51.9*	*0.617*	N/A
Test	47.5	436.4	251.9	15.3	0.497	32.3	5740.1	5069.8	88.3	331.6	91.0	247.7	5408.5	34.4	55.1	0.572	N/A
CEFEA	**47.5**	**352.7**	**249.4**	**15.3**	**0.618**	**41.1**	**7078.5**	**6463.4**	**91.3**	**340.0**	**91.0**	**184.1**	**6738.5**	**42.9**	**51.5**	**0.623**	**23.2**
Trans	***47.5***	***425.0***	***245.4***	***15.3***	***0.634***	***41.8***	***7138.3***	***6573.4***	***92.1***	***340.0***	***91.0***	***133.8***	***6798.3***	***43.3***	***51.8***	***0.619***	***26.5***
MotorCAD	*47.5*	*432.3*	*250.3*	*15.3*	*0.641*	*43.2*	*7365.0*	*6787.2*	*92.2*	*340.4*	*91.0*	*146.4*	*7024.6*	*44.7*	*50.0*	*0.643*	N/A
Test	50.0	430.9	248.8	15.3	0.523	33.8	5956.4	5314.7	89.2	331.6	91.0	219.1	5624.8	35.8	53.6	0.593	N/A
CEFEA	**50.0**	**425.7**	**245.8**	**15.3**	**0.644**	**42.4**	**7270.7**	**6656.3**	**91.5**	**340.0**	**91.0**	**183.4**	**6930.7**	**44.1**	**49.6**	**0.648**	**23.5**
Trans	***50.0***	***419.2***	***242.0***	***15.3***	***0.660***	***43.1***	***7326.4***	***6763.2***	***92.3***	***340.0***	***91.0***	***132.2***	***6986.4***	***44.5***	***49.9***	***0.644***	***27.2***
MotorCAD	*50.0*	*426.0*	*246.7*	*15.3*	*0.666*	*44.3*	*7536.2*	*6963.8*	*92.4*	*340.4*	*91.0*	*141.0*	*7195.8*	*45.8*	*48.1*	*0.668*	N/A
Test	52.5	424.9	245.3	15.3	0.547	35.2	6147.0	5531.3	90.0	331.6	91.0	193.1	5815.4	37.0	52.1	0.614	N/A
CEFEA	**52.5**	**419.0**	**241.9**	**15.3**	**0.669**	**43.4**	**7424.5**	**6811.1**	**91.7**	**340.0**	**91.0**	**182.4**	**7084.5**	**45.1**	**47.8**	**0.672**	**23.8**
Trans	***52.5***	***412.7***	***238.2***	***15.3***	***0.684***	***44.0***	***7479.1***	***6917.6***	***92.5***	***340.0***	***91.0***	***130.5***	***7139.1***	***45.4***	***48.1***	***0.668***	***28.3***
MotorCAD	*52.5*	*418.8*	*242.5*	*15.3*	*0.689*	*45.2*	*7666.6*	*7096.8*	*92.6*	*340.4*	*91.0*	*138.4*	*7326.2*	*46.6*	*46.3*	*0.691*	*14.2*
Test	55.0	418.2	241.5	15.3	0.570	36.4	6307.4	5717.4	90.6	331.6	91.0	167.4	5975.8	38.0	50.7	0.633	N/A
CEFEA	**55.0**	**411.0**	**237.3**	**15.3**	**0.691**	**44.1**	**7531.8**	**6920.4**	**91.9**	**340.0**	**91.0**	**180.4**	**7191.8**	**45.8**	**46.0**	**0.694**	**25.6**
Trans	***55.0***	***405.1***	***233.9***	***15.3***	***0.707***	***44.7***	***7588.8***	***7028.1***	***92.6***	***340.0***	***91.0***	***129.6***	***7248.8***	***46.1***	***46.3***	***0.690***	***29.5***
MotorCAD	*55.0*	*410.3*	*237.7*	*15.3*	*0.710*	*45.7*	*7749.8*	*7182.4*	*92.7*	*340.4*	*91.0*	*136.0*	*7409.4*	*47.2*	*44.5*	*0.713*	N/A
Test	57.5	410.7	237.1	15.3	0.592	37.3	6432.8	5866.7	91.2	331.6	91.0	143.5	6101.2	38.8	49.4	0.651	N/A
CEFEA	**57.5**	**402.2**	**232.2**	**15.3**	**0.713**	**44.5**	**7593.9**	**6985.4**	**92.0**	**340.0**	**91.0**	**177.5**	**7253.9**	**46.2**	**44.3**	**0.715**	**27.4**
Trans	***57.5***	***396.3***	***228.8***	***15.3***	***0.728***	***45.1***	***7646.7***	***7088.4***	***92.7***	***340.0***	***91.0***	***127.3***	***7306.7***	***46.5***	***44.6***	***0.712***	***30.8***
MotorCAD	*57.5*	*400.2*	*231.8*	*15.3*	*0.731*	*45.9*	*7775.0*	*7210.8*	*92.7*	*340.4*	*91.0*	*132.8*	*7434.6*	*47.3*	*42.9*	*0.733*	N/A
Test	60.0	402.2	232.2	15.3	0.613	38.1	6518.9	5977.3	91.7	331.6	91.0	119.1	6187.3	39.4	48.3	0.665	N/A
CEFEA	**60.0**	**391.4**	**226.0**	**15.3**	**0.731**	**44.4**	**7584.6**	**6980.3**	**92.0**	**340.0**	**91.0**	**173.3**	**7244.6**	**46.1**	**42.9**	**0.733**	**29.3**
Trans	***60.0***	***385.9***	***222.8***	***15.3***	***0.747***	***45.1***	***7643.4***	***7086.8***	***92.7***	***340.0***	***91.0***	***125.6***	***7303.4***	***46.5***	***43.0***	***0.731***	***32.6***
MotorCAD	*60.0*	*387.8*	*224.7*	*15.3*	*0.749*	*45.6*	*7720.0*	*7169.4*	*92.9*	*340.4*	*91.0*	*119.2*	*7379.6*	*47.0*	*41.3*	*0.751*	N/A
Test	62.5	392.6	226.7	15.3	0.632	38.4	6561.2	6038.6	92.0	331.6	91.0	100.0	6229.6	39.7	47.4	0.677	N/A
CEFEA	**62.5**	**378.6**	**218.6**	**15.3**	**0.746**	**43.8**	**7484.0**	**6886.4**	**92.0**	**340.0**	**91.0**	**166.7**	**7144.0**	**45.5**	**41.7**	**0.746**	**31.1**
Trans	***62.5***	***372.7***	***215.2***	***15.3***	***0.764***	***44.5***	***7542.4***	***6987.9***	***92.6***	***340.0***	***91.0***	***123.5***	***7202.4***	***45.9***	***41.6***	***0.748***	***34.0***
MotorCAD	*62.5*	*372.2*	*215.7*	*15.3*	*0.764*	*44.7*	*7561.4*	*7020.2*	*92.8*	*340.4*	*91.0*	*109.8*	*7221.0*	*46.0*	*40.0*	*0.767*	N/A
Test	65.0	381.6	220.3	15.3	0.649	38.5	6550.3	6045.0	92.3	331.6	91.0	82.7	6218.7	39.6	46.7	0.686	N/A
CEFEA	**65.0**	**362.7**	**209.4**	**15.3**	**0.754**	**42.4**	**7250.9**	**6664.2**	**91.9**	**340.0**	**91.0**	**155.7**	**6910.9**	**44.0**	**41.1**	**0.754**	**32.2**
Trans	***65.0***	***356.3***	***205.7***	***15.3***	***0.776***	***43.1***	***7324.1***	***6773.4***	***92.5***	***340.0***	***91.0***	***119.7***	***6984.1***	***44.5***	***40.4***	***0.761***	***35.2***
MotorCAD	*65.0*	*352.2*	*204.1*	*15.3*	*0.775*	*42.8*	*7262.9*	*6727.4*	*92.6*	*340.4*	*91.0*	*104.1*	*6922.5*	*44.1*	*38.9*	*0.778*	*14.5*
Test	67.5	368.8	212.9	15.3	0.664	38.1	6474.9	5986.0	92.4	331.6	91.0	66.3	6143.3	39.1	46.4	0.690	N/A
CEFEA	**67.5**	**342.6**	**197.8**	**15.3**	**0.754**	**39.9**	**6847.0**	**6274.8**	**91.6**	**340.0**	**91.0**	**141.2**	**6507.0**	**41.4**	**41.0**	**0.755**	**32.8**
Trans	***67.5***	***334.8***	***193.3***	***15.3***	***0.781***	***40.7***	***6930.1***	***6385.4***	***92.1***	***340.0***	***91.0***	***113.7***	***6590.1***	***42.0***	***39.7***	***0.770***	***35.4***
MotorCAD	*67.5*	*327.4*	*189.8*	*15.3*	*0.782*	*40.0*	*6808.9*	*6284.1*	*92.3*	*340.4*	*91.0*	*93.4*	*6468.5*	*41.2*	*38.3*	*0.785*	N/A
Test	70.0	353.9	204.3	15.3	0.676	37.2	6325.0	5848.4	92.5	331.6	91.0	54.0	5993.4	38.2	46.6	0.687	N/A
CEFEA	**70.0**	**317.0**	**183.0**	**15.3**	**0.749**	**36.5**	**6290.2**	**5733.1**	**91.1**	**340.0**	**91.0**	**126.0**	**5950.2**	**37.9**	**41.5**	**0.749**	**34.2**
Trans	***70.0***	***309.0***	***178.4***	***15.3***	***0.780***	***37.2***	***6383.7***	***5847.9***	***91.6***	***340.0***	***91.0***	***104.7***	***6043.7***	***38.5***	***39.5***	***0.771***	***35.9***
MotorCAD	*70.0*	*299.2*	*173.6*	*15.3*	*0.781*	*36.3*	*6219.9*	*5709.2*	*91.8*	*340.4*	*91.0*	*79.3*	*5879.5*	*37.4*	*38.3*	*0.784*	N/A

Table 4.6: Flux density in the stator teeth and yoke various with current phase angle estimated by CE-FEA and TS-FEA

	Current angle	BT1	BT2	BT3	BY1	BY2	BY3
	[deg]	[T]	[T]	[T]	[T]	[T]	[T]
CEFEA	**45.0**	**1.77**	**1.79**	**1.87**	**1.86**	**1.85**	**1.81**
Trans	***45.0***	***1.77***	***1.78***	***1.87***	***1.85***	***1.84***	***1.81***
CEFEA	**47.5**	**1.76**	**1.77**	**1.86**	**1.85**	**1.84**	**1.79**
Trans	***47.5***	***1.75***	***1.76***	***1.85***	***1.83***	***1.83***	***1.79***
CEFEA	**50.0**	**1.74**	**1.75**	**1.84**	**1.83**	**1.82**	**1.77**
Trans	***50.0***	***1.73***	***1.73***	***1.83***	***1.81***	***1.81***	***1.77***
CEFEA	**52.5**	**1.71**	**1.73**	**1.82**	**1.80**	**1.79**	**1.74**
Trans	***52.5***	***1.70***	***1.71***	***1.82***	***1.79***	***1.78***	***1.75***
CEFEA	**55.0**	**1.69**	**1.71**	**1.79**	**1.78**	**1.77**	**1.71**
Trans	**55.0**	***1.67***	***1.69***	***1.79***	***1.76***	***1.76***	***1.72***
CEFEA	**57.5**	**1.66**	**1.68**	**1.77**	**1.75**	**1.73**	**1.68**
Trans	**57.5**	***1.66***	***1.68***	***1.77***	***1.74***	***1.73***	***1.69***
CEFEA	**60.0**	**1.63**	**1.66**	**1.75**	**1.71**	**1.70**	**1.63**
Trans	**60.0**	***1.63***	***1.65***	***1.74***	***1.70***	***1.69***	***1.65***
CEFEA	**62.5**	**1.59**	**1.63**	**1.72**	**1.66**	**1.65**	**1.57**
Trans	**62.5**	***1.59***	***1.61***	***1.71***	***1.65***	***1.64***	***1.60***
CEFEA	**65.0**	**1.52**	**1.58**	**1.68**	**1.59**	**1.58**	**1.49**
Trans	**65.0**	***1.53***	***1.57***	***1.67***	***1.59***	***1.57***	***1.52***
CEFEA	**67.5**	**1.41**	**1.49**	**1.63**	**1.51**	**1.49**	**1.38**
Trans	**67.5**	***1.44***	***1.49***	***1.62***	***1.50***	***1.48***	***1.42***
CEFEA	**70.0**	**1.28**	**1.37**	**1.56**	**1.40**	**1.37**	**1.26**
Trans	**70.0**	***1.32***	***1.37***	***1.56***	***1.39***	***1.37***	***1.29***

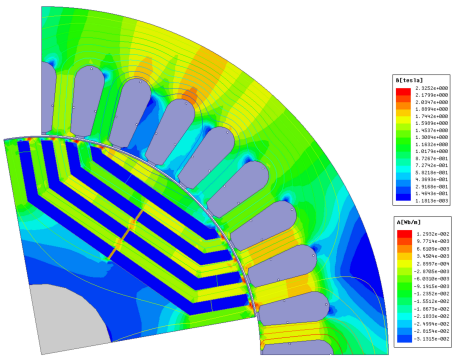

Figure 4.41: Flux plot of the SyncRel machine running at 45deg current phase angle.

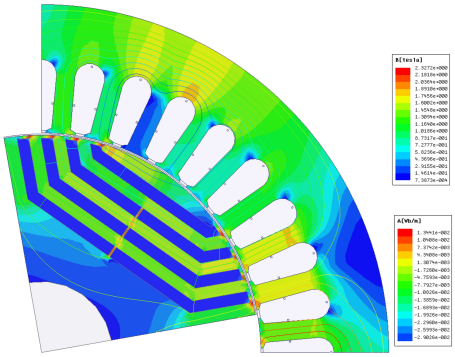

Figure 4.42: Flux plot of the SyncRel machine running at 57.5deg current phase angle.

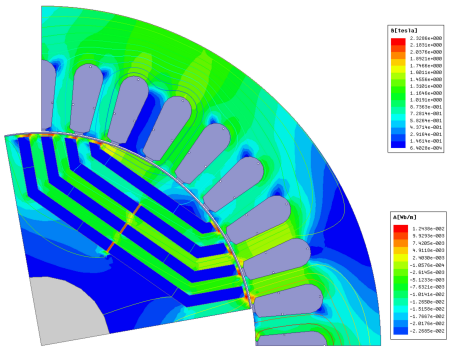

Figure 4.43: Flux plot of the SyncRel machine running at 70deg current phase angle.

CHAPTER 5

Conclusions, Contributions and Future Work

5.1 Conclusions

The focus of the work for this thesis is represented by the analysis and automated design optimization of electronically controlled synchronous (PM and SyncRel) machines. In Chapter 1, the research background for the relevant topics was reviewed, including main different topologies of PM and SyncRel machines, and specific optimal design optimization algorithms.

Elements of analysis have been reviewed in Chapter 2, prior to introducing a new method that comprises an ultrafast nonlinear electromagnetic FE technique for estimating the sine-wave current regulated performance of synchronous machines, including induced voltage waveforms, average and ripple torque, inductances, and power losses. Unlike the time-stepping FEA (TS-FEA) method, which utilizes hundreds of FE solutions to solve the electromagnetic field analysis, the ultrafast method, which exploits the slot-pitch symmetry of the stator magnetic circuit and the periodicity of the electromagnetic field, only uses a minimum number of magnetostatic FE solutions to substantially reduce the computational effort by up to two orders of magnitude while achieving satisfactory accuracy. The electromagnetic field analysis was iteratively coupled in a non-conventional manner with an equivalent network for

thermal and air-flow analysis. Examples included numerical studies and experimental validation.

In Chapter 3, the fundamental concepts and the computer implementation of differential evolution algorithms for solving multi-objective optimization problems have been discussed. The requirements and the means for building robust and flexible parametric models for the large scale automated design optimization were also exemplified. In order to avoid the overlapping of different geometrical subdomains, main geometric parameters were ratio parameterized. The steps of the optimization algorithms, the definition of Pareto-fronts, and procedures for selecting the "best compromise" designs have been presented.

In Chapter 4, the optimal design techniques have been applied for the study of an IPM machine with a 36-slot 6-pole V-shape rotor topology and of a SyncRel motor in 36-slot 4-pole configuration with different rotor arrangements. The results confirm some of the design rules known to those skilled in the art, but also provide insights that maybe new even to very experienced engineers. One SyncRel design has been prototyped and successfully tested, providing experimental validation.

5.2 Contributions

The main contributions resulting from the research covered in the thesis are listed in the following.

1. An ultrafast method for multi-physics analysis of electronically controlled synchronous machines of the BLPM and SyncRel type, which substantially reduces the computational effort, while achieving satisfactory accuracy was developed. The technique combines a computationally efficient FEA (CE-FEA) for the electromagnetic field with equivalent thermal and air-flow lumped parameter networks. Based on the observation that the core losses experience a relatively small variation with temperature and load, an innovative step is represented by the introduction of an inner loop iteration that only performs thermal calculations and updates only the copper losses. This approach minimizes the number of iterations for the outer loop, which includes the more time consuming electromagnetic CE-FEA. For the examples studied, as few as two outer loop iterations were required for convergence, recommending the technique as a useful tool suitable for large scale optimization studies that consider thousands of candidate designs. The analysis was validated thorough comparison with other more computationally expensive methods and with experimental results.

2. The coupled analysis technique was implemented using the MATLAB programming language and ActiveX scripting for employing the ANSYS-Maxwell software as an electromagnetic computational engine and the Motor Design-MotorCAD software as a thermal computational engine. Also, parallel processing functions based on a "distributed solve option (DSO)" for multi-core

computer systems, parametric models, and optimization routines for large scale studies have also been implemented.

3. Large scale studies with thousands of candidate designs for BLPM and SyncRel machines have been performed. These included a SyncRel optimization problem with three objectives, power factor, "badness", and torque ripple, which is the first of its kind as indicated by the recent literature review. Also included is a systematic study that confirms the limitations of conventional SyncRel technology in terms of power factor and illustrates the possible improvements with PMaSyncRel technology. A SyncRel prototype has been built and successfully tested.

Two IEEE Conference papers on analysis and optimization have been completed, reviewed, and are accepted for publication, and oral presentation at the ECCE Conference to be held in Pittsburgh in September 2014 [71, 72]. Public presentations on state of the art synchronous reluctance technology and on the computer implementation using the ANSYS and MotorCAD software have already been made at the EMCW Conference in Milwaukee, WI and the ANSYS Convergence Conference in Chicago, IL in May 2014.

5.3 Future work

Future work is recommended in the area of High Performance Computing (HPC). Topics of great interest to the scientific and engineering community include analysis techniques for which the computational time can be reduced linearly with the number of parallel solvers employed, and evolutionary algorithms suitable for set-ups in which the number of available cores for parallel processing exceeds the maxim number of individual recommended per generation.

From a mathematical point of view, the study of other optimization methods that could possibly quicker reach the optimum, especially for electric machine specific problems would be of interest.

From an engineering point of view, the study of alternative design topologies, such as SyncRel with fractional-slot or concentrated stator winding combinations, rotors with combined flux barrier and magnets arrangements, are just some of the timely topics that should be considered for further investigation.

The optimization method could be expanded to incorporate preliminary sensitivity studies in order to determine the influence of the independent variables on the output performance and objectives. In this case, possible advantages, beyond gathering engineering insights into the problem, would be a reduction of the dimensions of the design space and of the computational effort. Furthermore, it would be of interest to investigate if such studies, or other novel mathematical techniques, could be employed

at the end of the optimization and used to provide insights and explanations into what are the design characteristics, i.e. the "pattern" of independent variables, yielding a "good" design.

REFERENCES

[1] D. M. Ionel, "High-efficiency variable-speed electric motor drive technologies for energy savings in the us residential sector," in *Optimization of Electrical and Electronic Equipment (OPTIM), 2010 12th International Conference on*, May 2010, pp. 1403–1414.

[2] D. A. Staton and D. M. Ionel, "Practical aspects in modern design process of electric motors," in *Energy Conversion Congress and Exposition (ECCE), 2011 IEEE*, 2011.

[3] I. Boldea and S. A. Nasar, *Electric Drives*. CRC, 2005.

[4] J. F. Gieras, *Permanent Magnet Motor Technology*. CRC Press, .

[5] N. Bianchi and S. Bolognani, "Design techniques for reducing the cogging torque in surface-mounted pm motors," *IEEE Transactions on Industry Applications*, vol. 38, no. 5, pp. 1259–1265, 2002.

[6] A. EL-Refaie and T. Jahns, "Scalability of surface pm machines with concentrated windings designed to achieve wide speed ranges of constant-power operation," *IEEE Transactions on Energy Conversion*, vol. 21, no. 2, pp. 362–369, 2006.

[7] A. Mitcham, G. Antonopoulos, and J. J. A. Cullen, "Favourable slot and pole number combinations for fault-tolerant pm machines," *IEE Proceedings-Electric Power Applications*, vol. 151, no. 5, pp. 520–525, 2004.

[8] N. Bianchi, S. Bolognani, and M. Pre, "Strategies for the fault-tolerant current

control of a five-phase permanent-magnet motor," *IEEE Transactions on Industry Applications*, vol. 43, no. 4, pp. 960–970, 2007.

[9] N. Bianchi, S. Bolognani, and M. D. Pre, "Impact of stator winding of a five-phase permanent-magnet motor on postfault operations," *IEEE Transactions on Industrial Electronics*, vol. 55, no. 5, pp. 1978–1987, 2008.

[10] A. Vagati, G. Pellegrino, and P. Guglielmi, "Comparison between spm and ipm motor drives for ev application," in *Electrical Machines (ICEM), 2010 XIX International Conference on*, Sept 2010, pp. 1–6.

[11] D. M. Ionel. "IPM Motors: a new solution for high-performance appliances". [Online]. Available: http://www.appliancemagazine.com/print.php?article=2110

[12] Peng Zhang, D. M. Ionel, and N. Demerdash, "Morphing parametric modeling and design optimization of spoke and v-type permanent magnet machines by combined design of experiments and differential evolution algorithms," in *Energy Conversion Congress and Exposition (ECCE), 2013 IEEE*, Sept 2013, pp. 5056–5063.

[13] D. M. Ionel, R. J. Heideman, and R. P. Bartos, "Spoke permanent magnet rotors for electrical machines and methods of manufacturing same," U.S. Patent 7 148 598, Oct. 23, 2003.

[14] G. Pellegrino, F. Cupertino, and C. Gerada, "Barriers shapes and minimum set of rotor parameters in the automated design of synchronous reluctance machines," in *Electric Machines Drives Conference (IEMDC), 2013 IEEE International*, May 2013, pp. 1204–1210.

[15] F. Cupertino, G.-M. Pellegrino, E. Armando, and C. Gerada, "A syr and ipm machine design methodology assisted by optimization algorithms," in *Energy*

Conversion Congress and Exposition (ECCE), 2012 IEEE, Sept 2012, pp. 3686–3691.

[16] K. Wang, Z. Zhu, G. Ombach, M. Koch, S. Zhang, and J. Xu, "Optimal slot/pole and flux-barrier layer number combinations for synchronous reluctance machines," in *Ecological Vehicles and Renewable Energies (EVER), 2013 8th International Conference and Exhibition on*, March 2013, pp. 1–8.

[17] A. Vagati, A. Canova, M. Chiampi, M. Pastorelli, and M. Repetto, "Design refinement of synchronous reluctance motors through finite-element analysis," *Industry Applications, IEEE Transactions on*, vol. 36, no. 4, pp. 1094–1102, Jul 2000.

[18] R. Moghaddam, F. Magnussen, and C. Sadarangani, "A FEM[1] investigation on the synchronous reluctance machine rotor geometry with just one flux barrier as a guide toward the optimal barrier's shape," in *EUROCON 2009, EUROCON '09. IEEE*, May 2009, pp. 663–670.

[19] R. Moghaddam, F. Magnussen and C. Sadarangani, "Theoretical and experimental reevaluation of synchronous reluctance machine," *Industrial Electronics, IEEE Transactions on*, vol. 57, no. 1, pp. 6–13, Jan 2010.

[20] I. Boldea, Z. X. Fu, and S. Nasar, "Performance evaluation of axially-laminated anisotropic (ala) rotor reluctance synchronous motors," in *Industry Applications Society Annual Meeting, 1992., Conference Record of the 1992 IEEE*, Oct 1992, pp. 212–218 vol.1.

[21] A. Vagati, M. Pastorelli, G. Francheschini, and S. Petrache, "Design of low-torque-ripple synchronous reluctance motors," *Industry Applications, IEEE Transactions on*, vol. 34, no. 4, pp. 758–765, Jul 1998.

[22] A. Vagati, A. Fratta, G. Franceschini, and P. Rosso, "Ac motors for high-performance drives: a design-based comparison," *Industry Applications, IEEE Transactions on*, vol. 32, no. 5, pp. 1211–1219, Sep 1996.

[23] N. Bianchi, M. Degano, and E. Fornasiero, "Sensitivity analysis of torque ripple reduction of synchronous reluctance and interior pm motors," in *Energy Conversion Congress and Exposition (ECCE), 2013 IEEE*, Sept 2013, pp. 1842–1849.

[24] M. Ferrari, N. Bianchi, and E. Fornasiero, "Rotor saturation impact in synchronous reluctance and pm assisted reluctance motors," in *Energy Conversion Congress and Exposition (ECCE), 2013 IEEE*, Sept 2013, pp. 1235–1242.

[25] J. Baek, M. Rahimian, and H. Toliyat, "Optimal design of pm assisted synchronous reluctance generators using lumped parameter model and differential evolution strategy," in *Energy Conversion Congress and Exposition, 2009. ECCE 2009. IEEE*, Sept 2009, pp. 2453–2459.

[26] M. Kamper, "Reluctance synchronous machine drives a viable alternative ?" in *IEEE Joint IAS/PELS/IES Chapter Meeting*, July 2013.

[27] G. Sizov, Peng Zhang, D. M. Ionel, N. Demerdash, and M. Rosu, "Automated multi-objective design optimization of pm ac machines using computationally efficient fea and differential evolution," *Industry Applications, IEEE Transactions on*, vol. 49, no. 5, pp. 2086–2096, Sept 2013.

[28] G. Sizov, Peng Zhang, D. M. Ionel, N. A. O. Demerdash, and M. Rosu, "Automated bi-objective design optimization of multi-mw direct-drive pm machines using ce-fea and differential evolution," in *Energy Conversion Congress and Exposition (ECCE), 2011 IEEE*, Sept 2011, pp. 3672–3678.

[29] Peng Zhang, G. Sizov, D. M. Ionel, and N. Demerdash, "Design optimization of spoke-type ferrite magnet machines by combined design of experiments

and differential evolution algorithms," in *Electric Machines Drives Conference (IEMDC), 2013 IEEE International*, May 2013, pp. 892–898.

[30] Peng Zhang, G. Sizov, J. He, D. M. Ionel, and N. Demerdash, "Calculation of magnet losses in concentrated-winding permanent magnet synchronous machines using a computationally efficient - finite element method," in *Energy Conversion Congress and Exposition (ECCE), 2012 IEEE*, Sept 2012, pp. 3363–3370.

[31] S.-I. Kim, J.-P. Hong, Y.-K. Kim, H. Nam, and H.-I. Cho, "Optimal design of slotless-type pmlsm considering multiple responses by response surface methodology," *IEEE Transactions on Magnetics*, vol. 42, no. 4, pp. 1219–1222, 2006.

[32] Peng Zhang, S.-O. Kwon, L. Fang, and J. pyo Hong, "The design and analysis of a high efficiency permanent magnet reluctance motor," in *International Conference on Electrical Machines and Systems (ICEMS)*, 2006, pp. 1–7.

[33] Y. Duan and D. M. Ionel, "A review of recent developments in electrical machine design optimization methods with a permanent-magnet synchronous motor benchmark study," *Industry Applications, IEEE Transactions on*, vol. 49, no. 3, pp. 1268–1275, May 2013.

[34] M. Mitchell, *An Introduction to Genetic Algorithms, 3rd ed.* MIT Press, 1998.

[35] Y. Duan, R. Harley, and T. Habetler, "Comparison of particle swarm optimization and genetic algorithm in the design of permanent magnet motors," in *IEEE 6th International Power Electronics and Motion Control Conference (IPEMC)*, 2009, pp. 822–825.

[36] H. Hasanien, A. Abd-Rabou, and S. Sakr, "Design optimization of transverse flux linear motor for weight reduction and performance improvement using response surface methodology and genetic algorithms," *Energy Conversion, IEEE Transactions on*, vol. 25, no. 3, pp. 598–605, Sept 2010.

[37] G. Pellegrino and F. Cupertino, "Fea-based multi-objective optimization of ipm motor design including rotor losses," in *IEEE Energy Conversion Congress and Exposition (ECCE)*, Sept. 2010, pp. 3659–3666.

[38] W. Jiang, T. M. Jahns, T. A. Lipo, W. Taylor, and Y. Suziki, "Machine design optimization based on finite element analysis in a high-throughput computing environment," in *IEEE Energy Conversion Congress and Exposition(ECCE)*, Sept. 2012, pp. 869–876.

[39] D. Zarko, D. Ban, and D. Goricki, "Improvement of a servo motor design including optimization and cost analysis," in *12th International Power Electronics and Motion Control Conference (EPE-PEMC)*, 2006, pp. 302–307.

[40] W. Ouyang, D. Zarko, and T. A. Lipo, "Permanent magnet machine design practice and optimization," in *41st IEEE Industry Applications Society (IAS) Annual Meeting Conference,*, vol. 4, Oct. 2006, pp. 1905 –1911.

[41] M. Barcaro, N. Bianchi, and F. Magnussen, "Permanent-magnet optimization in permanent-magnet-assisted synchronous reluctance motor for a wide constant-power speed range," *IEEE Transaction on Industrial Electronics*, vol. 59, no. 6, pp. 2495–2502, June 2012.

[42] F. Parasiliti, M. Villani, S. Lucidi, and F. Rinaldi, "Finite-element-based multiobjective design optimization procedure of interior permanent magnet synchronous motors for wide constant-power region operation," *IEEE Transactions on Industrial Electronics*, vol. 59, no. 6, pp. 2503 –2514, June 2012.

[43] A. Arkadan, M. ElBsat, and M. Mneimneh, "Particle swarm design optimization of ala rotor synrm for traction applications," *IEEE Transaction on Magnetics*, vol. 45, no. 3, pp. 956–959, March 2009.

[44] L. Jolly, M. Jabbar, and L. Qinghua, "Optimization of the constant power speed range of a saturated permanent-magnet synchronous motor," *IEEE Transactions on Industry Applications*, vol. 42, no. 4, pp. 1024–1030, 2006.

[45] H. Hasanien, A. Abd-Rabou, and S. Sakr, "Design optimization of transverse flux linear motor for weight reduction and performance improvement using response surface methodology and genetic algorithms," *IEEE Transactions on Energy Conversion*, vol. 25, no. 3, pp. 598–605, 2010.

[46] D. M. Ionel and M. M. Popescu, "Ultrafast Finite-Element Analysis of Brushless PM Machines Based on SpaceTime Transformations," *IEEE Transactions on Industry Applications*, vol. 47, no. 2, pp. 744 –753, March-April 2011.

[47] D. M. Ionel and M. Popescu, "Finite-element surrogate model for electric machines with revolving field – application to ipm motors," *Industry Applications, IEEE Transactions on*, vol. 46, no. 6, pp. 2424–2433, 2010.

[48] G. Sizov, D. M. Ionel, and N. A. O. Demerdash, "Modeling and parametric design of permanent-magnet ac machines using computationally efficient finite-element analysis," *Industrial Electronics, IEEE Transactions on*, vol. 59, no. 6, pp. 2403–2413, 2012.

[49] F. Cupertino, G. Pellegrino, and C. Gerada, "Design of synchronous reluctance machines with multi-objective optimization algorithms," in *Energy Conversion Congress and Exposition (ECCE), 2013 IEEE*, Sept 2013, pp. 1858–1865.

[50] K. J. Bathe, *Numerical methods in finite element analysis*. Prentice-Hall, 1976.

[51] J. Chaskalovic, *Finite Elements Methods for Engineering Sciences*. Springer Verlag, 2008.

[52] Peng Zhang, "A novel design optimization of a fault-tolerant ac permanent magnet machine-drive system," Ph.D. dissertation, Marquette University, December 2013.

[53] R. Wang and N. A. Demerdash, "Extra high speed modified lundell alternator parameters and open/short-circuit characteristics from global 3-d-fe magnetic field solutions," *IEEE Transactions on Energy Conversion*, vol. 7, no. 2, pp. 330 –341, Jun 1992.

[54] G. Bertotti, "General properties of power losses in soft ferromagnetic materials," *IEEE Transactions on Magnetics*, vol. 24, no. 1, pp. 621 –630, Jan 1988.

[55] J. Mugglestone, S. Pickering, and D. Lampard, "Effect of geometric changes on the flow and heat transfer in the end region of a tefc induction motor," in *Electrical Machines and Drives, 1999. Ninth International Conference on (Conf. Publ. No. 468)*, 1999, pp. 40 –44.

[56] Z. Kolondzovski, "Thermal and mechanical analyses of high-speed permanent-magnet electrical machines," Ph.D. dissertation, Aalto University, 2010.

[57] S. Nategh, O. Wallmark, M. Leksell, and S. Zhao, "Thermal analysis of a pmasrm using partial fea and lumped parameter modeling," *Energy Conversion, IEEE Transactions on*, vol. 27, no. 2, pp. 477–488, June 2012.

[58] MotorCAD. [Online]. Available: http://www.motor-design.com/motorcad.php

[59] A. Boglietti, A. Cavagnino, D. Staton, M. Shanel, M. Mueller, and C. Mejuto, "Evolution and modern approaches for thermal analysis of electrical machines," *Industrial Electronics, IEEE Transactions on*, vol. 56, no. 3, pp. 871–882, 2009.

[60] D. Staton and A. Cavagnino, "Convection heat transfer and flow calculations suitable for analytical modelling of electric machines," in *IEEE Industrial Electronics, IECON 2006 - 32nd Annual Conference on*, Nov 2006, pp. 4841–4846.

[61] D. Dorrell, "Combined thermal and electromagnetic analysis of permanent-magnet and induction machines to aid calculation," *Industrial Electronics, IEEE Transactions on*, vol. 55, no. 10, pp. 3566–3574, Oct 2008.

[62] J.P.Holman, *Heat Transfer*. New York: McGraw-Hill, 1997.

[63] F. P. Incropera and D. P. D. Witt, *Introduction to Heat Transfer*. Hoboken, NJ: Wiley, 1990.

[64] W. S. Janna, *Engineering Heat Transfer*. New York: Van Nostrand-Reinhold, 1988.

[65] F. Marignetti, V. Delli Colli, and Y. Coia, "Design of axial flux pm synchronous machines through 3-d coupled electromagnetic thermal and fluid-dynamical finite-element analysis," *Industrial Electronics, IEEE Transactions on*, vol. 55, no. 10, pp. 3591–3601, Oct 2008.

[66] Wenying Jiang and T. Jahns, "Coupled electromagnetic-thermal analysis of electric machines including transient operation based on finite element techniques," in *Energy Conversion Congress and Exposition (ECCE), 2013 IEEE*, 2013, pp. 4356–4363.

[67] ANSYS Maxwell. [Online]. Available: http://www.ansys.com/

[68] R. Storn and K. Price, "Differential evolution - a simple and efficient heuristic for global optimization over continuous spaces," *Journal of Global Optimization*, vol. 11, pp. 341 – 359, 1997.

[69] K. V. Price, R. M. Storn, and J. A. Lampinen, *Differential Evolution-A Practical Approach to Global Optimization*. Springer-Verlag Berlin Heidelberg, 2005.

[70] Y. Wang and Z. Cai, "Combining multiobjective optimization with differential evolution to solve constrained optimization problems," *Evolutionary Computation, IEEE Transactions on*, vol. 16, no. 1, pp. 117–134, Feb 2012.

[71] Yi Wang, D. M. Ionel and D. Staton, "Ultrafast steady-state multi-physics model for PM and synchronous reluctance machines," in *Energy Conversion Congress and Exposition (ECCE), 2014 IEEE*, Sep 2014.

[72] M. Popescu, J. E. Goss, D. Staton, Yi Wang, and D. M. Ionel, "On the feasibility of integer and fractional number of slots per pole distributed winding designs for synchronous reluctance motors," in *Energy Conversion Congress and Exposition (ECCE), 2014 IEEE*, Sep 2014.